



# The Central Crete ( $M_w$ 6.0) Strong Earthquake on 27 September 2021 ... A year after

Edited by

**Filippos Vallianatos & Maria Kouli**



## Contributors

**Filippos Vallianatos** – Department of Geophysics–Geothermics, Faculty of Geology and Geoenvironment, National and Kapodistrian University of Athens, 15772 Athens, Greece, [fvallian@geol.uoa.gr](mailto:fvallian@geol.uoa.gr)

Institute of Physics of the Earth’s Interior and Geohazards, UNESCO Chair on Solid Earth Physics and Geohazards Risk Reduction, Hellenic Mediterranean University, Research & Innovation Center, 3 Romanou str., 73133, Chania, Crete, Greece.

**John P. Makris** – Institute of Physics of the Earth’s Interior and Geohazards, UNESCO Chair on Solid Earth Physics and Geohazards Risk Reduction, Hellenic Mediterranean University, Research & Innovation Center, 3 Romanou str., 73133, Chania, Crete, Greece, [jpmakris@hmu.gr](mailto:jpmakris@hmu.gr)

**Vasilios Saltas** – Institute of Physics of the Earth’s Interior and Geohazards, UNESCO Chair on Solid Earth Physics and Geohazards Risk Reduction, Hellenic Mediterranean University, Research & Innovation Center, 3 Romanou str., 73133, Chania, Crete, Greece, [vsaltas@hmu.gr](mailto:vsaltas@hmu.gr)

**Maria Kouli** – Institute of Physics of the Earth’s Interior and Geohazards, UNESCO Chair on Solid Earth Physics and Geohazards Risk Reduction, Hellenic Mediterranean University, Research & Innovation Center, 3 Romanou str., 73133, Chania, Crete, Greece, [mkouli@hmu.gr](mailto:mkouli@hmu.gr)

Hellenic Mediterranean University, Faculty of Electronic Engineering, Romanou 3, Chania, Crete, Greece

**Sofia Peleli** – Institute of Physics of the Earth’s Interior and Geohazards, UNESCO Chair on Solid Earth Physics and Geohazards Risk Reduction, Hellenic Mediterranean University, Research & Innovation Center, 3 Romanou str., 73133, Chania, Crete, Greece, [ddk81@edu.hmu.gr](mailto:ddk81@edu.hmu.gr)

Hellenic Mediterranean University, Department of Electronic Engineering, Romanou 3, Chania, Crete, Greece

**Georgios Chatzopoulos** – Institute of Physics of the Earth’s Interior & Geohazards, Hellenic Mediterranean University Research & Innovation Center, Chania, Crete, Greece, [gh1983@hotmail.com](mailto:gh1983@hotmail.com)

**Georgios Michas** – Section of Geophysics–Geothermics, Department of Geology and Geoenvironment, National and Kapodistrian University of Athens, 15784 Zografou, Athens, Greece, [gemichas@geol.uoa.gr](mailto:gemichas@geol.uoa.gr)

Institute of Physics of the Earth’s Interior and Geohazards, Hellenic Mediterranean University Research & Innovation Center, 3 Romanou str., 73133, Chania, Crete, Greece.

**Andreas Karakonstantis** – Section of Geophysics–Geothermics, Department of Geology and Geoenvironment, National and Kapodistrian University of Athens, 15784 Zografou, Athens, Greece, [akarakon@geol.uoa.gr](mailto:akarakon@geol.uoa.gr)

Institute of Physics of the Earth’s Interior & Geohazards, Hellenic Mediterranean University Research & Innovation Center, Chania, Crete, Greece

**Kyriaki Pavlou** – Section of Geophysics–Geothermics, Department of Geology and Geoenvironment, National and Kapodistrian University of Athens, 15784 Zografou, Athens, Greece, [kpavlou@geol.uoa.gr](mailto:kpavlou@geol.uoa.gr)

Institute of Physics of the Earth's Interior & Geohazards, Hellenic Mediterranean University Research & Innovation Center, Chania, Crete, Greece

**Sophia-Ekaterini Avgerinou** – Section of Geophysics–Geothermics, Department of Geology and Geoenvironment, National and Kapodistrian University of Athens, 15784 Zografou, Athens, Greece, [sophiavg@geol.uoa.gr](mailto:sophiavg@geol.uoa.gr)

Institute of Physics of the Earth's Interior and Geohazards, Hellenic Mediterranean University Research & Innovation Center, 3 Romanou str., 73133, Chania, Crete, Greece.

**Eleni-Apostolia Anyfadi** – Section of Geophysics–Geothermics, Department of Geology and Geoenvironment, National and Kapodistrian University of Athens, 15784 Zografou, Athens, Greece, [eleniapanif@geol.uoa.gr](mailto:eleniapanif@geol.uoa.gr)

Institute of Physics of the Earth's Interior and Geohazards, Hellenic Mediterranean University Research & Innovation Center, 3 Romanou str., 73133, Chania, Crete, Greece.

**George Hloupis** – Department of Surveying and Geoinformatics Engineering, University of West Attica, Egaleo Campus, 12244 Athens, Greece. E-mail: [hloupis@uniwa.gr](mailto:hloupis@uniwa.gr)

Institute of Physics of the Earth's Interior and Geohazards, Hellenic Mediterranean University Research & Innovation Center, 3 Romanou str., 73133, Chania, Crete, Greece

**Sakkas Vassilis** – Section of Geophysics–Geothermy, Department of Geology and Geoenvironment, National and Kapodistrian University of Athens, GR 15784 Zografou, Athens, Greece.

Institute of Physics of the Earth's Interior and Geohazards, Hellenic Mediterranean University Research & Innovation Center, 3 Romanou str., 73133, Chania, Crete, Greece.

**Nicola Angelo Famiglietti** – Istituto Nazionale di Geofisica e Vulcanologia, Rome, Italy; [nicola.famiglietti@ingv.it](mailto:nicola.famiglietti@ingv.it)

**Zeinab Golshadi** – Institute of Geophysics, University of Tehran, Tehran, Iran.; [z.golshadi@alumni.ut.ac.ir](mailto:z.golshadi@alumni.ut.ac.ir)

**Riccardo Caputo** – Dipartimento di Fisica e Scienze della Terra, Università degli Studi di Ferrara, 44121 Ferrara, Italy; [rcaputo@unife.it](mailto:rcaputo@unife.it)

Institute of Physics of the Earth's Interior and Geohazards, Hellenic Mediterranean University Research & Innovation Center, 3 Romanou str., 73133, Chania, Crete, Greece.

**Simone Atzori** – Istituto Nazionale di Geofisica e Vulcanologia, Rome, Italy; [simone.atzori@ingv.it](mailto:simone.atzori@ingv.it)

**Raffaele Moschillo** – Istituto Nazionale di Geofisica e Vulcanologia, Rome, Italy; [raffaele.moschillo@ingv.it](mailto:raffaele.moschillo@ingv.it)

**Gianpaolo Cecere** – Istituto Nazionale di Geofisica e Vulcanologia, Rome, Italy; [gianpaolo.cecere@ingv.it](mailto:gianpaolo.cecere@ingv.it)

**Ciriaco D'Ambrosio** – Istituto Nazionale di Geofisica e Vulcanologia, Rome, Italy; [ciriaco.dambrosio@ingv.it](mailto:ciriaco.dambrosio@ingv.it)

**Annamaria Vicari** – Istituto Nazionale di Geofisica e Vulcanologia, Rome, Italy; [annamaria.vicari@ingv.it](mailto:annamaria.vicari@ingv.it)

Foreword to **The Central Crete ( $M_w6.0$ ) Strong Earthquake on 27 September 2021 ... A year after**

Crete is situated at the front-arc of the Hellenic Subduction Zone and therefore, it is characterized by high seismicity with earthquake magnitudes that reach up to  $\sim 8.0$ . From an examination of the seismic history of the area, it comes out that no shallow strong earthquakes with epicenters lying on the island occurred during the instrumental period of seismology, i.e., since 1900.

On 27 September 2021 a strong earthquake with Moment magnitude,  $M_w$  6.0, associated with normal faulting ruptured the central part of the island of Crete, Greece, at about 20 km to the south of Heraklion, the capital city of the island. The earthquake caused one fatality, about 20 injuries and extensive building damage in the area of Arkalochori town and in other villages of the area.

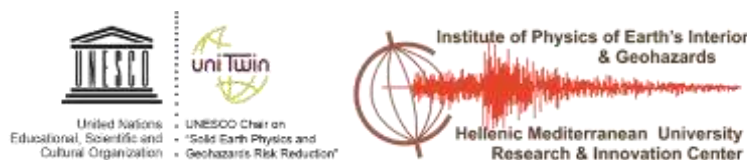
The mainshock of 27 September 2021 is the only known strong earthquake that ruptured the Arkalochori area ever. The main shock was preceded by a persisting foreshock activity since the beginning of June 2021, with the strongest foreshock of  $M_w4.6$  occurring on 24 July 2021. Intense aftershock activity followed the main shock with the largest aftershock ( $M_w5.1$ ) taking place on 28 September 2021.

In this Special Edition, a year after the Arkalochori earthquake, a summary of the the scientific work of the Institute of Physics of the Earth's Interior & Geohazards, along with the UNESCO Chair on Solid Earth Physics and Geohazards Risk Reduction, of the Hellenic Mediterranean University Research and Innovation Center and its Collaborations is presented towards understanding the seismogenic process, the causative fault associated with the Arkalochori mainshock and the seismic potential of the area from the short- and long-term perspective.

A lot of work done and much more is on the way to support the understanding of a unique event in the seismic history of Crete.

The Editors

*Filippos Vallianatos & Maria Kouli*





## Chapter 1

On the patterns and scaling properties  
of the 2021-2022 Arkalochori earthquake sequence  
(Central Crete, Greece)  
based on Seismological,  
Geophysical & Satellite Observations

**Abstract:** The September 27, 2021, damaging mainshock (Mw6.0) close to Arkalochori village, is the strongest earthquake that was recorded during the instrumental period of seismicity in Central Crete (Greece). The mainshock was preceded by a significant number of foreshocks that lasted nearly four months. Maximum ground subsidence of about 18 cm was estimated from InSAR processing. The aftershock sequence is located in an almost NE-SW direction and divided into two main clusters, the southern and the northern ones. The foreshock activity, the deformation area, and the strongest aftershocks are located within the southern cluster. Based on body-wave travel-times, a 3-D velocity model was developed, while using combined space and ground-based geodetic techniques, the co-seismic ground deformation is presented. Moreover, we examined the co-seismic static stress changes with respect to the aftershocks' spatial distribution during the major events of the foreshocks, the Mw=6.0 main event as well as the largest aftershock. Both the foreshock and the aftershock sequences obey scaling law for the frequency-magnitude distribution as derived from the framework of Non-Extensive Statistical Physics (NESP). The aftershock production rate decays according to the modified Omori scaling law, exhibiting various Omori regimes due to the generation of secondary aftershock sequences. The analysis of the inter-event time distribution, based on NESP, further indicates asymptotic power-law scaling and long-range correlations among the events. The spatiotemporal evolution of the aftershock sequence indicates triggering by coseismic stress transfer, while its slower migration towards the outer edges of the area of the aftershocks, related to the logarithm of time, further indicates a possible afterslip.

---

## 1. Introduction

Greece is located at the southeastern tip of Europe where a variety of geological processes take place, such as the formation of the Alpine mountain chain from the Western French Alps to the Dinarides in the Balkan Peninsula due to the collision between European and Nubian plates. Furthermore, observed intense deformation in the Aegean and the surrounding regions produces a significant portion of SE Europe's seismicity, concentrated in thrust structures along the Hellenic Arc and smaller extensive ruptures in the area of the Aegean back-arc [1-4].

The plioseismal area is located in the front of the Hellenic arc, near the region where the European and Nubia plates converge, giving rise to large earthquakes [1-5]. The most characteristic tectonic features in the vicinity of the rapture zone are the two large tectonic basins located in the northern Heraklion and the southwest Messara. These were formed by extensional forces from an arc-normal pull since 11Ma which formed the average NNE-SSW direction faults [1,2]. The basins are filled with Miocene to Pliocene sediments overlaid by Quaternary deposits and in the north-eastern part there are exposed nappes tectonic features consisting of Carbonates of the Tripolis and Trypation units.

Several field surveys showed the existence of active extensional faults in the upper crust of Crete along both E-W and N-S directions [e.g. 6-12]. The 2021 seismic crisis in Arkalochori and the neighboring villages was located in a fault system of what was considered as possibly active with NW-SE and NE-SW direction of strike [e.g. 8,10, 11, 13-15], bounding the Heraklion basin.

Destructive earthquakes occurred in the broader Crete region during the pre-instrumental era [16-18]. In Central Crete, two major historical earthquakes have been reported, both in the vicinity of Heraklion. The first one was on July 1, 1494 (M= 5.4) [16] while on November 26, 1595, a second event (M~6.4) took place, both causing severe damage on the island of Crete [16,18].

On September 27, 2021 a  $M_w=6.0$  event, linked to an approximately N-S trending normal fault at the central part of the island of Crete, Greece, occurred ~20 km to the south of the prefecture's capital. The occurrence of the mainshock took place after a long time of foreshocks since the first half of June 2021 with criticality characteristics [19] and a long aftershock sequence with the strongest event occurring on September 28 with local magnitude  $M_L5.3$ . Following the recent report by ITSAK [20], the recorded PGA at the epicentral area (Arkalochori) was 0.62 g in the horizontal component (N-S) and 0.82 g in the vertical one, with a duration of strong ground motion ( $>0.1$  g) almost 6 s. Its focal mechanism is characterized by an SSW-NNE to SW-NE-trending, nearly dip-slip normal faulting. Its strike generally ranges  $N200^\circ E-N230^\circ E$  and its dip angle varies between  $40^\circ$  and  $60^\circ$ . The active fault associated with the main event is the Kastelli Fault, which has a progressive change in the strike from  $225^\circ$  to  $265^\circ$  northeastwards and dip between  $60^\circ-80^\circ$  northwestwards [9, 21-23]

In this work, we present the consistency between seismological, geodetic, satellite and geophysical for the 2021-2022 Arkalochori earthquake sequence, highlighting the complementarity of multi-disciplinary approaches. First, we relocate the 2021-2022 Central Crete earthquake sequence to have a more accurate insight on its distribution and scaling properties. Based on body-wave travel-times, we have developed a 3-D velocity model, while using combined space and ground based geodetic techniques the co-seismic ground deformation is obtained. Moreover, we examined the co-seismic static stress changes with respect to the aftershocks' spatial distribution during the major events of the foreshocks, the  $M_w=6.0$  main event as well as the largest aftershock. In addition, the scaling properties of the 2021-2022 Central Crete earthquake sequence are investigated thoroughly, and we analyzed the aftershocks decay rate based on modified-Omori formula. Furthermore, the frequency-magnitude distribution parameters of the earthquake sequence along with that of the distribution of inter-event times between the successive events are viewed in terms of non-extensive statistical physics in order to provide more detailed insights into the complexity nature of long term correlation of the earthquake generation process.

## 2. Seismological Data and Earthquake sequence analysis

The 2021 seismic crisis in the wider area of Arkalochori began in the form of an earthquake swarm in early June 2021. The situation, however, changed dramatically since the occurrence of the  $M_w=6.0$  main event on September 27, 2021. Although several permanent stations of the Hellenic Unified Seismological Network operate on the island of Crete at the time of the mainshock, the closest station to the epicentral area was KNSS of the Hellenic Mediterranean University Research Center (HC network at formerly Technological Educational Institute of Crete [24], at a distance of about 12–22 km. These data were manually revised using a regional 1-D model and were put into a relocation procedure in order to obtain more accurate results, as will be discussed in the next sections.

### 2.1 Data analysis

The Arkalochori earthquake sequence is divided into two main temporal groups, one that preceded the September 27th  $M_w=6.0$  mainshock, consisting of 620 events with a significant rise in numbers during July and August 2021, and the aftershock sequence, divided into three sub-groups, composed by 4130 seismic events (Figure 1). A major part of the sequence was recorded by local stations of the regional Hellenic Unified Seismological Network (HUSN), with the nearest stations being KNSS, PFKS (IFEGG), located ~20 km to the SW and NE of the epicenter, respectively. On October 1, 2021, the Geodynamics Institute of the National Observatory of Athens (GI-NOA) installed 4 temporary stations (CRE1-4) around the aftershock zone, contributing to the depth accuracy and providing a preliminary hypocentral solution for this time period.

A total of 4,750 events of the 2021-2022 Arkalochori sequence that occurred during the period between 13 January and 31 January 2022 (Figure 2) were detected and manually analyzed using real-time waveform data from the Hellenic Unified Seismological Network (HUSN) in the SeisComP3 graphical user interface [25]. During the first stage of the sequence analysis, hypocentres were located in Near Real-Time, by employing the Hypo71 single-event algorithm [26] and a custom regional 1-D velocity model for the Hellenic peninsula [27].

In this study, two local 1-D velocity models [28, 29] have been used through the second stage of the data processing, running the HypoInverse code [30]. Residual values from these models were compared (Table 1) with no significant differences, while the epicentral differences were less than 0.5 km, whereas the depths, which are more sensitive to

the velocity model, differed by about 1 km on average. The [28] velocity model (Model 1) provided much shallower events than the respective ones of [29] (Model 2) and especially for the stronger events of the sequence ( $M_w=6.0$  and  $M_w=5.3$ ) that were located at a depth shallower than 5 km (2.7 and 0.7 km respectively), which seemed unrealistic in terms of earthquake physics and the past of the area.

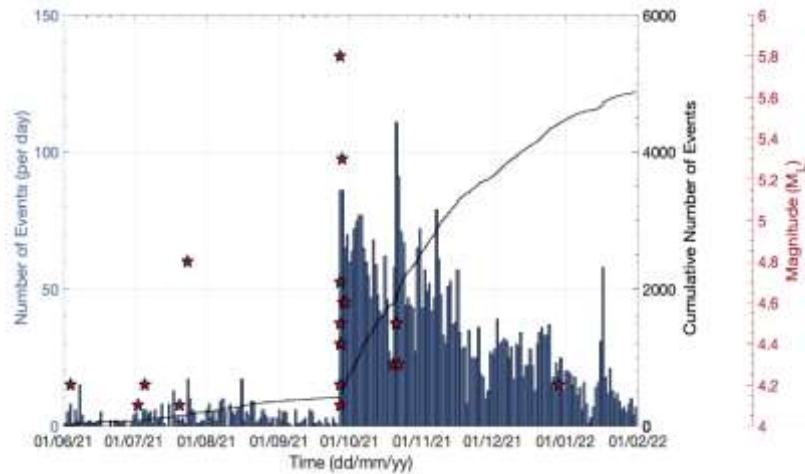


**Figure 1.** Seismicity rate in terms of events per day (blue vertical bars) and cumulative number of events (solid black line) during June 2021–January 2022 in the area of Arkalochori. The occurrence of events with  $M_L \geq 4$  is marked by red stars ( $M_L$  magnitude in the red axis to the right).

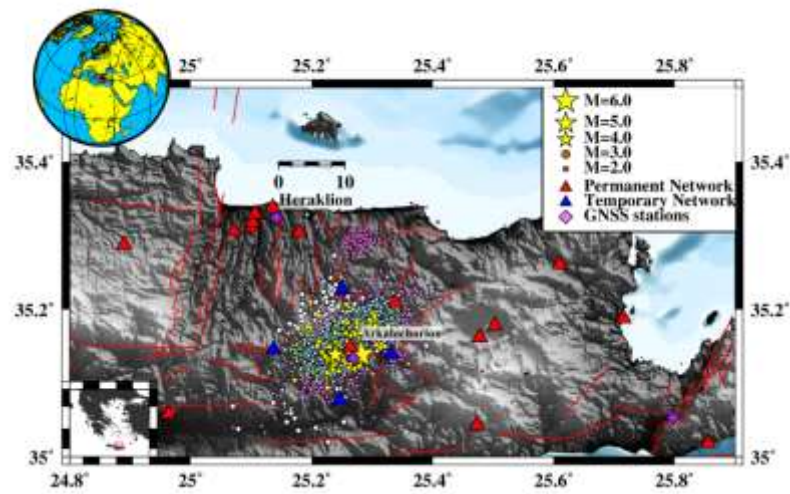


**Figure 2.** Spatial distribution of the 2021-2022 Arkalochori sequence, for 4750 events that occurred during the period between 13/1/2021 to 31/1/2022. The locations of the permanent (red triangles) and the temporary (blue triangles) stations are presented. The  $M \geq 4.0$  earthquakes are depicted by yellow stars. Faults are marked as red lines (see text for details). On the top left corner the location of Greece is indicated in the red triangle while on the bottom left one the study area is included in the red rectangle.

The final hypocentral locations were obtained using the velocity model of [29]. The range of depth distribution is mainly between 5 and 15 km for the aftershocks of the September 27<sup>th</sup>  $M_w=6.0$  event. Figure 2 presents the distribution of 4750 events that were manually revised and relocated with HypoInverse code, along with the faults in the area as extracted from [31].

**Table 1.** Comparison of the error statistics between Model 1 [28] and Model 2 [29] for the Arkalochori seismic sequence.

<b>Model:</b>	<b>Model 1</b>	<b>Model 2</b>
Mean RMS (sec)	0.26	0.26
Mean ERH (km)	1.30	1.31
Mean ERZ (km)	4.41	4.52
Mean Depth (km)	9.43	13.94

The seismic sequence was divided into 5 sub-groups according to its spatiotemporal occurrence (Figure 3):

1. January 13 – 27 September 27, 2021 (period A), consisting of 620 events,
2. September 27–28 September 28, 2021 (period B), the first day of the aftershock sequence and just a few hours before the greatest aftershock (M5.3), composed of 90 events,
3. September 28–October 12, 2021 (period C), just after the occurrence of the M=5.3 aftershock at 04:48 UTC, consisting of 803 events,
4. October 12 – October 31, 2021 (period D), where the M=4.0 event took place after a significant decay in the aftershocks number in Arkalochori.
5. November 1 – January 31, 2022 (period E), which comprises small to moderate magnitude events in a deeper part of the crust ( $H>20$  km) located near Herakleion.

## **2.2 Hypocentral relocation of the earthquake sequence**

Accurate earthquake hypocenter parameters are required in order to obtain a detailed image of the structural properties and processes that trigger seismic activity. The precision of hypocenter locations and their uncertainties depend on several factors, including the number and quality of available seismic phases, the accuracy with which arrival times are measured, the network geometry, the knowledge of the velocity structure, and the linear approximation to a set of non-linear equations, which is assumed in the inversion. hypoDD [32] is an algorithm that reduces residuals between observed and theoretical differences of travel times (or double-differences) for pairs of neighboring events at each station that recorded both events, as can be seen from eq. 1. This way, errors due to unmodeled velocity structures are minimized without station corrections. A minimum 1-D layered velocity model is used to predict the travel time differences and partial derivatives (eq. 2).

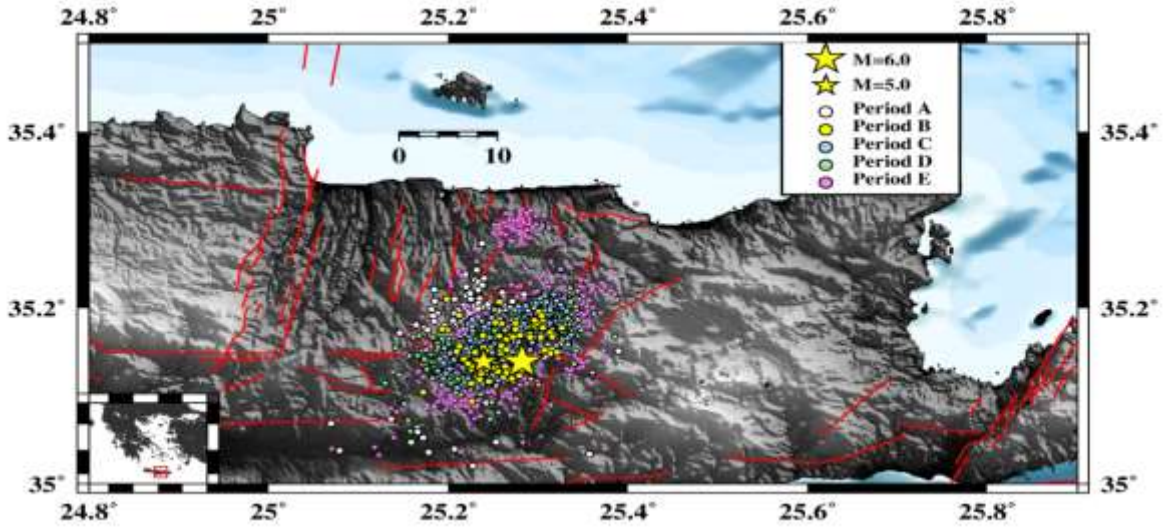


**Figure 3.** Temporal distribution of the 2021-2022 Arkalochori sequence for 4750 events. Period A, B, C, D and E are marked with orange, yellow, green, purple and violet circles respectively. The  $M \geq 4.0$  earthquakes are depicted by yellow stars. Faults are marked as red lines (see text for details).

$$dr_k^{ij} = (t_k^i - t_k^j)^{obs} - (t_k^i - t_k^j)^{cal} \quad (1)$$

$$\frac{\partial t_k^i}{\partial m} \Delta m^i - \frac{\partial t_k^j}{\partial m} \Delta m^j = dr_k^{ij} \quad \text{where } m=(x, y, z) \quad (2)$$

Inter-event distance and misfit weighting are applied to catalogue data after the end of each iteration, in order to optimize their quality during the relocation procedure. Horizontal and vertical relative spatial errors can be minimized by approximately one order of magnitude under certain conditions. In this study, more than 4500 events of  $ML \geq 0.6$ , comprising 58777 phases, were relocated with hypoDD. Among the main factors that had been taken into consideration during the relocation procedure were the following: a) network coverage of the area, b) the size of the dominant clusters, and c) their maximum separation distance. This led to the formation of 98070 P- and 43812 S-phase pairs respectively for the whole volume, while in the central cluster (cluster #1), where the mainshock ( $M=6.0$ ) largest aftershock ( $M_w=5.3$ ) is situated, 98070 P- and 18673 S-phase pairs were formed.

In the area of Central Crete, 4728 out of 4750 events of the initial catalogue ( $M \geq 0.6$ ), were relocated with hypoDD, giving a first result that could be rated as satisfactory. The mean temporal errors (rms) were reduced from 0.14 sec to 0.11 sec, while the spatial errors ( $er_x$ ,  $er_y$ ,  $er_z$ ) were decreased from 1.0, 0.8, and 2.0 km to 0.3, 0.3, and 0.4 km, respectively (Table 1). The hypoDD-estimated errors in the final locations were calculated using the LSQR method, which may not be representative of the real ones [32].

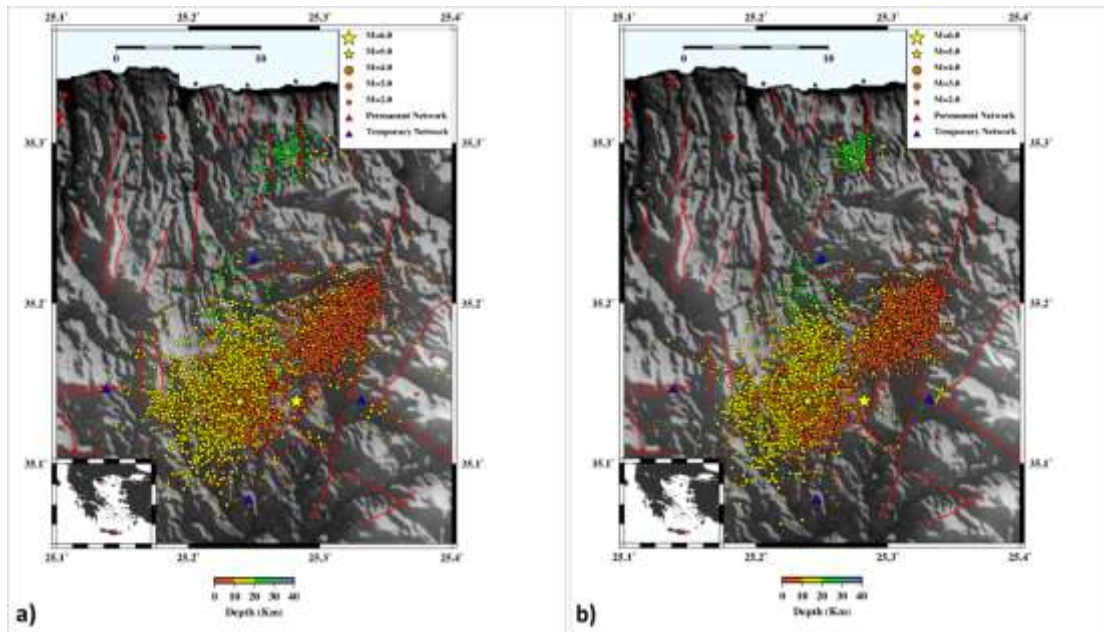


**Figure 4.** a) Location of the 2021-2022 Arkalochori sequence for 4750 events b) Relocated events of the aftershock sequence using hypoDD. The locations of the permanent (red triangles) and the temporary (blue triangles) are presented (see text for details). The  $M \geq 4.0$  earthquakes are depicted by yellow stars. Faults are marked as red lines (see text and [30] for details).

The epicenter of the mainshock was located less than 3 km to the SE of Arkalochori (lat:  $35.1416^\circ$  N, long:  $25.2736^\circ$  E) at a depth of  $\sim 9.6$  km, obtained by the double-difference algorithm procedure. The optimization of the final results leads to the clustering of the earthquake sequence into four main clusters. A dense cluster of events has occurred west of the mainshock, in an approximately 15-km-long area associated with the foreshocks (cluster 1). The epicenters of cluster 2 were mainly distributed in the area between Amourgeles and Parthenio N-S oriented normal faults, in the region to the west of Arkalochori. Further to the NE, another significant cluster of events (cluster 3) was also observed, in the footwall of Agnos NE-SW striking normal fault, near Kastelli (Figure 4). Most seismicity is in a range of focal depths between 7 and 18 km.

Furthermore, five (5) cross-sections were performed in order to see the impact of the relocation procedure on the sequence hypocentral depths and the discrimination of the local activated structures. Cross-sections 1-2 have a NNE-SSW orientation, and 3-5 WNW-ESE direction, perpendicular to the NE trending faults. The geometry of the hypocenters as they appear in the performed cross-sections, reveal the activation of a fault, dipping  $\sim 60^\circ$  to the WNW, and a smaller antithetic structure, possibly connected to Galatas N-S striking normal fault (Figure 5).

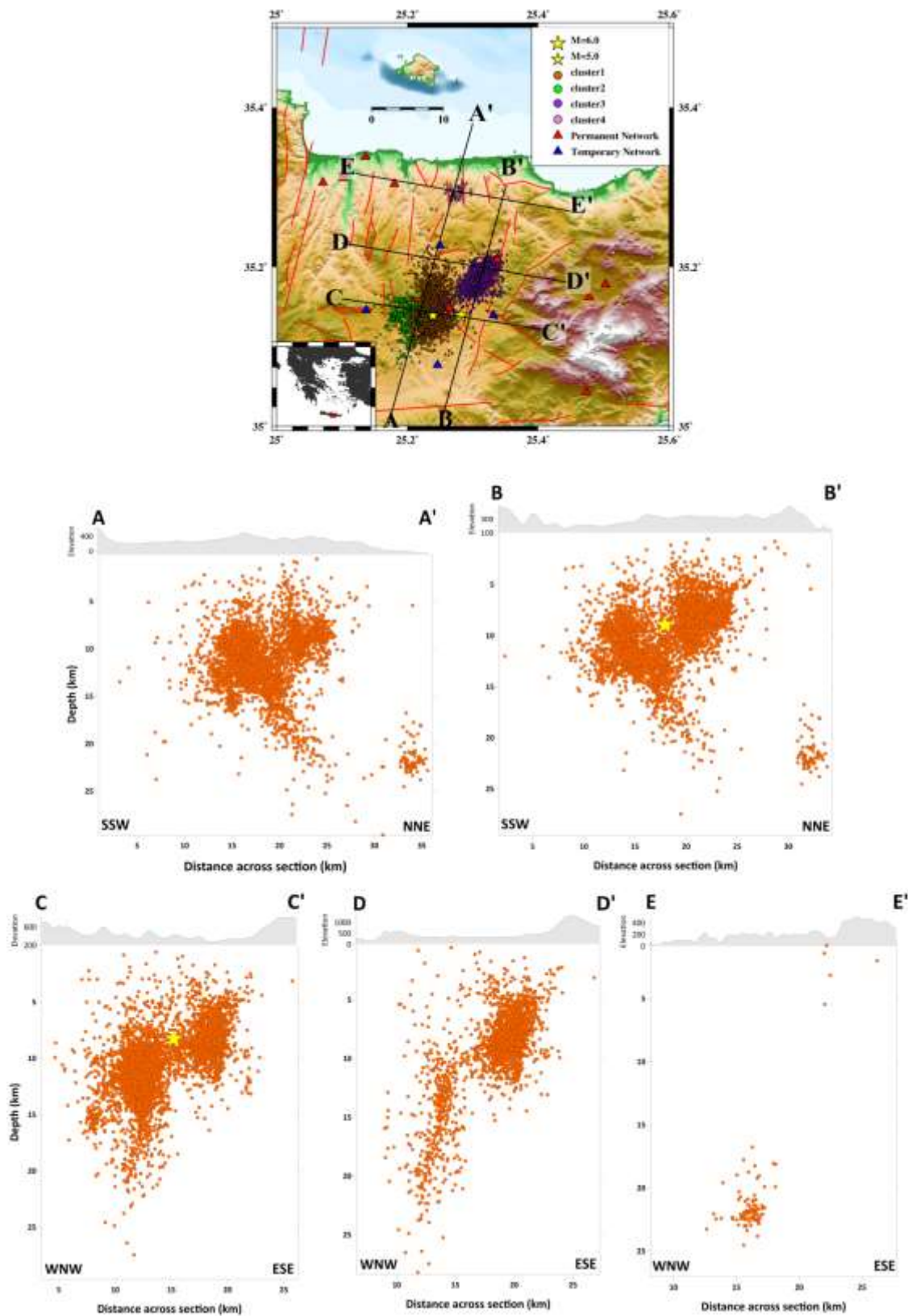


**Figure 5.** Presentation of the map of the 5 cross-sections, 5 km wide (A-A', B-B', C-C', D-D' and E-E') on the left side of the figure and the results of the SSW-NNE oriented cross-sections (upper panel) and the results of WNW-ESE oriented cross-sections (lower panel) on the right side. The projection of the September 27<sup>th</sup> mainshock is depicted by yellow star on sections B-B' and C-C'.

An almost sub-vertical structure makes an appearance in the cross-sections north of the epicenter of the mainshock (sections B-B', D-D'; Figure 5). The earthquake activity that belongs to cluster 4, started on January 16th, 2022, with an event of  $ML=3.3$  and continued throughout the first two months of 2022 as the latest contribution to the seismic sequence. The hypocenters appear to be located in deeper parts of the crust and they have an apparent dip towards the WNW.

### 3. Travel-time Tomography

Local Earthquake Tomography (LET) techniques have been successfully applied to reveal the velocity structure in such cases of aftershock sequences. In this paper, the body-wave inversion was based on the Local Tomographic Software (LOTOS) by [33]. P- and S-phases of more than 800 earthquakes, recorded during the 2021-2022 time period by local and regional stations of the Hellenic Unified Seismological Network (HUSN) and the Hellenic Strong Motion Network (HSMN), located in Southern Greece, were used for the tomographic inversion. Checkerboard tests were performed to set the input parameter values that produced better resolution and increased the fidelity area. Regarding the 3-D tomographic inversion, a dataset consisting of 12236 P- and 9820 S-arrival-times was chosen, with at least 12 phases per event (Supplementary material, Figure S2). LOTOS code provides two alternative options: inversion for  $V_P$  and  $V_S$  ( $V_P-V_S$  scheme) using P and S travel-time residuals ( $dt_P$  and  $dt_S$ ) and inversion for  $V_P$  and  $V_P/V_S$  ratio ( $V_P-V_P/V_S$  scheme) using  $dt_P$  and differential residuals,  $dt_S - dt_P$ . In this work, inversion was performed for  $V_P-V_S$  and  $V_P-V_P/V_S$  schemes, in order to obtain additional constraints concerning the  $V_P$  and  $V_S$  anomalies [33, 34].

The stations' coordinates, their elevation, and the body-wave arrival times are essential as input data to the algorithm. The hypocenter locations and the origin times are not necessarily needed, given that their determination is performed during the execution of the calculations. However, if preliminary hypocentral locations are available, they are used to decrease the processing time. Moreover, the available initial 1-D velocity model [29] and a set of input parameters, i.e. parameterization, grid dimensions, and damping parameter, are defined by the user [33]. A nodal representation was employed, given that the velocity field, reconstructed by a three-dimensional grid, does not assume a specific geometry of heterogeneities [35]. The grid spacing ( $\sim 2$  km) was kept considerably smaller than the expected resolution length, to reduce the bias of the resulting models due to the grid configuration. The optimal grid mesh has been determined considering the stations/events geometry. In addition, to further decrease the influence of the model parameterization on the solutions, the inversion was repeated using four grid orientations ( $0^\circ$ ,  $22^\circ$ ,  $45^\circ$ , and  $67^\circ$ ). The inversion results, obtained for the previously mentioned grids, were stacked into one summary model, reducing the artifacts related to grid orientation, as described by [33].

**Table 2.** Average absolute values of P- and S-wave residuals and their cumulative reduction percentage during the inversion of experimental data.

Iteration	P-residual (s)	P-residual reduction (%)	S-residual (s)	S-residual reduction (%)
1	0.269	0.00	0.437	0.00
2	0.211	21.50	0.248	43.14
3	0.194	27.63	0.222	49.12
4	0.188	30.08	0.218	50.10
5	0.186	30.85	0.211	51.69

The values of the P- and S-wave residuals during different iteration steps of the inversion procedure are presented in Table 2. For the P- and S-data, the reduction of the residual is  $\sim 10\%$  and  $13\%$ , respectively. The resulting P- and

S-wave velocity anomalies with respect to the starting 1-D velocity model are shown in horizontal depth slices (Figures 5-6). The interpretation of the obtained results is limited to the unmasked confidence regions, given that they are characterized by reasonable reconstruction of the checkerboard model. The mean computed P and S anomalies for the study area do not exceed  $\pm 13\%$ .

Strong NW-SE and E-W oriented negative velocity anomalies predominate at both the upper and the lower crust of Central Crete. These are observed down to 15 km depth in the tomograms of Figures 6-7. Deeper than 20 km the model lacks resolution and can only be considered indicative, hence it is not discussed. At the depth slice of 5 km, a NE-SW-trending zone of negative body-wave velocity perturbations appears near the epicentral region of the Mw=6.0 Arkalochori earthquake (Figures 6-7). This anomaly follows the mean distribution of Alluvial deposits and post-alpine sediments which are bounded by positive ( $\sim 13\%$ ) body-wave velocity perturbations, possibly connected to the older post-alpine sediments of Viannos formation and the Mesozoic carbonate rocks to the east and south of Arkalochori basin, respectively [13, 22]. In the area north of Arkalochori, an E-W-trending anticorrelated pattern of negative P- and positive S-wave velocity anomalies are observed at the depth range of 5-10 km ( $35.20^{\circ}\text{N}$ - $35.30^{\circ}\text{N}$ ,  $25.25^{\circ}\text{E}$ - $25.40^{\circ}\text{E}$ ). This anomaly coincides with the eastward bending of Kastelli normal fault direction, from the area east of Arkalochori towards the town of Malia ( $35.20^{\circ}\text{N}$ - $35.27^{\circ}\text{N}$ ,  $25.34^{\circ}\text{E}$ - $25.45^{\circ}\text{E}$ ). In the depth slice of 15 and 20 km, and almost NNE-SSW discontinuity of positive to the west and negative to the east  $V_P$  anomalies (Figure 6) are identified along the west-dipping Agnos normal fault. Furthermore, cross-sections B-B' and C-C' in both Primary (P) and Secondary (S) wave velocity anomalies (Figures 8-9), reveal this west-dipping structure that may be related to Agnos high-angle ( $\sim 60^{\circ}$ ) normal fault [13, 21-23].

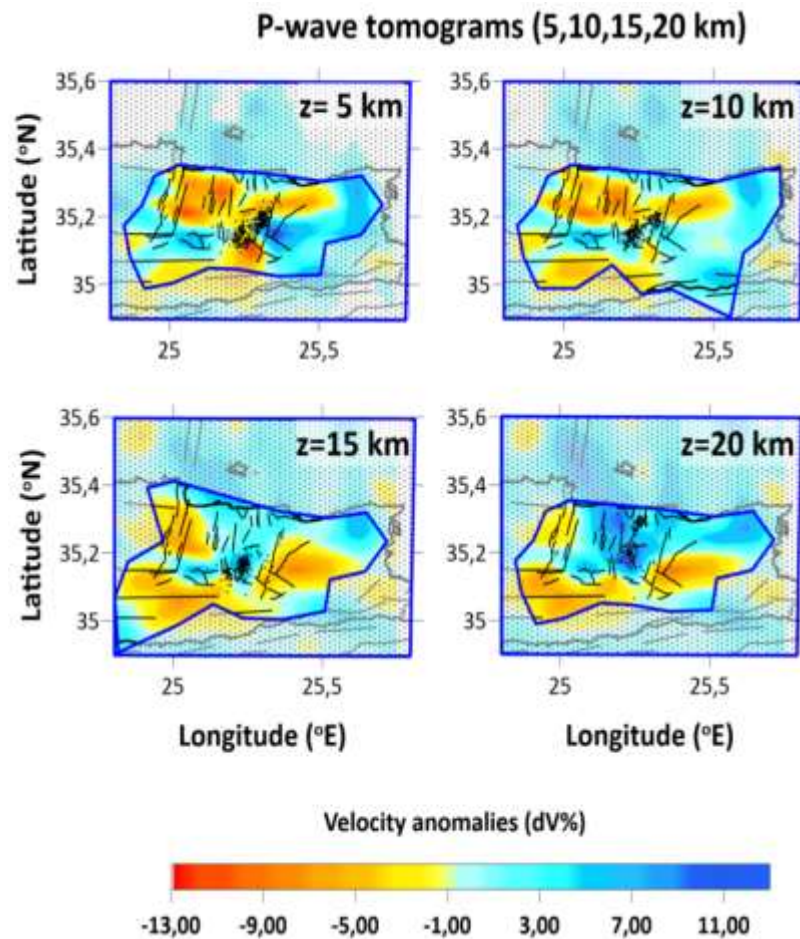


**Figure 6.** Lateral  $V_P$  (%) perturbations at 5, 10, 15 and 20 km depths. Areas with lower resolution are masked (darkened). Fault traces derived by [31].

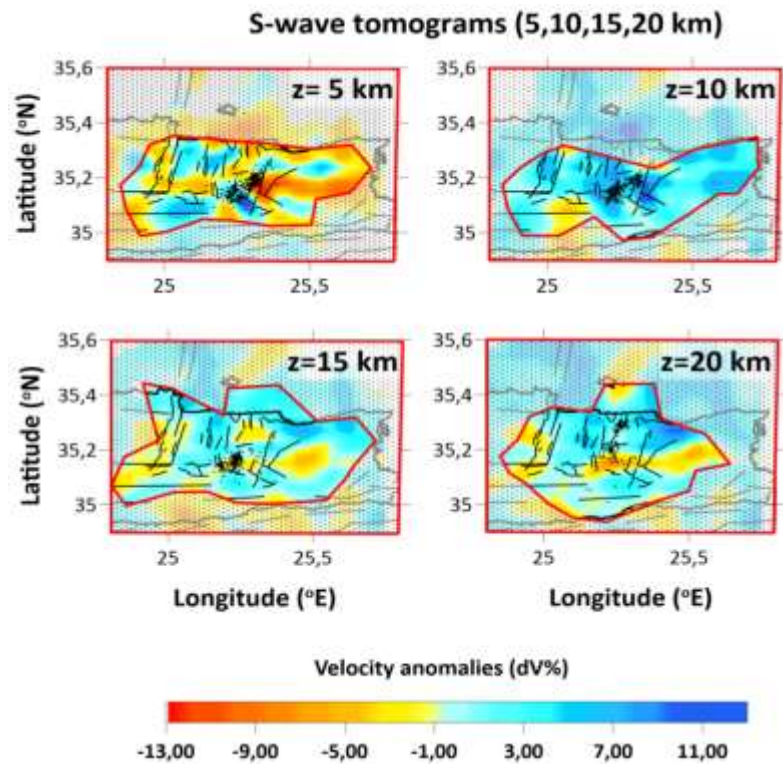


**Figure 7.** Lateral  $V_s$  (%) perturbations at 5, 10, 15 and 20 km depths. Areas with lower resolution are masked (darkened). Fault traces derived by [31].

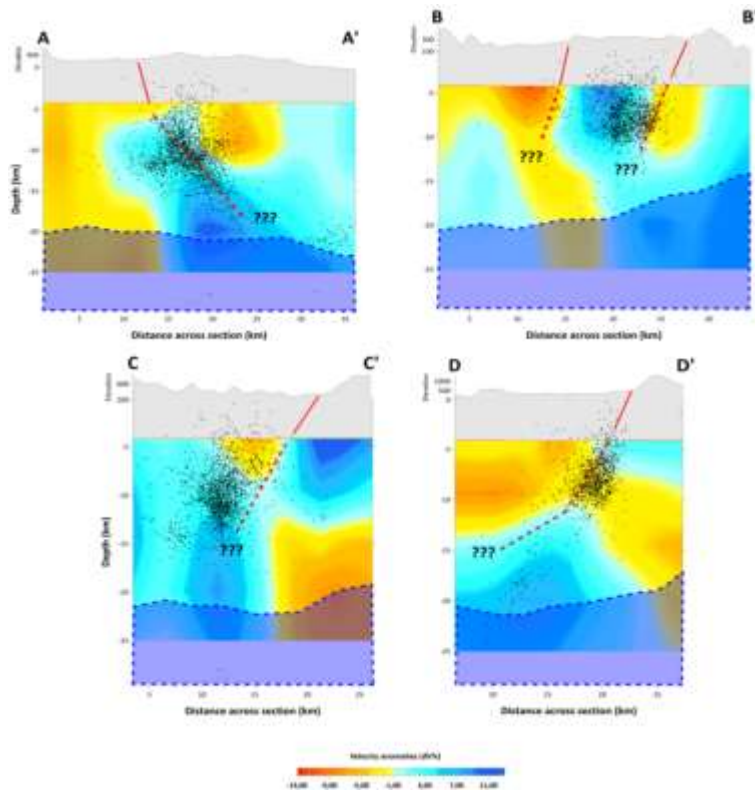


**Figure 8.** Cross-sections of  $V_p$  (%) perturbations. The cross-section traces are the same with the first four ones of Figure 5.

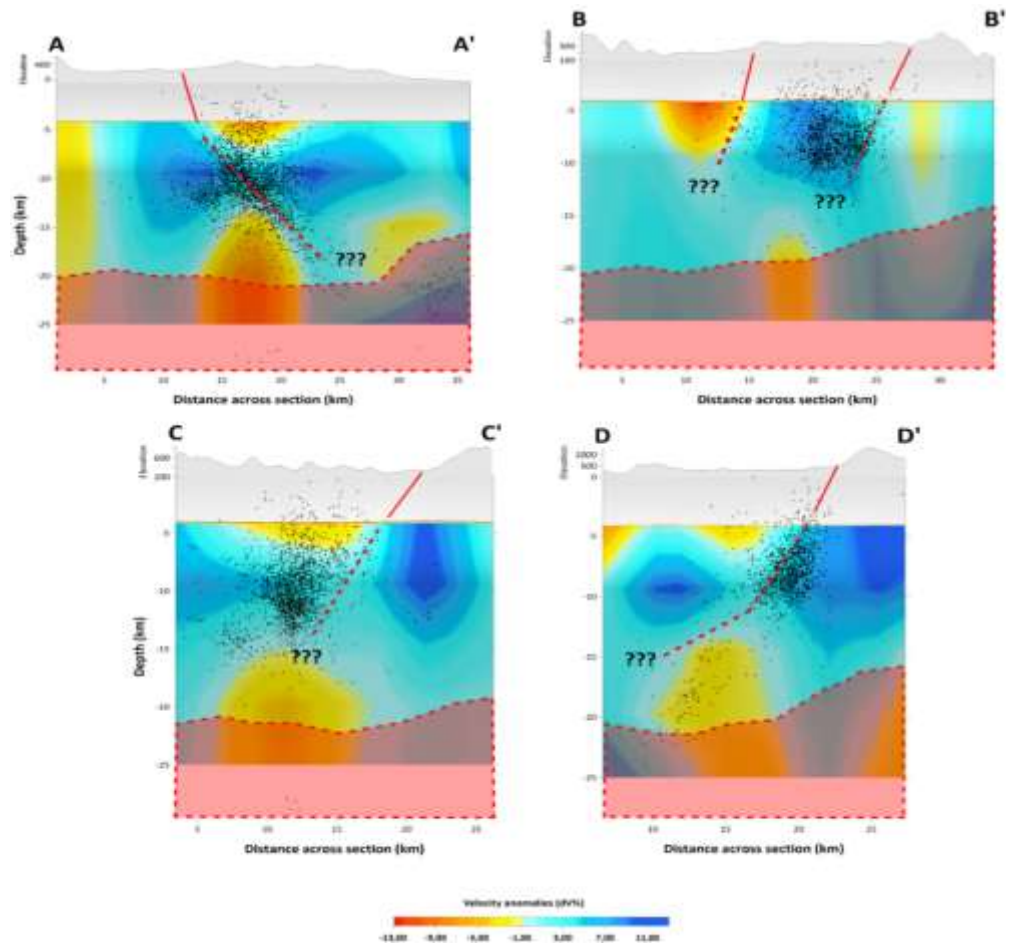


**Figure 9.** Cross-sections of  $V_s$  (%) perturbations. The cross-section traces are the same with the first four ones of Figure 5.

#### 4. Co-seismic Ground Deformation

To study the co-seismic ground deformation on the epicentral area of the September 27, 2021 event, we combined space and ground-based geodetic techniques. Radar satellite data were used to produce differential interferograms to spatially study the co-seismic deformation. Moreover, geodetic data from continuous Global Navigation Satellite System (GNSS) stations operating on the broad affected area provided point-wise accurate 3D displacement vectors.

##### 4.1 Interferometric Data and Results

The term SAR stands for Synthetic Aperture Radar [38]. Differential Interferometry (Differential InSAR technique-DInSAR) is an advanced technique [39] aimed at detecting surface movements due to geophysical phenomena or human interventions. Since the 1990s, the DInSAR technique has proven to be an interesting tool for measuring and observing ground deformation suitable for analyzing geodynamic processes e.g. [40-44].

To map the coseismic ground deformation due to the September 27, 2021 mainshock, we used two SAR image pairs, one on ascending and one on descending orbital geometries (Table 3), acquired from ESA's Sentinel-1A and Sentinel-1B satellites (<https://scihub.copernicus.eu/>). In both cases, the reference image was the one before the earthquake occurrence, while the repeat image was the one that refers to the date after the event. Each reference-repeat pair was processed using the ESA's SNAP software and two individual interferograms were generated. The topographic phase was subtracted using the SRTM 1 arc-second Digital Terrain Model, a 30-m resolution Shuttle Radar Topography Mission Digital Elevation Model (USGS 1 ARC-second SRTM DEM, <https://doi.org/10.5066/F7DF6PQS>), while the signal to noise ratio was enhanced by applying the adaptive power spectrum filter of [45] with a coherence threshold of 0.4.

**Table 3.** The main characteristics of the SAR images used in this study.

<b>Ascending Image Pair</b>						
<b>Satellite</b>	<b>Ref - Repeat</b>	<b>Acquisition</b>	<b>Track</b>	<b>Orbit</b>	<b>Bperp(m)</b>	<b>Btemp(days)</b>
S1B	Reference	23/09/2021	102	28828	-111.36	6
S1A	Repeat	29/09/2021	102	39899		
<b>Descending Image Pair</b>						
<b>Satellite</b>	<b>Ref. / Repeat</b>	<b>Acquisition</b>	<b>Track</b>	<b>Orbit</b>	<b>Bperp(m)</b>	<b>Btemp(days)</b>
S1A	Reference	25/09/2021	36	39833	-28.08	6
S1B	Repeat	01/10/2021	36	28937		

The two-phase wrapped interferograms were then used to estimate co-seismic ground deformation. To calculate the terrain displacement, an unwrapping process was performed, and the phase unit was transformed into distance units in the satellite line of sight (LoS) for each interferometric pair. Finally, decomposition of the ascending and descending LoS displacement vectors was performed to extract the vertical (up-down) and horizontal (east-west) ground deformation components.

The two wrapped interferograms are of good quality and contain the phase difference, between reference and repeat images, produced by the main seismic event and its aftershocks until the 29<sup>th</sup> of September. Due to the low temporal geometric baselines (six days), there are no areas of low coherence in the interferograms. Six fringes, forming a lobe, are evident both in ascending and descending wrapped phase interferograms (Figure 10, upper part). This asymmetrical displacement pattern is characteristic of normal-faulting earthquakes indicating that the subsidence is larger than the uplift. Each interference fringe is a phase change that corresponds to a motion of 2.8 cm in the satellite line of sight.

The LoS displacement map in the ascending geometry shows negative LoS displacement values up to 18 cm, after the Mw=6.0 earthquake including the ground deformation caused by all the seismic events that occurred in the time interval from 23/09 to 29/09, (Figure 10, lower part), while the LoS displacement map in the descending geometry shows negative LoS values up to 20 cm after the Mw=6.0 earthquake, including all the aftershocks, occurred until the 1st of October. On the descending orbital geometry, the maximum value of ground deformation has shifted east of the epicenter of the main earthquake (Figure 10) with respect to the ascending displacement map. After the decomposition of ascending and descending LoS displacement maps, the ground deformation in vertical (up-down) and east-west direction was extracted (Figure 11a). Subsidence up to 18 cm has been calculated from the displacement decomposition in the vertical (up-down) direction while no uplift was detected. The horizontal (east-west) displacement map reveals an eastward motion up to 6 cm in the area west of the epicenter and a westward movement up to 7.6 cm for the area east of Arkalochori (Figure 11b). The latter is in satisfactory agreement with [21] where the displacement is associated with the horizontal motion of strike-slip component of the mean event focal mechanism.

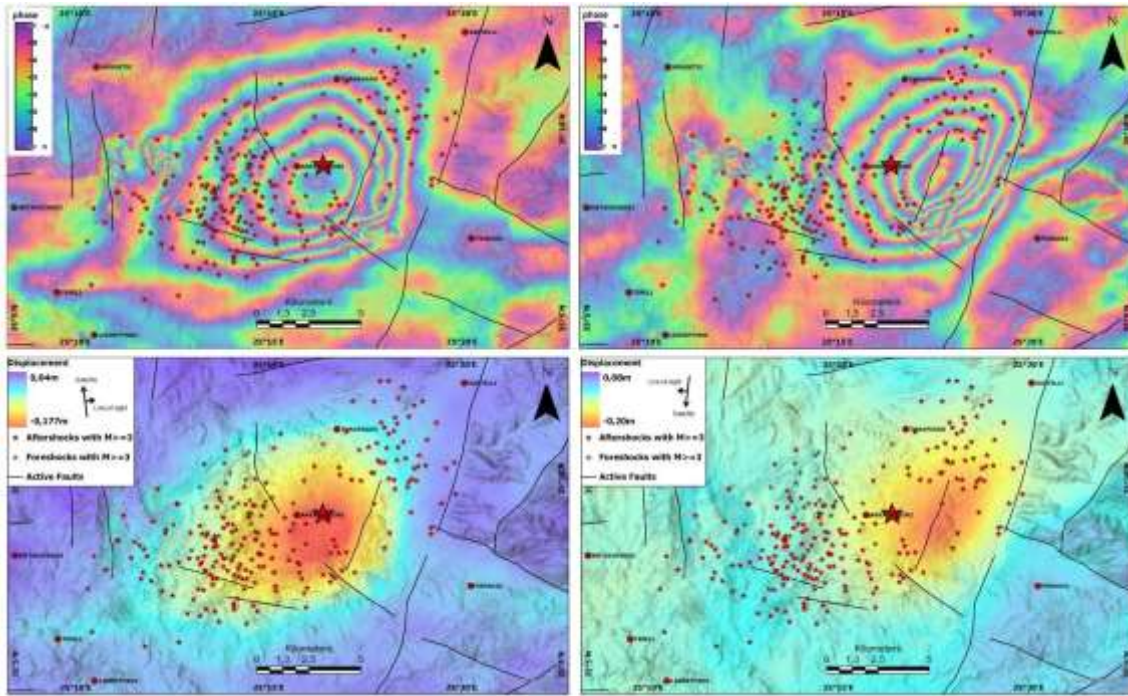


**Figure 10** Upper Maps: Wrapped ascending (left) and descending (right) co-seismic interferograms over the Arkalochori area. The interferograms are draped over shaded relief. Lower maps: Co-seismic displacement maps generated using the ascending and the descending image pairs and draped over shaded relief.

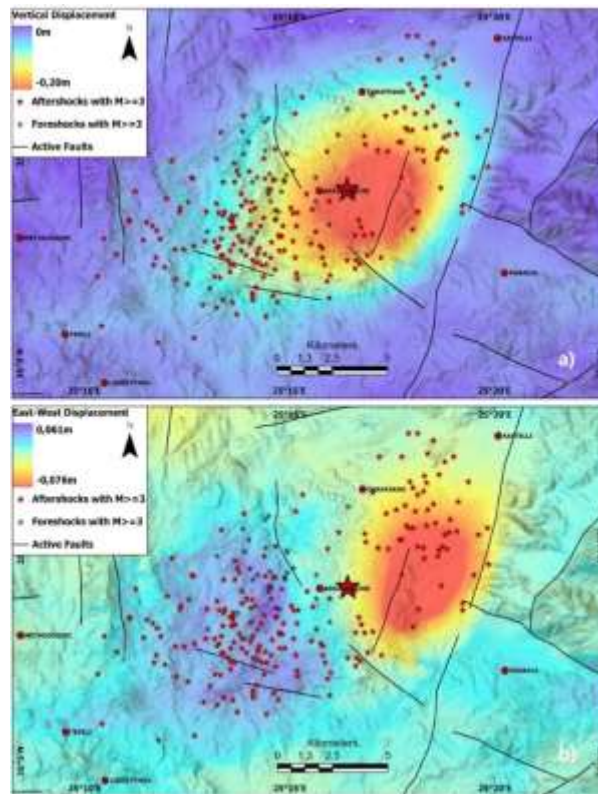


**Figure 11** Displacement maps for (a) the Vertical (Up-Down) and (b) the E-W displacement components for the Arkalochori earthquake overlain by the earthquakes with magnitude greater than 3 and the active faults of the broader area. Positive values on the E-W component indicate eastward motion, while the negative ones describe westward motion.

## 4.2 GNSS data and results

GNSS data from four continuous stations (belonging to the private network of METRICA SA) on the central-eastern part of Crete were used in the current study to measure the co-seismic displacement. One of the stations (ARKL) is located almost above the hypocenter of the main event, in Arkalochori. The other sites are located in the city of Heraclion (HERA station; ~24 km NNW of Arkalochori), in the village of Moires (MOI1 station; ~38 km WSW from epicenter) and in the Ierapetra region (IERA station; ~49 km ESE from the epicenter). Daily raw GNSS data from these four stations were processed for a period of several years before the 2021 seismic sequence up to April 30, 2022, using the Bernese v5.2 GNSS software [46].

In the processing procedure of the local GNSS data, several stations of the EUREF and IGS were included together with other auxiliary files. The absolute antenna phase center corrections were used, together with precise orbital solutions from the Center for Orbit Determination in Europe (CODE) and the Vienna Mapping Functions for the tropospheric modeling. For the coordinates estimation on static mode solutions, the precise double-difference method was used. For ambiguity resolution, numerous strategies were applied, based on the length of the formed baselines between the GNSS stations. The processing resulted in the estimation of high-precision station coordinates. Time series were formed, annual velocities prior to the 2021 seismic event were calculated and co-seismic displacements were determined. The daily coordinates of the GNSS stations were estimated on the global ITRF2014 reference frame.

Based on the formed time series of the stations' coordinates (Figure S5-S6), for the pre-seismic period, all the stations show SE horizontal linear type of motion (with respect to ITRF 2014) and subsiding vertical motion, consistent with the velocity field of the area [47]. Calculating the change in the baseline distance between the stations prior to the seismic sequence it is observed that a small extension pattern occurred in the area, since lengthening on the baselines was recorded of small amplitude (~1.5 mm/yr).

The main seismic event on Arkarochori caused, as it is expected strong ground displacement in the epicentral station ARKL as well as in the HERA station (Table 4). The vector of the co-seismic displacement was calculated as the static shift of the station coordinates nine days prior to and three days after the September 27, 2021 event, to minimize the effect of possible post-seismic motions. The higher displacement was recorded on the ARKL station, while noticeable displacement occurred in HERA site (Figure S5). The two other sites (MOI1 and IERA) have not shown any considerable co-seismic motion (Figure S6).

**Table 4** GNSS stations' coordinates and the respective vector of the co-seismic displacement.

Site	Latitude	Longitude	D <sub>East</sub> (cm)	D <sub>North</sub> (cm)	D <sub>Up</sub> (cm)
ARKL	35.1339	25.2689	4.51 ± 0.11	7.85 ± 0.14	-15.45 ± 0.60
HERA	35.4241	25.1415	-0.5 ± 0.09	0.62 ± 0.19	0.57 ± 0.39

The displacement vector on ARKL site shows a strong subsiding component of ~16 cm and significant eastward and northward horizontal motion. Both the E-W and the vertical components deduced by the GNSS analysis agree with the interferometric results. Small discrepancies in the amplitude of the components deduced by the two techniques may be attributed to the incompetence of the DInSAR to define the north motional component that is inherent in the LoS vector, and in our case is quite noticeable (~8 cm). The displacement vector on HERA station shows NW horizontal co-seismic motion and a noticeable upward vertical component.

The overall image of the ground deformation in the epicentral area, based on both interferometric and GNSS results, defines a strong subsiding pattern with substantial horizontal motional component compatible with normal faulting activated structure.

In the period following the mainshock and up to April 30, 2022, the two GNSS sites in Arkalochori and Heraklion city show increased velocity values, compared to the previous period, indicating that the post-seismic relaxation is continuous up to this date.

### 5. Spatial footprint of Coulomb stress changes

Numerous studies of strong earthquakes show a correlation between the positive lobe of Coulomb stress changes and the locations of the majority of the most significant aftershocks [e.g. 48, 49]. A moderate earthquake of magnitude  $M_w = 4.9$  occurred on July 24, 2021, 02:07:37 (UTC) accompanied of many aftershocks, before the main and catastrophic earthquake of magnitude  $M_w=6.0$  and its major aftershock of magnitude  $M_w=5.3$ , which took place on September 27, 2021, 06:17:21 (UTC) and September 28, 2021, 04:48:08 (UTC), respectively. Herein, we examine the co-seismic static stress changes with respect to the aftershocks spatial distribution during the event of  $M_w=4.9$ , the  $M_w=6.0$  main event as well as the  $M_w=5.3$  major aftershock. The  $\Delta CFS$  changes were determined via Coulomb3.3 software [50] in an elastic half-space and a uniform slip on the rupture planar surfaces.

The Coulomb Failure Stress changes ( $\Delta CFS$ ) is given by the equation (3):

$$\Delta CFS = \Delta\tau - \mu f \Delta\sigma \tag{3}$$

where  $\Delta\tau$  and  $\Delta\sigma$  are the in-shear stress and normal stress respectively, while the  $\mu f$  is the effective friction coefficient [51-53]. For the shear modulus and Poisson’s ratio, we used the values of 3.3 MPa and 0.25, respectively and a mean value for the coefficient of friction equal to  $\mu f = 0.4$  [54].

To calculate the subsurface fault’s width and length, we used the empirical relations of [55] for each modelled earthquake. In addition, we used the available focal mechanism solutions by various agencies, and we present our preferred models for this study in Table 5.

Figure 12 shows the determined co-seismic  $\Delta CFS$  changes caused by the event of magnitude  $M_w=4.9$  at centroid depth of 8.0 km and the vertical cross-sections AB and CD. The spatial distribution of the  $\Delta CFS$  reveals stress decrease towards NW and SE and stress increase towards NE and SW of the ruptured fault. The aftershocks during this period and before the main event of  $M_w=6.0$  are distributed mainly along and under the fault up to 20Km depth. The  $\Delta CFS$  values at the hypocentres of the  $M_w=6.0$  and  $M_w=5.4$  events were calculated, and the results provide -0.104 MPa and +0.0169 MPa, respectively. The co-seismic Coulomb stress variations caused by the strong earthquake of  $M_w=6.0$  and its major aftershock ( $M_w=5.4$ ) at centroid depths of 10.0 km and 9.0 km, respectively, as well as the spatial distribution of aftershocks are presented in Figures 13 and 14. For both seismic events, the same pattern on the spatial distribution of the  $\Delta CFS$  is observed, which indicates stress decrease towards NW and SE and stress increase towards NE and SW of the ruptured faults.

**Table 5** Focal parameters of  $M_w=4.9$ ,  $M_w=6.0$  and  $M_w=5.4$  events.

Date	Hour	Minute	Lat.	Long.	Depth (km)	$M_w$	Strike	Dip	Rake	Agency	Length	Width	$M_0$ (Nm)
24/7/2021	2	7	35.1676	25.2286	8	4.9	214	52	-95	NOA	2.3	2.56	$9.116 \times 10^{15}$
27/9/2021	6	17	35.1421	25.2734	10	6.0	218	57	-85	GFZ	7.61	10.3	$1.1 \times 10^{18}$
28/9/2021	4	48	35.1356	25.2312	9	5.3	182	22	-95	UOA	4.41	4.88	$1.30 \times 10^{17}$

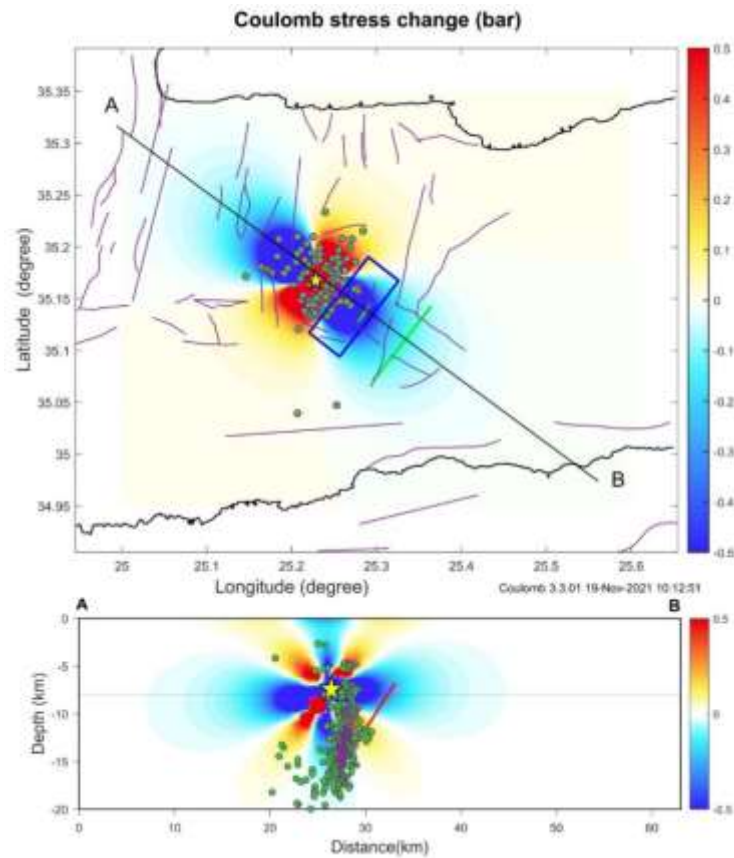


**Figure 12** (Up) Coulomb stress changes distribution due to Mw=4.9 event (yellow star) at centroid depth of 8.0 km. The red rectangle indicates the fault model for the kinematics of Mw=4.9 while the blue one is the projection of the fault model of Mw=6.0 main shock (listed in Table 3). (Down) Coulomb stress changes along the vertical cross-section AB. The green circles are the relocated hypocenters of the aftershocks which occurred after the Mw=4.9 and before the major earthquake Mw=6.0. The green lines show the surface projections of the two fault models.

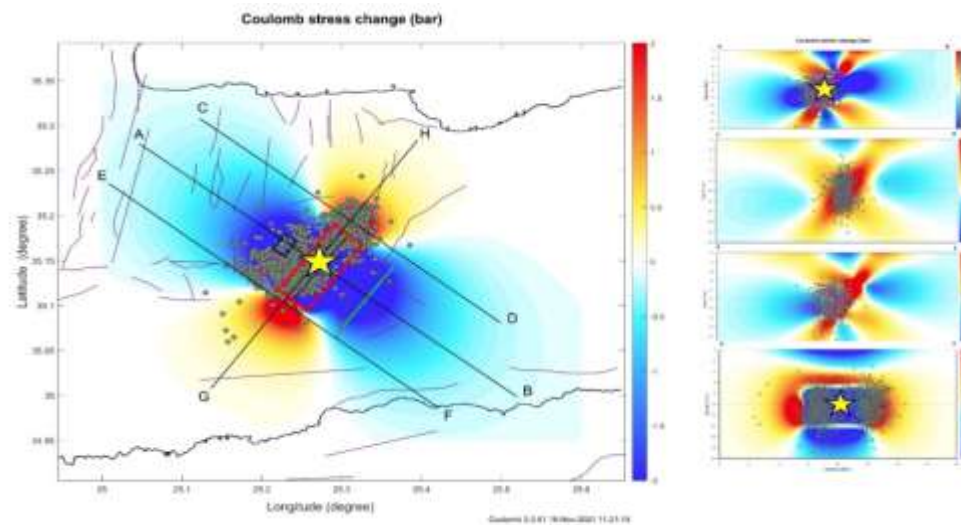


**Figure 13** (Left) Coulomb stress changes distribution due to Mw=6.0 event (yellow star) at centroid depth of 10.0 km. The red rectangle indicates the fault model for the kinematics of Mw=6.0 while the blue one is the projection of the fault model of Mw=4.9 event (listed in Table 3). (Right) Coulomb stress changes along the vertical cross-sections A-B, C-D, E-F and the parallel cross-section G-H (from up to down). The green circles are the relocated hypocenters of the aftershocks which occurred after the Mw=6.0 main shock. The green lines show the surface projections of the two fault models.

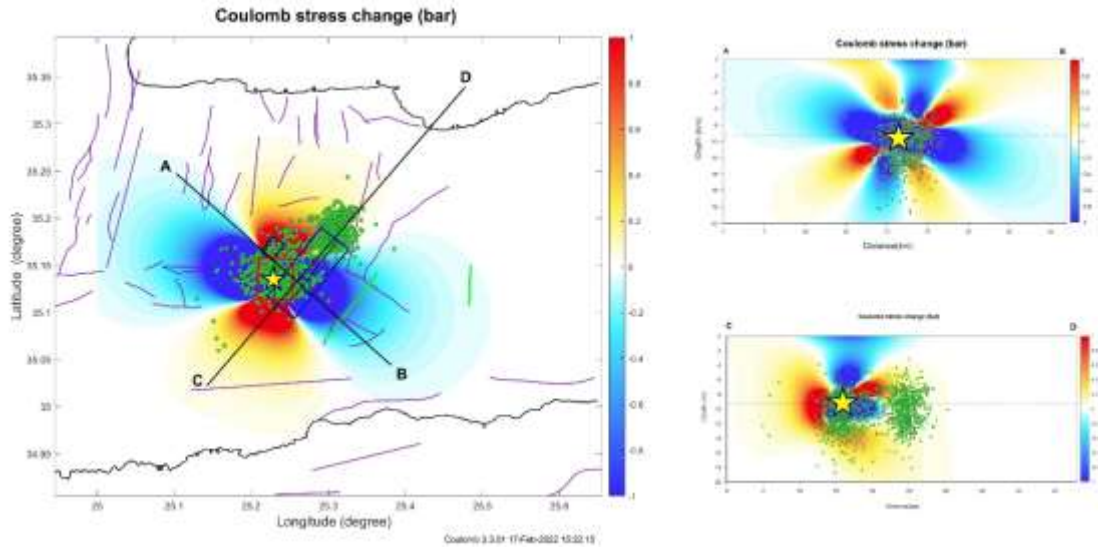


**Figure 14** (Left) Coulomb stress changes distribution due to Mw=5.4 major aftershock (yellow star) at centroid depth of 9.0 km. The red rectangle indicates the fault model for the kinematics of Mw=5.4 while the blue ones are the projections of the fault models of Mw=4.9 and Mw=6.0 events (listed in Table 3). (Right) Coulomb stress changes along the cross-sections AB, CD. The green circles are the relocated hypocenters of the aftershocks which occurred after the Mw=6.0 main shock. The green lines show the surface projections of the two fault models.

The focal mechanism of the mainshock was related to normal faulting and only a small portion of the strike-slip component was involved. A similar solution is evident for the largest foreshock ( $M_w$ 4.9) and aftershock ( $M_w$ 5.3) (Table 5) although, in the latter, the strike-slip component is increased.

From the obtained co-seismic  $\Delta$ CFS changes we thus observe that most aftershocks, including those of greater magnitude, occurred within positive static stress changes produced by the major earthquake, and by the strongest aftershock. This suggests that the spatial distribution of aftershocks, including the significant ones, are controlled by the co-seismic Coulomb stress changes produced during the Mw=6.0 mainshock and the major events of the sequence.

## 6. Frequency-Magnitude scaling properties of the foreshock and aftershock sequences in terms of non-extensive statistical physics

The frequency – magnitude distribution (FMD), known as G-R law [56], is of vital importance for the characterization of a seismic sequence [56-69] and is expressed by equation (4):

$$\log N = a - bM \quad (4)$$

where  $N$  is either the discrete frequency of magnitudes  $M$  in each magnitude bin, or the cumulative frequency of magnitudes  $\geq M$ ;  $\alpha$ ,  $b$  are parameters determined by the earthquake catalog data, and the slope  $b$  of the G-R law expresses the relative number of the small magnitude earthquakes to the large magnitude ones and  $\alpha$  is a measure of the seismicity level. In terms of geophysics, the  $b$ -value is considered as a stress meter e.g. [58]. In this context, low  $b$  indicates high material heterogeneity and concentrated stress while high  $b$  implies asymmetrically distributed stress. For details on the  $b$ -values for the Arkalochori seismic sequence see [21].

An alternative model that describes the frequency-size distribution of earthquakes from the first principles of non-extensive statistical physics (NESP) introduced in [70]. This model is based on Tsallis Entropy, a generalization of Boltmann-Gibbs one [71] that offers a coherent theoretical framework for analyzing complex dynamical systems with fractal features and long-range correlations [72]. In the approach introduced in [70] considers that the seismic energy  $E$  is related to the size of the fragments that fill the space between the activated fault blocks. Then, by considering that the earthquake magnitude is related to the radiated seismic energy as  $M = \frac{2}{3} \log E$ , the cumulative distribution function  $N(>M)$  of earthquake magnitudes  $M$  can be deduced as [73]:

$$\frac{N(>M)}{N} = \left[ 1 - \left( \frac{1-q_m}{2-q_m} \right) \left( \frac{10^M}{\alpha_m^{2/s}} \right)^{\frac{2-q_m}{1-q_m}} \right] \quad (5)$$

where  $q_m$  is the entropic index and  $\alpha_m$  a model parameter that expresses the proportionality between the seismic energy and the size of the fragments. In [74] updated the derived equation to include the minimum earthquake magnitude  $M_0$  in a seismic catalog, which now reads as:

$$\frac{N(>M)}{N} = \frac{\left[ 1 - \left( \frac{1-q_m}{2-q_m} \right) \left( \frac{10^M}{\alpha_m^{2/s}} \right)^{\frac{2-q_m}{1-q_m}} \right]}{\left[ 1 - \left( \frac{1-q_m}{2-q_m} \right) \left( \frac{10^{M_0}}{\alpha_m^{2/s}} \right)^{\frac{2-q_m}{1-q_m}} \right]} \quad (6)$$

The derived model, in the form of Eq.6, has extensively been used to describe the earthquake dynamics of local and regional seismicity [e.g. 75-86]. In comparison to the Gutenberg–Richter (G-R) scaling law, the FA model provides a reasonable explanation of recorded earthquake magnitudes over a wider range of scales, while the  $b$ -value may be obtained as a special case for values over a certain threshold magnitude [75,86] as:

$$b = \frac{(2-q_E)}{(q_E-1)}$$

The result of the application of the NESP model (Eq.6) to the observed cumulative distributions  $N(>M)$  of earthquake magnitudes for the foreshock and aftershock sequences of the Mw=6.0 mainshock, as well as for the NE and SW spatial clusters, are shown in Figure 15. The model provides a good fit to the observed distributions over the entire range of magnitudes, for the model parameters referred in Table 6 and Figure 15. The greater  $q_m$  value for the SW cluster indicates greater tectonic instability in this region where the mainshock and the major aftershocks occurred.

**Table 6** Parameter values for the foreshock and aftershock sequences in Arkalochori, as well as for the NE and SW aftershock clusters. N is the number of events (with  $M \geq M_c$ ),  $M_c$  the magnitude of completeness,  $\alpha_m$ ,  $q_m$  the parameters of the NESP model (Eq.6) and  $\tau_0$ ,  $q_\tau$  the parameters of the q-exponential function for the inter-event times distribution (Eq.10).

	$N$	$M_c$	$\alpha_m$	$q_m$	$\tau_0$	$q_\tau$
Foreshocks	410	2.8	3005 ±734	1.46 ±0.02	732.2 ±47.9	1.72 ±0.11
Aftershocks (both NE and SW clusters)	4465	2.5	384 ±99	1.50 ±0.01	69.2 ±12.3	1.78 ±0.09
NE cluster	1815	2.5	518 ±84	1.43 ±0.01	204.9 ±12.4	1.81 ±0.12
SW cluster	2431	2.5	409 ±101	1.53 ±0.01	61.8 ±4.3	2.16 ±0.17

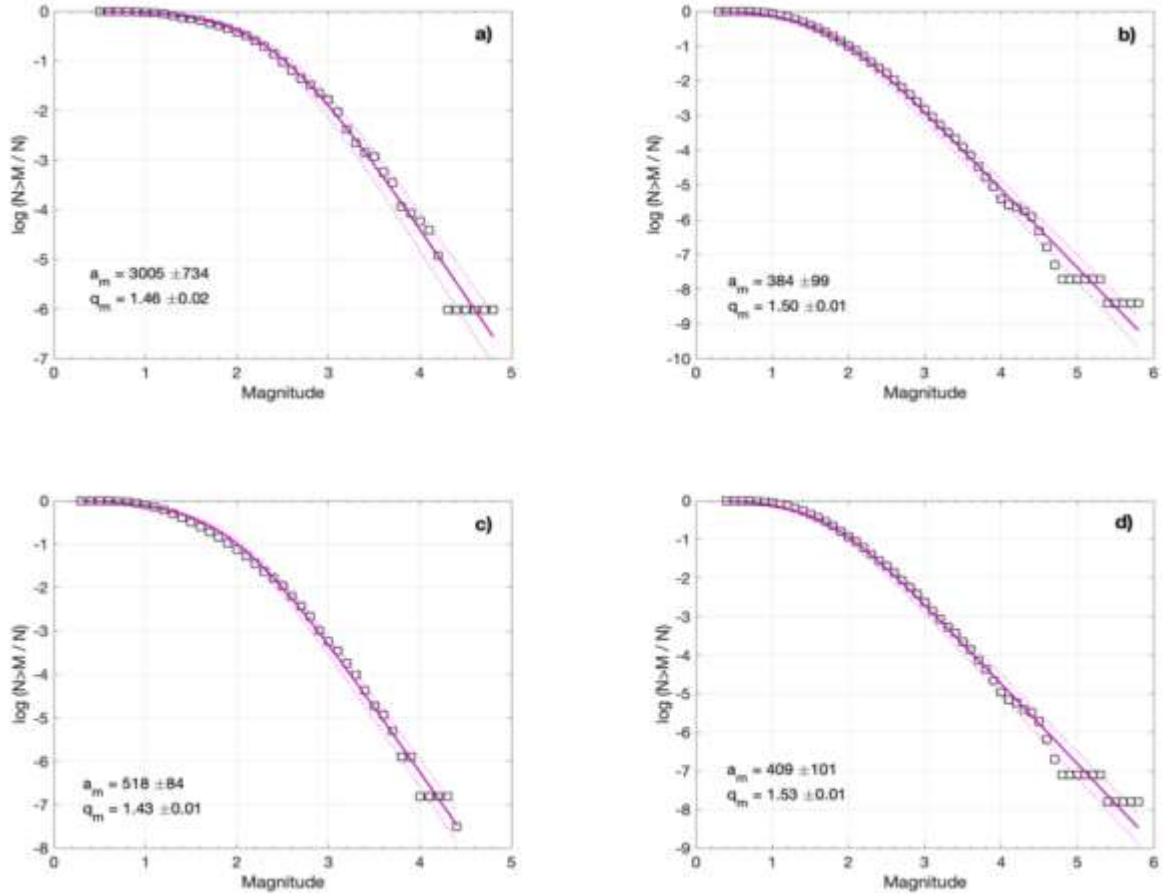


**Figure 15** The frequency-magnitude distribution of earthquakes (squares) for the a) foreshock sequence, b) aftershock sequence, c) NE aftershocks cluster, d) SW aftershocks cluster. The corresponding fit according to Equation (6) is shown with the solid line, for the parameter values shown in the down left corner and Table 6. The dotted lines represent the 95% confidence intervals.

### 6.3 Temporal properties of the aftershock sequence

#### 6.3.1 Aftershock production rate and modelling

It has long now been recognized that the number of aftershocks following a major event resembles a power-law decay with time that expresses the relaxation process after the mainshock. This mathematical relationship takes the form of the so-called modified Omori's scaling law [87,88]:

$$n(t) = K(t + c)^{-p}, \quad (7)$$

where  $n(t)$  is the production rate of aftershocks  $n(t) = dN(t)/dt$ ,  $N(t)$  is the number of aftershocks in time  $t$  after the mainshock,  $K$  and  $c$  are constants and  $p$  the power-law exponent that usually takes values in the range  $0.9 < p < 1.6$  [89]. Moreover, the cumulative frequency of aftershocks  $N(t)$  is estimated from  $n(t)$  as:

$$N(t) = \int_0^t n(s) ds = \begin{cases} K[c^{1-p} - (t+c)^{1-p}]/(p-1), & \text{for } p \neq 1 \\ K \ln(t/c + 1), & \text{for } p = 1 \end{cases} \quad (8)$$

Herein, we use the previous equation to model the evolution of the aftershocks in terms of the cumulative frequency of aftershock activity that followed the Mw6.0 mainshock. We focus on the two major aftershocks clusters, the NE and SW spatial clusters that were discussed previously and apply the maximum likelihood method to estimate the model parameters of Eq.8 [90]. In Figure 16 the cumulative number of aftershocks (for  $M \geq M_c$ ) with time is shown for the two spatial clusters along with the modified Omori's law (Eq.8), which generally provides a fair fit for the parameter values given in Table 7. However, large aftershocks may trigger secondary aftershock sequences

embedded in the aftershock sequence of the mainshock. In this case, several Omori regimes may be used to model the aftershocks production rate  $n(t)$  [89-91]:

$$n(t) = K_1(t + c_1)^{-p_1} + H(t - t_2)K_2(t - t_2 + c_2)^{-p_2} + H(t - t_3)K_3(t - t_3 + c_3)^{-p_3}, \quad (9)$$

where  $H(\cdot)$  denotes a unit step function and  $t_2, t_3$  indicates the occurrence times of secondary aftershock sequences. In Figure 16, breaks are observed in the cumulative number of aftershocks for both spatial clusters that are associated with strong aftershocks and the generation of secondary aftershock sequences. Hence, we investigate if the composite model of Eq.9 fits better the observed distribution. By setting  $t_2=22.8$  days and  $t_3=67.4$  days that designate the occurrence times of strong aftershocks following the main shock for the NE cluster (Table 7), we find that the composite model provides a better fit to the observed distribution (Figure 16), which is further confirmed by the smaller Akaike Information Criterion (AIC) value in comparison to the single Omori regime (Table 7).

**Table 7** The considered mainshock, the duration (in days), the number of events (N) and the MLE of the modified Omori formula parameters for the NE and SW aftershock clusters, along with their associated uncertainties. AIC is the estimated Akaike Information Criterion for each model.

Cluster	Model	Mainshock	Duration (days)	N	K	c (days)	p	AIC
NE cluster	Single model	M5.8 27/09/21	119.3	256	71.02 ±14.45	28.35 ±0.57	1.85 ±0.08	-72.4
	Composite model	M5.8 27/09/21	22.8	120	10.57 ±7.18	0.01 ±1.63	0.35 ±0.12	-125.7
		M4.3 20/10/21	44.6	92	10.95 ±3.98	0.24 ±0.65	0.66 ±0.06	
		M3.7 03/12/21	51.9	44	11.57 ±8.56	1.50 ±1.63	1.10 ±0.28	
SW cluster	Single model	M5.8 27/09/21	114.8	446	165.65 ±126.80	1.76 ±1.33	1.18 ±0.16	-1130
	Composite model	M5.8 27/09/21	24.1	290	81.09 ±35.98	0.67 ±1.15	1.01 ±0.36	-1304
		M4.5 21/10/21	8.7	68	12.00 ±4.66	0.01 ±0.11	0.86 ±0.19	
		M3.7 03/12/21	82.0	88	10.00 ±4.55	0.26 ±0.32	0.77 ±0.08	

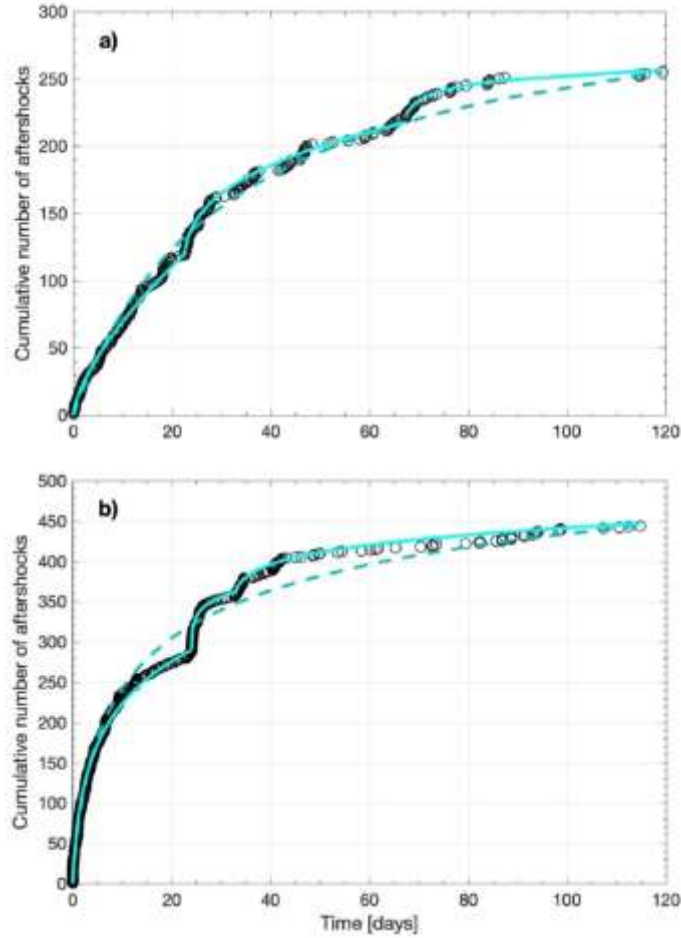


**Figure 16.** The cumulative number of events for  $M \geq M_c$  (symbols) with time that followed the  $M_w 6.0$  mainshock in the a) NE cluster and b) the SW cluster. The solid lines represent the composite model of three modified Omori regimes, while the dashed line the model for a single modified Omori regime, for the parameter values shown in Table 7.

A similar result is obtained for the SW cluster. In this case, we used  $t_2=24.1$  days and  $t_3=32.8$  days that mark the occurrence times of strong aftershocks in the SW cluster (Table 7). The composite model provides a better fit to the observed distribution, in comparison to the single Omori regime, for the parameter values given in Table 7.

### 6.3.2 The interevent times distributions for the foreshock and aftershock sequences

Furthermore, we study the temporal scaling properties of the foreshock and aftershock sequences by investigating the interevent times (or waiting times) distributions between the successive events. In this analysis, earthquakes are considered as a point process in time, marked by the magnitude of the event, with interevent times  $\tau$  between the successive events defined as  $\tau_i = t_{i+1} - t_i$ , where  $t_i$  is the time of occurrence of the  $i$ th event  $\{i = 1, 2, \dots, N-1\}$  and  $N$  the total number of events. First, we construct the cumulative distribution of the interevent times ( $M \geq M_c$ ) for the foreshock and aftershock sequences, as well as for the NE and SW spatial clusters. We then model the observed distributions with the  $q$ -exponential function, derived in the framework of NESP [72, 82, 84, 86, 92-96]. It has been shown in various studies that the  $q$ -exponential function appropriately describes the distribution of interevent times in global, regional, and volcanic earthquake activity, as well as in aftershock sequences [73-86, 91-96].

If  $P(>\tau) = N(>\tau)/N_0$  is the cumulative distribution function (CDF) of the interevent times, with  $N(>\tau)$  the number of

interevent times with value greater than  $\tau$  and  $N_0$  their total number, then the  $q$ -exponential cumulative distribution is given by [92]:

$$P(> \tau) = \exp_q\left(-\frac{\tau}{\tau_0}\right), \quad (10)$$

where  $\tau_0$  is a constant in time units and  $\exp_q(x)$  is the  $q$ -exponential function defined as:

$$\exp_q(x) = [1 + (1 - q)x]^{1/(1-q)}, \quad (11)$$

when  $1+(1-q)x \geq 0$  and  $\exp_q(x)=0$  in all the other cases. Its inverse is the  $q$ -logarithmic function:  $\ln_q(x) = \frac{1}{1-q}(x^{1-q} - 1)$ . In the limit of  $q \rightarrow 1$ , the  $q$ -exponential and  $q$ -logarithmic functions lead to the ordinary exponential and logarithmic functions, respectively.

In Figure 17, we present the cumulative distributions  $P(>\tau)$  for the foreshock and aftershock sequences and for the two spatial clusters in log-log plots. In all four cases, the  $q$ -exponential cumulative distribution (Eq.10) provides a good fit to the observed distributions for the parameter values given in Figure 17 and Table 6. This is further confirmed by the expected linear dependence of corresponding  $q$ -logarithmic distributions  $\ln_q P(>\tau)$  with  $\tau$  [77], that are shown in the right panels of Figure 17. In all cases, the  $q$ -logarithmic function describes the observed distributions with high correlation coefficients, shown in the corresponding panels. The high values of  $q_\tau$  (Table 6) indicate long-range temporal correlations in the evolution of the earthquake activity and further confirm the high  $q_\tau$  values observed in aftershock sequences [84, 96-98].

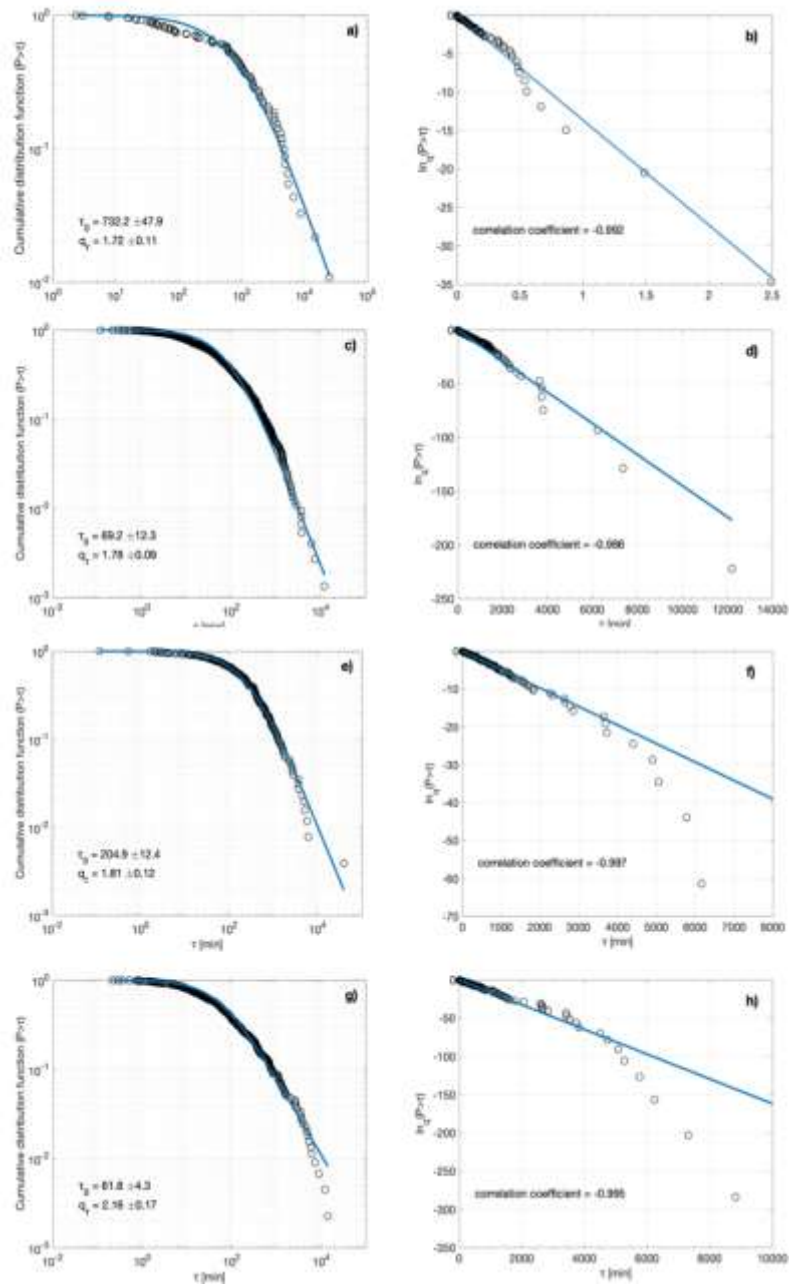


**Figure 17** The cumulative distribution function  $P(>\tau)$  of the inter-event times  $\tau$  (in minutes) (left panels) and the corresponding  $q$ -logarithmic function (right panels), represented by circles, for the a, b) foreshock sequence, c, d) aftershock sequence, e, f) NE aftershocks cluster, g, h) SW aftershocks cluster. Fitting with the  $q$ -exponential function (Eq.10) is shown with the solid lines, for the parameter values and the corresponding correlation coefficients shown in the down left corners.

#### 6.4 Scaling of the aftershocks focal zone with time

The growth of the aftershocks focal zone with time can provide valuable information regarding the triggering mechanisms of earthquake migration. This migration pattern observed in many cases frequently scales as the logarithm of time [97-102]. Various studies, based on numerical simulations [103, 104], as well as on real cases [97,105], suggest that this logarithmic migration pattern signifies that aftershocks migration is driven by afterslip. In this case, aftershocks are generated as the outcome of afterslip propagation along the activated fault. To anticipate the growth of the aftershocks focal zone with time as the outcome of afterslip, [106] have recently introduced a numer-

ical model. In this model, asperities on a fault are stressed initially by regional creep occurring at a steady deformation rate during the inter-seismic period. As the mainshock occurs, some of the asperities slip co-seismically, transferring large positive Coulomb stresses to the surrounding creeping regions. During the post-seismic phase, the stress-loaded regions can accommodate large amounts of afterslip and when a critical level of afterslip is reached, aftershocks are triggered. Static stress changes in the model are thought to trigger aftershocks only during the early post-seismic phase, so that most aftershocks are triggered by afterslip. In this case, the seismicity rate  $R(t)$  can then be proportional to the afterslip rate  $V(t)$  [103, 106, 107]:

$$V(t) = \frac{V_+ \exp(t/t_r)}{1 + \left(\frac{V_+}{V_L}\right) [\exp(t/t_r) - 1]} \quad (12)$$

where  $V_+$  and  $V_L$  are the sliding velocity just after the end of co-seismic rupture and the long-term loading velocity after the mainshock and  $t_r$  the duration of the post-seismic phase. Considering the previous equation, the seismicity rate  $R(t)$  can then be given by:

$$R(t) = \frac{R_+ \exp(t/t_r)}{1 + \left(\frac{R_+}{R_L}\right) [\exp(t/t_r) - 1]} \quad (13)$$

where  $R_+$  and  $R_L$  are the seismicity rates just after the end of co-seismic rupture and the long-term one after the mainshock, respectively. If  $\tau$  is the stressing rate and  $\Delta CFS$  the co-seismic Coulomb stress changes induced by the mainshock, then the parameters  $t_r$  and  $R_+$  are given by  $t_r = A'/\tau$  and  $R_+ = R_L \exp(\Delta CFS/A')$ , where  $A' = (a - b)\sigma$ , with  $a$  and  $b$  the rate and state frictional parameters and  $\sigma$  the effective normal stress. For  $t/t_r \ll 1$ , Equation 13 yields a decay rate for  $R(t)$  proportional to  $1/t$ , which is consistent with a modified Omori decay rate with  $p=1$  [87].

With the previous assumptions, the distribution of afterslip velocities can be deduced. Initially, a fault with only depth varying normal stress, stressing rate and rheological parameter  $A'$  is considered. If the initial Coulomb stress field varies with the strike direction  $x$ , then aftershocks migrate along  $x$ , forming the initial distribution of afterslip velocities. Then, the propagation velocity  $V_p$  of the aftershocks focal zone, on the early stage of the post-seismic phase that typically lasts several weeks or months after the mainshock, is given by [103]:

$$V_p = \frac{A'}{t} \times \left( -\frac{\partial \Delta CFS}{\partial x} \right)^{-1} \quad (14)$$

The expansion of the aftershocks zone  $L_a$  between time  $t_i$  and  $t$  ( $t > t_i$ ) is now given by:

$$\Delta L_a(t) = L_a(t) - L_a(t_i) = A' \times \left( -\frac{\partial \Delta CFS}{\partial x} \right)^{-1} \ln \left( \frac{t}{t_i} \right) \quad (15)$$

The latter equation manifests the logarithmic expansion of the aftershocks zone with time and for a smooth co-seismic Coulomb stress field, implies its slow migration.

Since the estimated co-seismic Coulomb stress field  $\Delta CFS$  (Equation 3) can be significantly different from the “real” one, In [103] suggested a mean Coulomb stress gradient to be used. In this case Eq.15 becomes:

$$\langle \Delta L_a(t) \rangle = A' \times \left\langle \left( -\frac{\partial \Delta CFS}{\partial x} \right)^{-1} \right\rangle \ln \left( \frac{t}{t_i} \right) = \zeta A' \frac{l_c}{\Delta \sigma} \ln \left( \frac{t}{t_i} \right) \quad (16)$$

In the latter equation,  $l_c$  is the radius of the co-seismic rupture,  $\Delta \sigma$  the mean value of the mean co-seismic stress drop and  $\zeta$  a constant. For an idealized Coulomb stress field,  $\zeta$  takes the value of 2.77 [103].

In the light of the previously described model, we investigated the scaling properties of the aftershocks focal zone with time for the Arkalochori aftershock sequence. In the analysis, we used the relocated catalogue for the events with  $M \geq M_c = 2.5$  to estimate the mean distance of aftershocks from the mainshock  $\langle \Delta L_a(t) \rangle$  with time  $t$ , along the horizontal dimensions. The result is shown in Figure 18, as a function of the logarithm with time. The expansion of the aftershocks zone becomes apparent, as  $\langle \Delta L_a(t) \rangle$  grows systematically with time after the surpass of one day from the mainshock. This growth can well be described by the afterslip front (Eq.16) for over a period of one hundred days ( $R_2=0.97$ ). We note that the logarithmic time dependence starts almost after the first day from the main event, possible suggested that after that time the system is starts driven by an after slip process.

Furthermore, from Eq.16 the rheological parameter  $A'$  can be determined once the slope  $s_a$  of the afterslip front is known. From Figure 18, we get  $s_a = 0.320 \pm 0.003$ . Then, from Eq.16,  $s_a = \frac{d\langle L_a(t) \rangle}{d \ln t} = \zeta A' \frac{l_c}{\Delta \sigma}$ , where  $l_c$  is the radius

of the co-seismic rupture and  $\Delta\sigma$  the co-seismic stress drop. For a simple model of circular rupture,  $l_c$  can approximately be determined as  $l_c = \left(\frac{7 M_0}{2 \Delta\sigma}\right)^{1/3}$  [51]. The average stress drop for normal fault earthquakes in Greece is  $\Delta\sigma = 5.5 \pm 1.5$  MPa [108, 109], while the mainshock's seismic moment is  $M_0=1.1E+18$  Nm (Table 4) [21-23]. Then, we estimate the value of  $l_c \approx 8.9$  km for the co-seismic rupture. For  $\zeta=2.77$ , the rheological parameter  $A'$  takes the value of  $A' \approx 0.71$  MPa, which is within the range 0.1 – 1 MPa of  $A'$  values that are usually found [97, 98, 103]. This value is considerably higher than other  $A'$  values that were estimated for recent normal fault mainshocks in Greece, as [97] estimated  $A' \approx 0.041$  MPa for the 2020 Mw7.0 Samos earthquake, while [98] estimated the value of  $A' \approx 0.29$  MPa for the 2021 Mw6.3 Northern Thessaly earthquake.

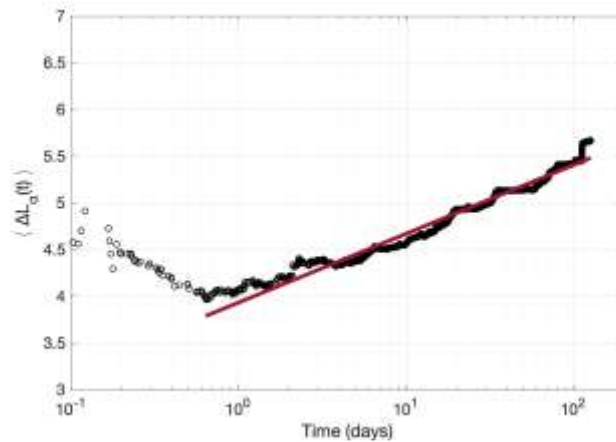


**Figure 18.** The average expansion (in km) of the aftershock zone as function of the logarithm of time (symbols) for Central Crete 2022, Mw6.0 aftershock sequence. The solid line represents the logarithmic growth of the aftershocks zone.

## 7. Concluding remarks

The 2021 Arkalochori earthquake is a characteristic event in the time history of Central Crete. The main event of September 27, 2021 Mw6.0 was a reminder that strong earthquakes do occur onshore Crete. In the present work the patterns and the scaling properties of the 2021 – 2022 earthquake sequence that occurred at Central Crete, are presented.

A relocation procedure has managed to improve the relative locations of the foreshock epicenters, which are concentrated in the vicinity of the September 27<sup>th</sup> mainshock. The mainshock apparently broke a large asperity of a west-dipping normal fault and distributed stresses towards its northern and southern edges, triggering aftershocks mainly at two large groups, separated by a spatial gap, where the asperity was located. Similar cases have been previously reported in other significant earthquakes on normal faults in Greece, including the 1999 Athens [110], the 2017 Kos [111,112], and the 2020 Samos [113,114] earthquakes.

Strong NW-SE and E-W oriented negative velocity anomalies predominate at both the upper and the lower crust of Central Crete. These are observed down to 15 km depth at the tomograms presented. At the depth slice of 5 km, a NE-SW-trending zone of negative body-wave velocity perturbations appears near the epicentral region of the Mw=6.0 Arkalochori earthquake. This anomaly follows the mean distribution of Alluvial deposits and post-alpine sediments which are bounded by positive (~13%) body-wave velocity perturbations, possibly connected to the older post-alpine sediments of Viannos formation and the Mesozoic carbonate rocks to the east and south of Arkalochori basin, respectively. In the area north of Arkalochori, an E-W-trending anticorrelated pattern of negative P- and positive S-wave velocity anomalies are observed at the depth range of 5-10 km. This anomaly coincides with the eastward bending of Kastelli normal fault direction, from the area east of Arkalochori towards the town of Malia. In the depth slice of 15 and 20 km, an almost NNE-SSW discontinuity of positive to the west and negative to the east VP anomalies is identified along the west-dipping Agnos normal fault. Furthermore, cross-sections created in

both primary (P) and secondary (S) wave velocity anomalies, reveal this west-dipping structure that may be related to Agnos high-angle ( $\sim 60^\circ$ ) normal fault.

The co-seismic Coulomb stress variations caused by the strong earthquake of  $M_w=6.0$  and its major foreshock and aftershock, as well as the spatial distribution of foreshocks and aftershocks are presented. For all the major seismic events analyzed, the same pattern on the spatial distribution of the  $\Delta CFS$  is observed, which indicates stress decrease towards NW and SE and stress increase towards NE and SW of the ruptured faults. The spatiotemporal evolution of the sequence indicated triggering of seismicity throughout most of the aftershock zone soon after the mainshock, attributed to coseismic stress transfer, followed by slower migration towards its outer edges, indicating possible afterslip.

A straightforward interpretation of horizontal motion patterns derived from the DInSAR analysis is mainly in agreement with the aftershock distribution and clustering. The displacement vector on ARKL site show strong subsiding component of  $\sim 16$  cm and significant eastward and northward horizontal motion. Both the E-W and the vertical components deduced by the GNSS analysis agree with the interferometric results. The overall image of the ground deformation in the epicentral area, based on both interferometric and GNSS results, define a strong subsiding pattern with substantial horizontal motional component compatible with normal faulting activated structure. In the period followed the mainshock and up to April 30, 2022, the two GNSS sites in Arkalochori and Heraklion city show increased velocity values, compared to the previous period, indicating that the post-seismic relaxation continuous up to this date.

The mainshock was followed by numerous aftershocks, with the largest being an  $M_w 5.3$  event on September 28, 2021. Both the foreshock and the aftershock sequences follow the frequency-magnitude scaling law as derived in the framework of Non-Extensive Statistical Physics (NESP). Applying this model, a greater  $q_m$ -value was estimated for the SW aftershocks cluster, consistent with a lower  $b$ -value, indicating greater tectonic instability in this region where the mainshock and the greatest aftershock occurred. Scaling was also found in the temporal properties of the sequence. The aftershocks production rate, in both the SW and NE clusters, decays according to a composite model of three modified Omori regimes, signifying the generation of secondary aftershock sequences embedded in the aftershock sequence of the  $M_w 6.0$  mainshock. Furthermore, the cumulative distributions of the inter-event times between the successive events for the foreshock and aftershock sequences, as well as for the NE and SW aftershock clusters, scale according to the  $q$ -exponential distribution derived in the framework of NESP, indicating clustering and long-range correlations in the temporal evolution of seismicity.

Summarizing we can state that for the 2021-2022 Arkalochori earthquake sequence the consistency between seismological, geodetic, satellite and geophysical observations has been well demonstrated, highlighting the complementarity of multi-disciplinary approaches.

## References

1. Delibasis, N.; Drakopoulos, J. K.; Fytrolakis, N.; Katsikatos, G.; Makropoulos, K.C.; Zamani A. Seismotectonic Investigation of the area of Crete Island, Proc. of the Intern. Symp. On the Hellenic Arc and Trench (H.E.A.T.), Athens, 1981, 1, 121-138.
2. Drakopoulos, J.; Delibasis, N. "The focal mechanism of earthquakes in the major area of Greece for the period 1947-1981." Seismol. Lab. Univ. Athens Publ, 1982, 2, 1-72.
3. Ganas, A.; Parsons, T. Three-dimensional model of Hellenic Arc deformation and origin of the Cretan uplift. *J. Geophys. Res.* 2009, 114, B06404.
4. Kiratzi, A.; Benetatos, C.; Vallianatos F. Seismic deformation derived from moment tensor summation: application along the Hellenic Trench, (Book Chapter) Springer International Publishing AG, part of Springer Nature 2019, S. D'Amico (ed.), *Moment Tensor Solutions*, 2018, Springer Natural Hazards, [https://doi.org/10.1007/978-3-319-77359-9\\_10](https://doi.org/10.1007/978-3-319-77359-9_10)
5. Papadimitriou, E.; Karakostas, V.; Mesimeri, M.; Vallianatos, F. The  $M_w 6.7$  12 October 2013 western Hellenic Arc main shock and its aftershock sequence: implications for the slab properties. *Int J Earth Sci*, 2016, 105(7), 2149-2160.
6. Ten Veen, J.H.; Meijer, P.T. Late Miocene to recent tectonic evolution of Crete (Greece): Geological observations and model analysis. *Tectonophysics* 1998, 298, 191-208.
7. Papanikolaou, D.; Vassilakis, E. Thrust faults and extensional detachment faults in Cretan tectono-stratigraphy: Implications for Middle Miocene extension. *Tectonophysics* 2010, 488, 233-247.
8. Fassoulas, C. The tectonic development of a Neogene basin at the leading edge of the active European margin: The Heraklion basin, Crete, Greece. *J. Geodyn.* 2001, 31, 49-70.
9. Caputo, R.; Catalano, S.; Monaco, C.; Romagnoli, R.; Tortorici, G.; Tortorici, L. Active faulting on the island of Crete (Greece). *Geophys. J. Int.* 2010, 183, 111-126.
10. Ganas, A.; Parsons, T. Three-dimensional model of Hellenic Arc deformation and origin of the Cretan uplift. *J. Geophys. Res.* 2009, 114, B06404.
11. Ganas, A.; Kourkoulis, P.; Briole, P.; Moshou, A.; Elias, P.; Parcharidis, I. Coseismic Displacements from Moderate-Size Earth-

- quakes Mapped by Sentinel-1 Differential Interferometry: The Case of February 2017 Gulpinar Earthquake Sequence (Biga Peninsula, Turkey). *Remote Sens.* 2018, 10, 1089
12. Mason, J.; Reicherter, K. The palaeoseismological study of capable faults on Crete. In *Minoan Earthquakes—Breaking the Myth through Interdisciplinarity*, 1st ed.; Jusseret, S., Sintubin, M., Eds.; Leuven University Press: Leuven, Belgium, 2017; pp. 191–216.
  13. Vassilakis, E. Study of the Tectonic Structure of the Messara Basin, Central Crete, With the AID of Remote Sensing Techniques and G.I.S. Ph. D. Thesis, National and Kapodistrian University of Athens, Athens, Greece, 2006; p. 564.
  14. Ganas, A.; Elias, P.; Kapetanidis, V.; Valkaniotis, S.; Briole, P.; Kassaras, I.; Argyrakis, P.; Barberopoulou, A.; Moshou, A. The July 20, 2017 M6.6 Kos Earthquake: Seismic and Geodetic Evidence for an Active North-Dipping Normal Fault at the Western End of the Gulf of Gökova (SE Aegean Sea). *Pure Appl. Geophys.* 2019, 176, 4177–4211.
  15. Zygouri, V.; Koukouvelas, I.; Ganas, A. Palaeoseismological analysis of the East Giouchtas fault, Heraklion basin, Crete (preliminary results). *Bull. Geol. Soc. Greece* 2016, 50, 563–571.
  16. Stucchi, M.; Rovida, A.; Gomez Capera, A.A.; Alexandre, P.; Camelbeeck, T.; Demircioglu, M.B.; Gasperini, P.; Kouskouna, V.; Musson, R.M.W.; Radulian, M.; et al. The SHARE European Earthquake Catalogue (SHEEC) 1000–1899. *J. Seismol.* 2013, 17, 523–544.
  17. Papazachos, B.C.; Papazachou, C.B. The Earthquakes of Greece; Ziti: Thessaloniki, Greece, 2003; p. 304.
  18. Guidoboni, E.; Comastri, A. Catalogue of Earthquakes and Tsunamis in the Mediterranean Area from the 11th to the 15th Century; INGV-SGA: Roma, Italy, 2005; p. 1037.
  19. Vallianatos, F.; Michas, G.; Hloupis, G.; Chatzopoulos, G. The Evolution of Preseismic Patterns Related to the Central Crete (Mw6.0) Strong Earthquake on 27 September 2021 Revealed by Multiresolution Wavelets and Natural Time Analysis. *Geosciences* 2022, 12, 33.
  20. ITSAK. Arkalochori Earthquakes, M 6.0 on 27/09/2021 & M 5.3 on 28/09/2021: Preliminary Report—Recordings of the ITSAK Accelerometric Network and Damage on the Natural and Built Environment; ITSAK Research Unit: Thessaloniki, Greece, 2021; p. 44.
  21. Triantafyllou, I.; Karavias, A.; Koukouvelas, I.; Papadopoulos, G.A.; Parcharidis, I. The Crete Isl. (Greece) Mw6.0 Earthquake of 27 September 2021: Expecting the Unexpected. *GeoHazards* 2022, 3, 106–124. <https://doi.org/10.3390/geohazards3010006>
  22. Vassilakis, E.; Kaviris, G.; Kapetanidis, V.; Papageorgiou, E.; Fomelis, M.; Konsolaki, A.; Petrakis, S.; Evangelidis, C.P.; Alexopoulos, J.; Karastathis, V.; Voulgaris, N.; Tselentis, G.-A. The 27 September 2021 Earthquake in Central Crete (Greece)—Detailed Analysis of the Earthquake Sequence and Indications for Contemporary Arc-Parallel Extension to the Hellenic Arc. *Appl. Sci.* 2022, 12, 2815. <https://doi.org/10.3390/app12062815>
  23. Ganas, A.; Hamiel, Y.; Serpetsidaki, A.; Briole, P.; Valkaniotis, S.; Fassoulas, C.; Piatibratova, O.; Kranis, H.; Tsironi, V.; Karamitros, I.; Elias, P.; Vassilakis, E. The Arkalochori Mw = 5.9 Earthquake of 27 September 2021 Inside the Heraklion Basin: A Shallow, Blind Rupture Event Highlighting the Orthogonal Extension of Central Crete. *Geosciences* 2022, 12, 220. <https://doi.org/10.3390/geosciences12060220>
  24. Hellenic Mediterranean University Research Center (former Technological Educational Institute of Crete). Seismological Network of Crete; 10.7914/SN/HC; International Federation of Digital Seismograph Networks: Crete, Greece, 2006.
  25. Behr, Y.; Clinton, J. F.; Cauzzi, C.; Hauksson, E.; Jónsdóttir, K.; Marius, C. G.; Pinar, A.; Salichon, J.; Sokos, E. The Virtual Seismologist in SeisComp3: A New Implementation Strategy for Earthquake Early Warning Algorithms *Seism. Res. Lett.* 87(2A):363–373. doi: 10.1785/0220150235 2016
  26. Lee, W.H.K.; Lahr, J.C. HYP071 (Revised): A Computer Program for Determining Hypocenter, Magnitude, and First Motion Pattern of Local Earthquakes; U.S. Geological Survey Open File Report 75-311; U.S. Geological Survey: Reston, VA, USA, 1975.
  27. Karakonstantis, A. 3-D Simulation of Crust and Upper Mantle Structure in the Broader Hellenic Area through Seismic Tomography. Ph.D. Thesis, Department of Geophysics-Geothermics, Faculty of Geology, University of Athens, Athens, Greece, 2017. (In Greek).
  28. Delibasis, N.D.; Ziazia, M.; Voulgaris, N.; Papadopoulos, T.; Stavrakakis, G.N.; Papanastassiou, D.; Drakatos, G. Microseismic activity and seismotectonics of Heraklion Area (central Crete Island, Greece). *Tectonophysics* 1999, 308, 237–248.
  29. Becker, D.; Meier, T.; Bohnhoff, M.; Harjes, H.P. Seismicity at the convergent plate boundary offshore Crete, Greece, observed by an amphibian network. *J. Seismol.* 2010, 14, 369–392.
  30. Klein, F.W. User's Guide to HYPOINVERSE-2000, a Fortran Program to Solve for Earthquake Locations and Magnitudes, 2002-171; United States Department of The Interior Geological Survey: Menlo Park, CA, USA, 2002; 123.
  31. Ganas, A.; Oikonomou, I.A.; Tsimi, C. NOAfaults: A digital database for active faults in Greece. *Bull. Geol. Soc. Greece* 2017, 47, 518–530.
  32. Waldhauser, F. hypoDD-A Program to Compute Double-Difference Hypocenter Locations, open-file report, 01-113; U.S. Geological Survey: Menlo Park, CA, USA, 2001.
  33. Koulakov, I. LOTOS code for local earthquake tomographic inversion: Benchmarks for testing tomographic algorithms. *Bull. Seismol. Soc. Am.* 2009, 99, 194–214.
  34. Jaxybulatov, K.; Koulakov, I.; Ibs-von Seht, M.; Klinge, K.; Reichert, C.; Dahren, B.; Troll, V.R. Evidence for high fluid/melt content beneath Krakatau volcano (Indonesia) from local earthquake tomography *J. Volcanol. Geotherm. Res.* 2011, 206 (3–4), 96–105.
  35. Toomey, D.R.; Foulger, G.R.. Tomographic inversion of local earthquake data from the Hengill–Grensdalur central volcano complex, Iceland. *J. Geophys. Res.* 1989, 94, 17497–17510
  36. Ganas, A.; Fassoulas, C.; Moschou, A.; Bozionelos, G.; Papanastassiou, G.; Tsimi, C.; Valkaniotis, S. Geological and seismological evidence for NW-SE crustal extension at the southern margin of Heraklion Basin, Crete. *Bull. Geol. Soc. Greece* 2017, 51, 52–75.
  37. Kassaras, I.; Kapetanidis, V.; Ganas, A.; Tzani, A.; Kosma, C.; Karakonstantis, A.; Valkaniotis, S.; Chailas, S.; Kouskouna, V.; Papadimitriou, P. The New Seismotectonic Atlas of Greece (v1.0) and Its Implementation. *Geosciences* 2020, 10, 447. [doi.org/10.3390/geosciences10110447](https://doi.org/10.3390/geosciences10110447)

38. Curlander, J.; McDonough, R. *Synthetic Aperture Radar: Systems and Signal Processing*; John Wiley & Sons.: Hoboken, NJ, USA, 1991; ISBN 978-0-471-85770-9
39. Hooper, A.; Bekaert, D.; Spaans, K.; Arikan, M. Recent advances in SAR interferometry time series analysis for measuring crustal deformation. *Tectonophysics*, 2012, 514–517, 1–1.
40. Massonnet, D.; Rabaut, T. Radar interferometry: limits and potential. *IEEE Geosci Remote Sens*, 1993, 8(2), 455–464. <https://doi.org/10.1109/36.214922>
41. Bamler, R.; Hartl, P. Synthetic Aperture Radar Interferometry. *Inverse Probl.* 1998, 14, 1–54.
42. Elliott, J.; Walters, R.; Wright, T. The role of space-based observation in understanding and responding to active tectonics and earthquakes. *Nat Commun*, 2016, 7, 13844.
43. Markogiannaki, O.; Karavias, A.; Bafi, D. et al. A geospatial intelligence application to support post-disaster inspections based on local exposure information and on co-seismic DInSAR results: the case of the Durrës (Albania) earthquake on November 26, 2019. *Nat Hazards*, 2020, 103, 3085–3100, <https://doi.org/10.1007/s11069-020-04120-7>
44. Sakkas, V. Ground Deformation Modelling of the 2020 Mw6.9 Samos Earthquake (Greece) Based on InSAR and GNSS Data. *Remote Sens*. 2021, 13, 1665. <https://doi.org/10.3390/rs13091665>
45. Goldstein, R.M.; Werner, C.L. Radar interferogram filtering for geophysical applications. *Geophys. Res. Lett.* 1998, 25, 4035–4038. [S data, Remote Sensing, 2021, 13 (9), art. no. 1665.
46. Dach, R.; Lutz, S.; Walser, P.; Fridez, P. *Bernese GNSS Software Version 5.2; User manual*; Astronomical Institute, University of Bern, Bern Open Publishing: Bern, Switzerland, 2015.
47. Briole, P.; Ganas, A.; Elias, P.; Dimitrov, D. The GPS velocity field of the Aegean. New observations, contribution of the earthquakes, crustal blocks model. *Geophys. J. Int.* 2021, 226, 468–492. <https://doi.org/10.1093/gji/ggab089>
48. King, G. C.; Stein, R. S.; Lin, J. Static stress changes and the triggering of earthquakes. *Bulletin of the Seismological Society of America*, 1994, 84(3), 935–953.
49. Alkan, H.; Büyüksaraç, A.; Bektaş, Ö.; Isik, E. Coulomb stress change before and after 24.01.2020 Sivrice (Elazığ) Earthquake (Mw = 6.8) on the East Anatolian Fault Zone. *Arab J Geosci.*, 2021, 14, 2648. <https://doi.org/10.1007/s12517-021-09080-1>
50. Toda, S.; Stein, R.S.; Sevilgen, V.; Lin, J. Coulomb 3.3 Graphic-rich deformation and stress-change software for earthquake, tectonic, and volcano research and teaching—user guide. US Geological Survey open-file report, 2011, 1060, 63.
51. Scholz, C. *The Mechanics of Earthquakes and Faulting*, 3rd ed. Cambridge University Press, Cambridge
52. Cocco, M.; Rice, J. R. Pore pressure and poroelasticity effects in Coulomb stress analysis of earthquake interactions. *Journal of Geophysical Research: Solid Earth*, 2002, 107(B2), ESE-2.
53. Lin, J.; Stein, R. S. Stress triggering in thrust and subduction earthquakes and stress interaction between the southern San Andreas and nearby thrust and strike-slip faults. *Journal of Geophysical Research: Solid Earth*, 2004, 109(B2).
54. Harris, R. A.; Simpson, R. W. Suppression of large earthquakes by stress shadows: A comparison of Coulomb and rate-and-state failure. *Journal of Geophysical Research: Solid Earth*, 1998, 103(B10), 24439–24451.
55. Wells, D.L.; Coppersmith, K.J. New empirical relationships among magnitude, rupture length, rupture width, rupture area, and surface displacement. *Bull. Seismol. Soc. Am.* 1994, 84, 974–1002.
56. Gutenberg, B.; Richter, C. Frequency of earthquakes in California. *Bull. Seismol. Soc. Am.* 1944, 34, 185–188.
57. Frohlich, C.; Davis, S.D. Teleseismic b values; or, much ado about 1.0. *J. Geophys. Res.* 1993, 98, 631–644.
58. Schorlemmer, D.; Wiemer, S.; Wyss, M. Variations in earthquake-size distribution across different stress regimes. *Nature* 2005, 437, 539–542.
59. Mogi, K. Some discussion on aftershocks, foreshocks and earthquake swarms—the fracture of a semi-infinite body caused by an inner stress origin and its relation to the earthquake phenomena (3rd paper). *Bull. Earthq. Res. Inst. Univ. Tokyo* 1963, 41, 615–658
60. Suyehiro, S.; Sekiya, H. Foreshocks and earthquake prediction. *Tectonophysics* 1972, 14, 219–225.
61. Papazachos, B.C. Foreshocks and earthquake prediction. *Tectonophysics* 1975, 28, 213–226.
62. Jones, L.M.; Molnar, P. Some characteristics of foreshocks and their possible relationship to earthquake prediction and premonitory slip on faults. *J. Geophys. Res.* 1979, 84, 3596–3608.
63. Main, I.; Meredith, P.G.; Jones, C. A reinterpretation of the precursory seismic b-value anomaly from fracture mechanics. *Geophys. J. Internat.* 1989, 96, 131–138.
64. Chan, C.-H.; Wu, Y.-M.; Tseng, T.-L.; Lin, T.-L.; Chen, C.-C. Spatial and temporal evolution of b-values before large earthquakes in Taiwan. *Tectonophysics* 2012, 532–535, 215–222.
65. Kato, A.; Obara, K.; Igarashi, T.; Tsuruoka, H.; Nakagawa, S.; Hirata, N. Propagation of slow slip leading up to the 2011 Mw 9.0 Tohoku-Oki earthquake. *Science* 2012, 335, 705–708.
66. Nanjo, K.Z.; Hirata, N.; Obara, K.; Kasahara, K. Decade-scale decrease b value prior to the M9-class 2011 Tohoku and 2004 Sumatra quakes. *Geophys. Res. Lett.* 2012, 39, 1–4.
67. Papadopoulos, G.A.; Minadakis, G. Foreshock Patterns Preceding Great Earthquakes in the Subduction Zone of Chile. *Pure Appl. Geophys.* 2016, 173, 3247–3271.
68. Papadopoulos, G.A.; Minadakis, G.; Orfanogiannaki, K. Short-Term Foreshocks and Earthquake Prediction. In *AGU Geophysical Monograph Series Book*, 1st ed.; Ouzounov, D., Pulinets, S., Hattori, K., Taylor, P., Eds.; John Wiley & Sons, Inc.: Hoboken, NJ, USA, 2018; pp. 127–147.
69. Wiemer S, Wyss M (2000) Minimum magnitude of complete reporting in earthquake catalogs: examples from Alaska, the Western United States, and Japan. *Bulletin Seismology Society of America* 90: 859–869
70. Sotolongo-Costa, O.; Posadas, A. Fragment-asperity interaction model for earthquakes. *Phys. Rev. Lett.* 2004, 92, 048501.
71. Tsallis, C. Possible generalization of Boltzmann–Gibbs statistics. *J. Stat. Phys.* 1988, 52, 479–487.
72. Tsallis, C. *Introduction to Nonextensive Statistical Mechanics: Approaching a Complex World*; Springer: Berlin, Germany, 2009.
73. Silva, R.; França, G.S.; Vilar, C.S.; Alcaniz, J.S. Nonextensive models for earthquakes. *Phys. Rev. E* 2006, 73, 026102.
74. Telesca, L. Tsallis-Based Nonextensive Analysis of the Southern California Seismicity. *Entropy* 2011, 13, 1267–1280. <https://doi.org/10.3390/e13071267>

75. Vallianatos, F.; Papadakis, G.; Michas, G. Generalized statistical mechanics approaches to earthquakes and tectonics. *Proc. of the Royal Society A*, 2016, 472, 2196, doi: 10.1098/rspa.2016.0497
76. Vallianatos, F.; Michas, G.; Hloupis, G. Seismicity Patterns Prior to the Thessaly (Mw6.3) Strong Earthquake on 3 March 2021 in Terms of Multiresolution Wavelets and Natural Time Analysis. *Geosciences* 2021, 11, 379.
77. Vallianatos, F. A non extensive statistical physics approach to the polarity reversals of the geomagnetic field, *Physica A: Statistical Mechanics and its Applications*, 2011, 390 (10), 1773-1778.
78. Vallianatos, F.; Sammonds, P. Is plate tectonics a case of non-extensive thermodynamics? *Physica A: Statistical Mechanics and its Applications*, 2010, 389 (21), 4989-4993.
79. Vallianatos, F.; Telesca, L. Statistical mechanics in earth physics and natural hazards, *Acta Geophysica*, 2012, 60, 3, 499-501.
80. Vallianatos, F.; Michas, G.; Papadakis, G.; Tzanis, A. Evidence of non-extensivity in the seismicity observed during the 2011-2012 unrest at the Santorini volcanic complex, Greece, *Nat. Hazards Earth Syst. Sci.*, 2013, 13,177-185.
81. Vallianatos, F.; Sammonds, P. Evidence of non-extensive statistical physics of the lithospheric instability approaching the 2004 Sumatran-Andaman and 2011 Honshu mega-earthquakes, *Tectonophysics*, 2013, 590, 52-58.
82. Papadakis, G.; Vallianatos, F.; Sammonds, P.; Evidence of Nonextensive Statistical Physics behavior of the Hellenic Subduction Zone seismicity, *Tectonophysics*, 2013, 608, 1037 -1048
83. Papadakis, G.; Vallianatos, F.; Michas, G. The earthquake intervent time distribution along the Hellenic subduction Zone. *Bulletin of the Geological Society of Greece*, 2013, XLVII, 1194-1200.
84. Vallianatos, F.; Karakostas, V.; Papadimitriou, E. A Non-Extensive Statistical Physics View in the Spatiotemporal Properties of the 2003 (Mw6.2) Lefkada, Ionian Island Greece, Aftershock Sequence, *Pure and Applied Geophysics*, 2014, 171, 7, 1343-1534. Doi: 10.1007/s00024-013-0706-6
85. Chochlaki, K.; Vallianatos, F.; Michas, G. Global regionalized seismicity in view of Non-Extensive Statistical Physics. *Physica A: Statistical Mechanics and its Applications*, 2018, 493, 276-285.
86. Vallianatos, F.; Michas, G.; Papadakis, G. Non Extensive statistical Seismology: An overview, in T. Chelidze, L. Telesca and F. Vallianatos, *Complexity of seismic time series; Measurement and Application*, Elsevier, (2018).
87. Omori, F. On after-shocks of earthquakes, *J Coll Sci Imp Univ Tokyo*, 1894, 7, 111-200.
88. Utsu, T. A statistical study on the occurrence of aftershocks. *Geo-physics*, 1961, 30,521–605
89. Utsu, T.; Ogata, Y.; Matura, R.S. The Centenary of the Omori Formula for a Decay Law of Aftershock Activity. *J Phys Earth*, 1995, 43,1-33.
90. Ogata Y (1983) Estimation of the parameters in the modified Omori formula for aftershock frequencies by the maximum likelihood procedure. *J Phys Earth* 31: 115–124
91. Michas, G.; Vallianatos, F. Scaling properties, multifractality and range of correlations in earthquake timeseries: Are earthquakes random? In: *Limnios N, Papadimitriou E, Tsaklidis G (eds) Statistical Methods and Modeling of Seismogenesis*, 2021, ISTE John Wiley, London
92. Abe, S.; Suzuki, N. Scale-free statistics of time interval between successive earthquakes. *Phys. A Stat. Mech. Appl.* 2005, 350, 588–596.
93. Michas, G.; Vallianatos, F.; Sammonds, P. Non-extensivity and long-range correlations in the earthquake activity at the West Corinth rift (Greece). *Nonlinear Processes in Geophysics*, 2013, 20, 713–724
94. Vallianatos, F.; Michas, G.; Benson, P.; Sammonds, P. Natural time analysis of critical phenomena: The case of acoustic emissions in triaxially deformed Etna basalt. *Phys. A Stat. Mech. Appl.* 2013, 392, 5172–5178.
95. Chochlaki, K.; Michas, G.; Vallianatos, F. Complexity of the Yellowstone Park Volcanic Field Seismicity in Terms of Tsallis Entropy. *Entropy* 2018, 20, 721. doi.org/10.3390/e20100721
96. Vallianatos, F.; Michas, G.; Papadakis, G.; Sammonds P. A non-extensive statistical physics view to the spatiotemporal properties of the June 1995, Aigion earthquake (M6.2) aftershock sequence (West Corinth rift, Greece). *Acta Geophys*, 2012, 60, 758–768.
97. Vallianatos, F.; Pavlou, K. Scaling properties of the Mw7.0 Samos (Greece), 2020 aftershock sequence. *Acta Geophysica*, 2021, 1-18. doi.org/10.1007/s11600-021-00579-5
98. G Michas, K Pavlou, S. E Avgerinou, E. A Anyfadi, F Vallianatos, Aftershock patterns of the 2021 Mw 6.3 Northern Thessaly (Greece) earthquake, *Journal of Seismology*, 1-25, 2022
99. Peng, Z., Zhao, P. Migration of early aftershocks following the 2004 Parkfield earthquake. *Nature Geosci* 2, 877–881 (2009). doi.org/10.1038/ngeo697
100. Obana, K.; Kodaira, S.; Nakamura, Y.; Sato, T.; Fujie, G.; Takahashi, T.; Yamamoto. Y. Aftershocks of the December 7, 2012 intraplate doublet near the Japan Trench axis. *Earth Planets Space*, 2014, 66,24. doi.org/10.1186/1880-5981-66-24
101. Tang, C.C.; Lin, C.H.; Peng, Z. Spatial-temporal evolution of early aftershocks following the 2010 ML6.4 Jiashian earthquake in southern Taiwan. *Geophysical Journal International*, 2014, 199,1772– 1783
102. Frank, W.B.; Poli, P.; Perfettini, H. Mapping the rheology of the Central Chile subduction zone with aftershocks. *Geophysical Research Letters*, 2017, 44, 5374–5382 . doi.org/10.1002/2016GL072288
103. Perfettini, H.; Frank, W.B.; Marsan, D.; Bouchon, M. A model of aftershock migration driven by afterslip. *Geophysical Research Letters*, 2018, 45, 2283–2293. doi.org/10.1002/2017GL076287
104. Ariyoshi, K.; Matsuzawa, T.; Hasegawa, A. The key frictional parameters controlling spatial variations in the speed of postseismic-slip propagation on a subduction plate boundary. *Earth Planet Sci Lett*, 2007, 256,136-146. doi:10.1016/j.epsl.2007.01.019
105. Kato, A.; Iidaka, T.; Kurashimo, E.; Nakagawa, S.; Hirata, N.; Iwasaki, T. Delineation of probable asperities on the Atotsugawa fault, central Japan, using a dense temporary seismic network, *Geophys. Res. Lett.*, 2007, 34, L09318. doi:10.1029/2007GL029604.
106. Perfettini H, Avouac JP (2004) Postseismic relaxation driven by brittle creep: A possible mechanism to reconcile geodetic measurements and the decay rate of aftershocks, application to the Chi-Chi earthquake, Taiwan. *Journal of Geophysical Research* 109, B02304
107. Dieterich, J.H. A constitutive law for earthquake production and its application to earthquake clustering. *J Geophys Res*, 1994, 99,

2601–2618.

108. Margaris, B.N.; Hatzidimitriou, P.M. Source spectral scaling and stress release estimates using strong-motion records in Greece. *Bulletin of the Seismological Society of America*, 2002, 92(3), 1040-1059.
109. Allmann, B.P.; Shearer P. M. Global variations of stress drop for moderate to large earthquakes. *J. Geophys. Res.*, 2009, 114, B01310, doi:10.1029/2008JB005821
110. Papadimitriou, P.; Voulgaris, N.; Kassaras, I.; Kaviris, G.; Delibasis, N.; Makropoulos, K. The Mw = 6.0, 7 September 1999 Athens Earthquake. *Nat. Hazards* 2002, 27, 15–33.
111. Kapetanidis, V.; Karakonstantis, A.; Papadimitriou, P.; Pavlou, K.; Spingos, I.; Kaviris, G.; Voulgaris, N. The 19 July 2019 earthquake in Athens, Greece: A delayed major aftershock of the 1999 Mw = 6.0 event, or the activation of a different structure? *J. Geodyn.* 2020, 139, 101766.
112. Ganas, A.; Elias, P.; Kapetanidis, V.; Valkaniotis, S.; Briole, P.; Kassaras, I.; Argyrakis, P.; Barberopoulou, A.; Moshou, A. The July 20, 2017 M6.6 Kos Earthquake: Seismic and Geodetic Evidence for an Active North-Dipping Normal Fault at the Western End of the Gulf of Gökova (SE Aegean Sea). *Pure Appl. Geophys.* 2019, 176, 4177–4211.
113. Triantafyllou, I.; Papadopoulos, G.A.; Lekkas, E. Impact on built and natural environment of the strong earthquakes of April 23, 1933, and July 20, 2017, in the southeast Aegean Sea, eastern Mediterranean. *Nat. Hazards* 2020, 100, 671–695.
114. Papadimitriou, P.; Kapetanidis, V.; Karakonstantis, A.; Spingos, I.; Kassaras, I.; Sakkas, V.; Kouskouna, V.; Karatzetzou, A.; Pavlou, K.; Kaviris, G.; et al. First Results on the Mw=6.9 Samos Earthquake of 30 October 2020. *Bull. Geol. Soc. Greece* 2020, 56, 251–279.
115. Karakostas, V.; Tan, O.; Kostoglou, A.; Papadimitriou, E.; Bonatis, P. Seismotectonic implications of the 2020 Samos, Greece, Mw 7.0 mainshock based on high-resolution aftershock relocation and source slip model. *Acta Geophys.* 2021, 69, 979–996.

The following supporting information provides more information on the methods, additional figures and tables used in the main article.

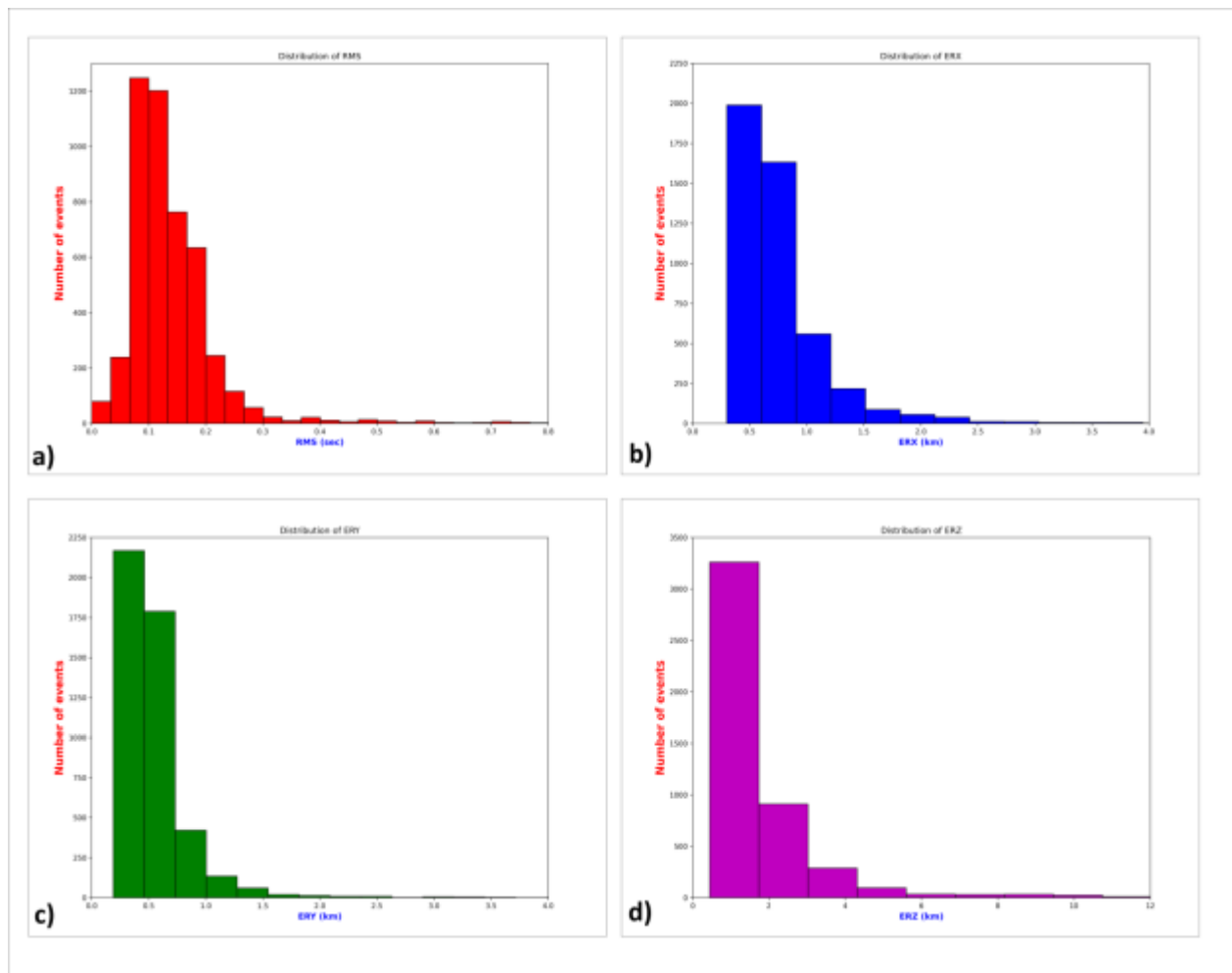


**Figure S1** Statistics of the (a) RMS (b) X-horizontal location error (ERX) (c) Y-horizontal location error (ERY) (d) Z-vertical location error (ERZ).

## Travel-time Tomography-Synthetic tests

P- and S-phases of more than 800 events, recorded during the 2021-2022 time period by local and regional stations of the Hellenic Unified Seismological Network (HUSN) and the Hellenic Strong Motion Network (HSMN), located in Southern Greece, were used for the tomographic inversion. Synthetic tests were performed to set the input parameter values that produced better resolution and increased the fidelity area. Regarding the 3-D tomographic inversion, a dataset consisting of 12,236 P- and 9,820 S-arrival-times was selected, with at least 12 phases per event (Supplementary material, Figure S2). The algorithm provides two alternative options: inversion for  $V_P$  and  $V_S$  ( $V_P$ - $V_S$  scheme) using P and S travel-time residuals ( $dt_P$  and  $dt_S$ ) and inversion for  $V_P$  and  $V_P/V_S$  ratio ( $V_P$ - $V_P/V_S$  scheme) using  $dt_P$  and differential residuals,  $dt_S - dt_P$ . In this study, inversion was performed for both  $V_P$ - $V_S$  and  $V_P$ - $V_P/V_S$  schemes, in order to obtain additional constraints concerning the  $V_P$  and  $V_S$  anomalies (Koulakov 2009; Jaxybulatov et al. 2011).

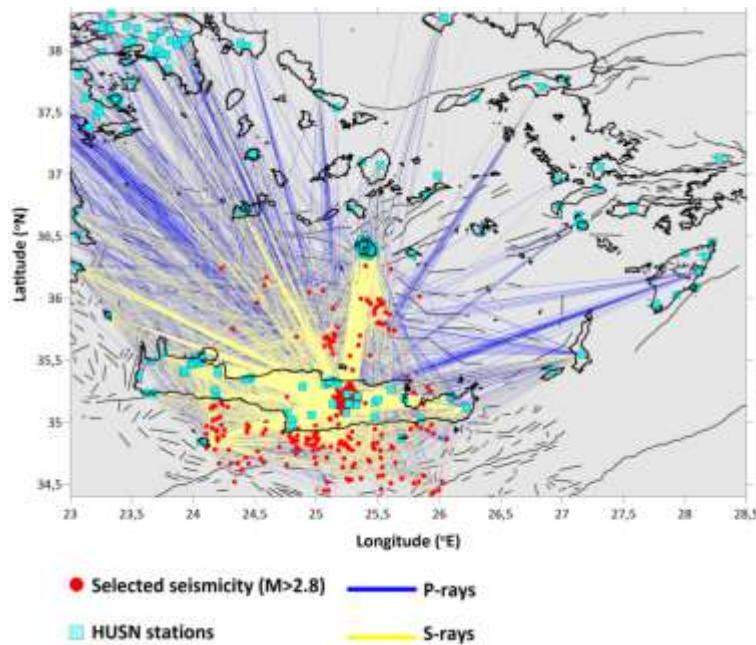


**Figure S2** Total P- (blue) and S-ray (yellow) distribution. Red triangles indicate locations of the HUSN and the HSMN stations. The selected seismicity ( $M \geq 2.8$ ) during the study period (2021-2022) is presented by red circles.

## Sensitivity analysis

In this study, sensitivity analysis for the available dataset was performed by applying the checkerboard test (Humphreys and Clayton 1988). This method uses alternating anomalies of fast and slow velocity perturbations, relative to the initial 1-D gradient model, evenly spaced throughout the model, in a checkerboard pattern (Figures S3-S4). The data resolution is mainly controlled by the ray-path distribution, the model parameterization and smoothing (Lees and Crosson 1989). The average spacing between stations is of the same order as the minimum size of the resolved anomalies in the tomographic inversion (Koulakov and Shapiro 2015).

Checkerboard tests are performed to reproduce the attributes of the real data processing procedure. In the initial synthetic models, the size of cells corresponds to the expected anomalies. The applied procedure requires the definition of spiked regions, with 10% variability in the velocity structure, compared to the reference 1-D velocity model. Travel-times for the paths between the source and the receiver were computed. Subsequently, random noise was added to the synthetic travel-time residuals, to resemble the respective RMS errors of 0.18 s for P-waves and 0.21 s for S-waves which are observed in the real-data. This procedure corresponds to the real observation system,

which uses 3-D ray tracing that follows the bending algorithm principles. The reconstruction of the synthetic model is performed in the same way as with the real data processing, including the 1-D velocity model optimization and the absolute source location. After performing several synthetic tests, the set of parameters that provided a greater confidence area and could successfully reconstruct the model of checkerboard anomalies was used for the 3-D tomographic inversion, using real data. The inversion variance is controlled by errors in the data, including mis-picks, mislocations and incorrectly determined ray-paths.

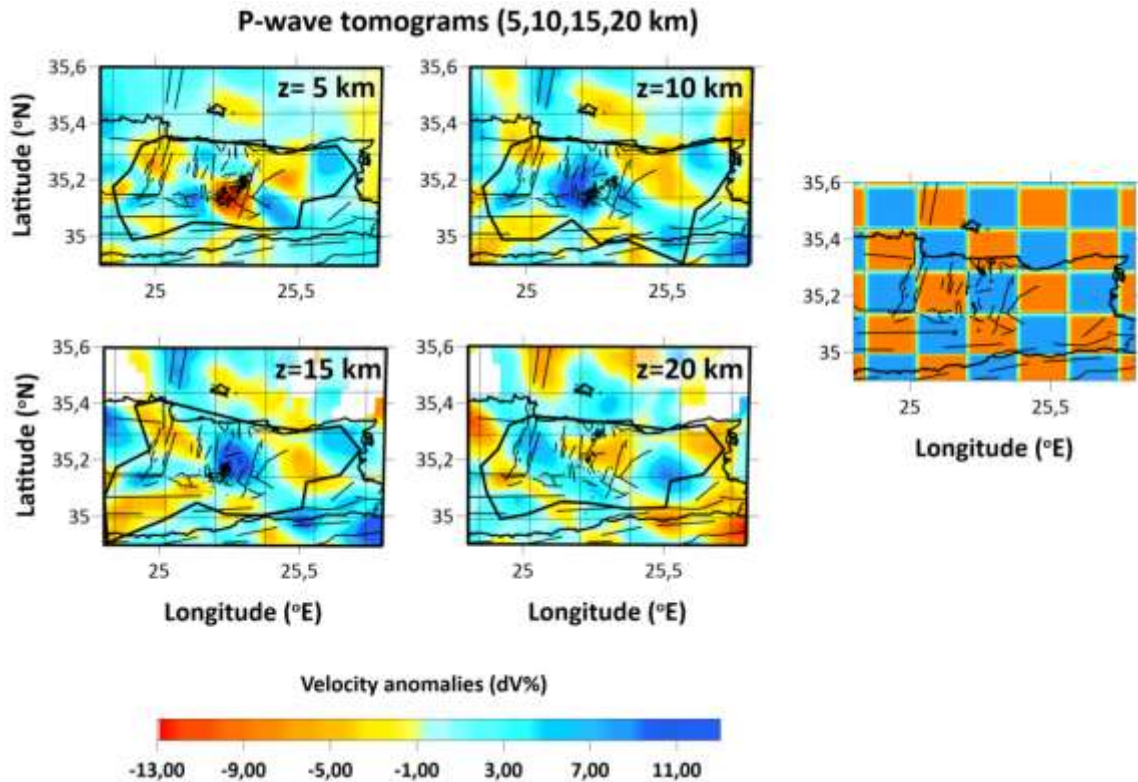


**Figure S3** Reconstruction of P-wave anomalies for the depth slices of 5, 10, 15 and 20 km with anomaly cell size of  $10 \times 10 \text{ km}^2$ . The confidence area is included within the dashed-outline polygon.

An example of a checkerboard test, presented herein, consists of alternating  $10 \times 10 \text{ km}^2$  anomalies for the horizontal tests, which define the limitations of our model. The variations (%) of body-wave velocity anomalies ( $\pm 13\%$ ) are presented in Figures S3-S4, at depths of 5, 10, 15, and 20 km. The sign of the velocity is changed at 5 and 15 km depth, in order to check the vertical resolution. The synthetic model is reconstructed relatively well within the region between Heraklion basin to the north and Asterousia mountains to the south  $35.00^\circ\text{N}$ - $35.25^\circ\text{N}$ ,  $24.90^\circ\text{E}$ - $25.60^\circ\text{E}$ ). More specifically, the anomalies do not resolve well within the depth slices of 10 km and 15 km depth for either of the P- and S-wave velocity models. Horizontal smearing is observed towards the northern and the western part of the study area, mainly due to the azimuthal gap of the available seismological stations and the absence of significant seismic activity recorded during the study period.

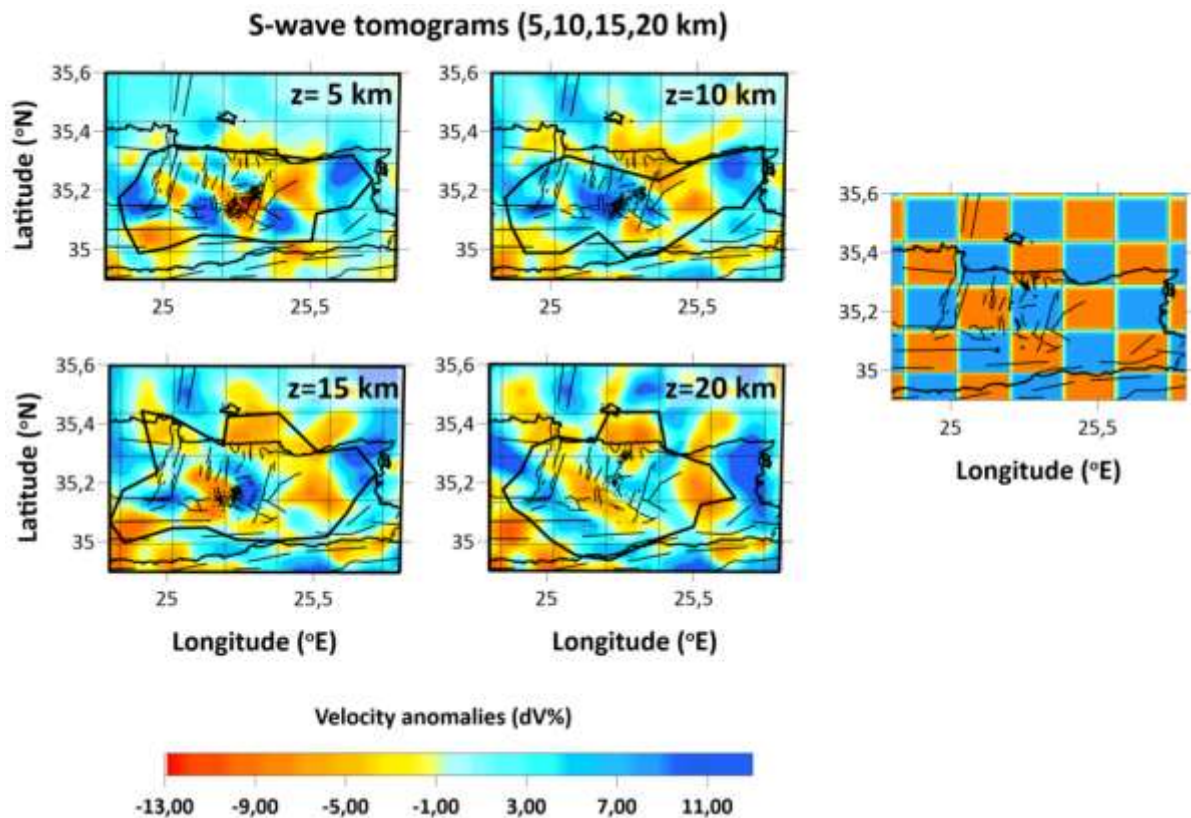


**Figure S4** Reconstruction of S-wave anomalies for the depth slices of 5, 15, 20, and 25 km with anomaly cell size of  $10 \times 10 \text{ km}^2$ . The confidence area is included within the dashed-outline polygon.

Synthetic tests showed that the absolute amplitudes of the body-wave anomalies were up to 5% smaller than the respective ones off or the starting checkerboard grid. These tests are used as a preliminary tool to understand whether the ray configuration enables the reconstruction of the shape of small patterns at all depths. In the case where this condition is not fulfilled, the results of the tests indicate the size of the anomaly preserved throughout the examined depth interval. The size and form of the resolved area for the horizontal slices, in combination with the presence of dense ray coverage for the horizontal slices, provide reliability to the interpretation of the final results of the velocity perturbations.

### GNSS data and results

Time series of the stations coordinates were formed for the four continuous GNSS stations operated on the broad area of central-eastern Crete. The velocity vector was estimated for the period prior to the strong seismic event on September 2021, and for the period followed that event. Sites MOI1 and IERA have shown insignificant or no co-seismic displacement and therefore only one velocity vector is presented for the indicated time period.

**Table S1.** Velocity components for the four continuous GNSS stations on the central-eastern part of Crete.

Site	Latitude(°)	Longitude (°)	Period	V <sub>East</sub> (mm/yr)	V <sub>North</sub> (mm/yr)	V <sub>Up</sub> (mm/yr)
ARKL	35.1339	25.2689	Jan. 30, 2017 - Sept. 26, 2021	$7.20 \pm 0.04$	$-15.02 \pm 0.05$	$-0.88 \pm 0.09$
			4.66yrs			
			Sept. 29, 2021 – Apr. 30, 2022	$4.76 \pm 0.73$	$-19.85 \pm 0.80$	$-26.78 \pm 2.56$
			0.59yrs			
HERA	35.4241	25.1415	Dec. 2, 2013 - Sept. 26, 2021	$7.96 \pm 0.02$	$-13.54 \pm 0.02$	$-0.56 \pm 0.05$
			7.82yrs			
			Sept. 29, 2021 – Apr. 30, 2022	$4.93 \pm 0.65$	$-5.62 \pm 0.62$	$9.81 \pm 1.80$
			0.59 yrs			
MOI1	35.0503	24.8719	May 1, 2020 – Apr. 30 2022	$6.62 \pm 0.11$	$-17.62 \pm 0.14$	$-3.72 \pm 0.40$
			2.00yrs			
IERA	35.0530	25.7970	Jul.5, 2011 – Apr. 30 2022	$9.14 \pm 0.02$	$15.02 \pm 0.03$	$-0.85 \pm 0.05$
			10.83yrs			

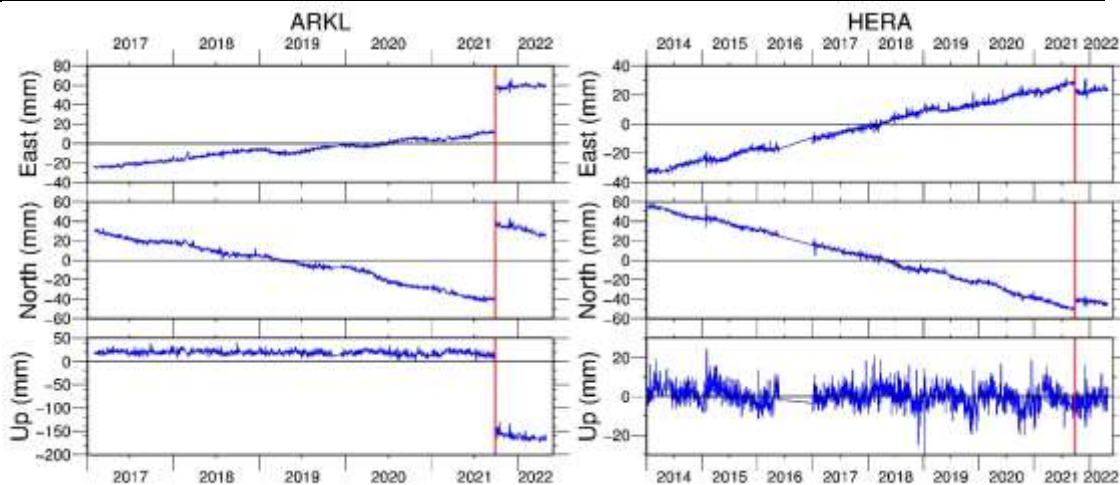


**Figure S5.** Time Series for GNSS sites ARKL and HERA. Red line indicates the strong Mw5.8 seismic event in Arkalochori village.

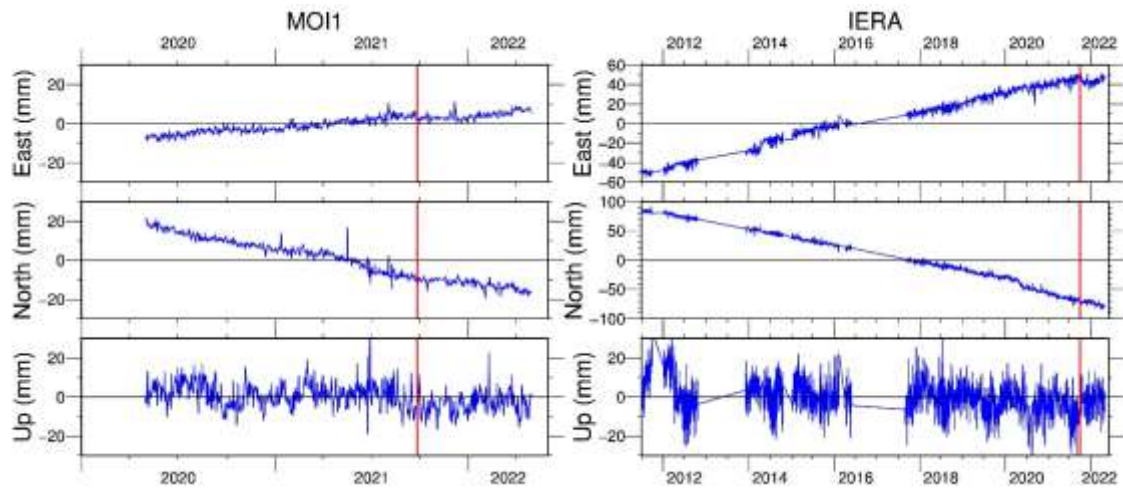


**Figure S6.** Time Series for GNSS sites MOI1 and IERA, located WSW and ESE from epicentral area, respectively. Red line indicates the September 27, 2021 earthquake.



## Chapter 2

The evolution of pre-seismic patterns related to the  
Central Crete (Mw6.0) Strong Earthquake on  
27 September 2021

Revealed by Multiresolution Wavelets  
and Natural Time Analysis

**Abstract:** On 27 September 2021, a shallow earthquake with focal depth of 10 km and moment magnitude  $M_w6.0$  occurred onshore in Central Crete (Greece). The evolution of possible preseismic patterns in the area of Central Crete before the  $M_w6.0$  event, was investigated by applying the methods of multiresolution wavelet analysis (MRWA) along with that of natural time (NT). The monitoring of preseismic patterns by critical parameters defined by NT analysis, integrated with the results of MRWA as the initiation point for the NT analysis, forms a promising framework that may lead to new universal principles that describe the evolution patterns before strong earthquakes. Initially, we apply MRWA to the interevent time series of the successive regional earthquakes in order to investigate the approach of the regional seismicity towards critical stages and to define the starting point of the natural time domain. Then, using the results of MRWA we apply the NT analysis, showing that the regional seismicity approached criticality for a prolonged period of  $\sim 40$  days before the occurrence of the  $M_w6.0$  earthquake, when the  $\kappa_1$  natural time parameter reached the critical value of  $\kappa_1 = 0.070$ , as suggested by the NT method.

## 1. Introduction

On September 27, 2021, a strong  $M_w6.0$  earthquake occurred onshore in Central Crete (Greece), in the close proximity to the city of Heraklion (Figure 1). The mainshock occurred in the vicinity of the Arkalochori town and was widely felt in Crete and the surrounding islands. The earthquake has caused one casualty, several injuries and extensive structural damages to the surrounding villages. The strongest aftershock in the sequence, with local magnitude 5.2, occurred within the first 24 hours, while there were eleven aftershocks with magnitude greater than  $M_L4.0$ .

Crete is located at the front of the Hellenic Island arc (Figure 1) and is an area of important tectonic deformation and high seismic activity, as a result of the collision between the Eurasian and African plates [1, 2]. The Mediterranean seafloor, subducts northwards beneath Crete at a rate of 35 mm/yr that greatly exceeds the convergence between Africa and Eurasia (5-10 mm/yr) due to the rapid SW motion of the southern Aegean itself, relative to Eurasia [1,3]. The dominant horizontal and vertical movements construct a complex fault tectonic structure driven by the presence of both extensional and compressional stresses regimes in the area [4,5]. A study on shallow normal fault earthquakes shows that there are two extensional stress regimes trending NE-SW and NW-SE in the Hellenic Arc [4,6]. In [7], focal mechanisms and GPS velocities, showed that Nubia–Aegean convergence was accommodated by shallowly dipping thrust faulting along the subduction interface, as well as by steeper splay faults in the overriding material.

In the onshore central Crete region, there are two large tectonic features, the northern Heraklion and the southwest Messara tectonic grabens shaped by fault zones with an average NE-SW direction. [1,2,5]. The Heraklion graben is bounded by the Ida Mountain in the west and the Dictea mountain to the east, along the Malevizi and Kastelli fault zones, respectively. The fault zones in central Crete can be divided into four distinguished groups. The first group has faults cutting the basement rocks, or bound basement rocks and Miocene sediments with an E-W direction, while the second one comprises with large and moderated scale faults cutting the previous mentioned formations with a N-S angles. The third and fourth groups are focused on faults with a NE-SW and NW-SE strike, respectively, which appear to be the youngest faults occurring on Crete Island [2,5,8,9]. Recent results suggest that the fault length distribution in the area of Central Crete presents a hierarchical pattern that follows a  $q$ -exponential distribution following the principles of non-extensive statistical physics [10].

The September 27, 2021  $M_w6.0$  ruptured zone, has NNE-SSW direction [11]. In the activated zone, the dominant features are NNE-SSW normal faults like the well-known Kastelli Fault [12] with code GRCS743 in the Greek Database of Seismogenic Sources [13] (<http://gredass.unife.it/> accessed on October 1st, 2021). The moment tensor solutions for the main event obtained from several reporting agencies (see <https://www.seismicportal.eu/mtws/> accessed on October 1st, 2021), suggest that the activated fault was a normal fault with a NW median dip-direction of about  $54^\circ$ , in agreement with [11-13]. The neotectonic Kastelli fault bounds to the northwest the Dikti massif

that consists of carbonate sediments and metamorphic terranes [9]. It is characterized by a 300-m-high major escarpment. Following [9] its strike progressively varies southwestwards from N80°E to N25°E, while dips 70°–75° northwestwards with well-exposed dip-slip slicken lines with pitches of 85°–115°, shows a 13 km long recent reactivation at the base of the mountain front, which corresponds to a maximum possible earthquake magnitude of M6.7 (see details in table 1 of [9]). The maximum measured throw value affecting the Upper Pleistocene slope deposits is about 6 m. In the hanging wall, alluvial–colluvial deposits composed of unconsolidated conglomerates are present.

Strong arguments suggest that the earthquake generation process can be considered as a critical point phenomenon that culminates with a large event, which is the critical point [14–24]. New findings regarding the complex dynamics that characterize various geodynamic phenomena illustrate stimulating features in the framework of new concepts, as that of non-extensive statistical physics [17–24], multiresolution wavelets analysis [25–27] and of the novel time domain, termed as natural time [22–23,28–39].

The concept of natural time (NT) has been introduced recently to analyze possible pre-seismic signals [28,29,34]. The analysis of various complex systems in the NT domain enables the optimal extraction of signal information by reducing the uncertainties related to the conventional time, as well as the identification of long-range correlations in the evolution of the system, even in the presence of “heavy tails” [29]. The usefulness of NT analysis has been discussed in a number of applications to known critical phenomena, such as fracturing, earthquakes, the 2-D Ising model and 3-D turbulent flow [35], and references therein, and it has been tested experimentally in fracturing experiments in the laboratory by analyzing acoustic emissions time series [22,40].

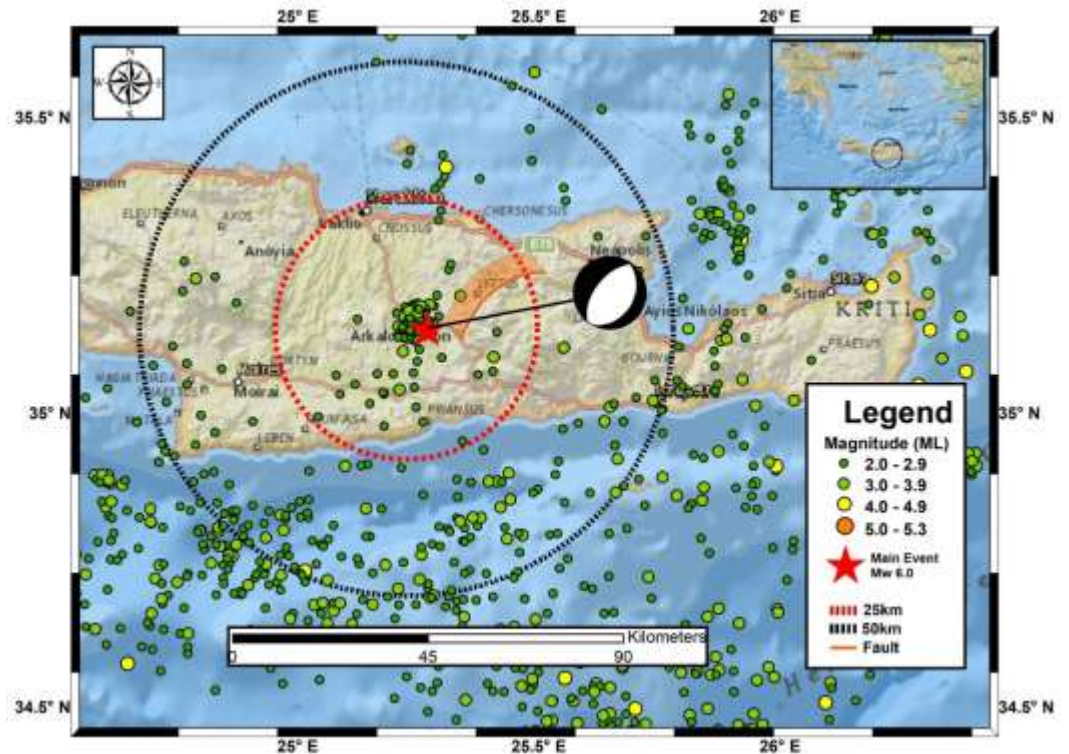


**Figure 1.** The observed seismicity in the Central Crete region between September 15, 2017, and September 27, 2021. The mainshock is denoted with a red star, while earthquakes with threshold magnitude  $M_{th}=2.0$  are represented with circles in different color and size. The two circles with radius 25 and 50 km are noted with red and black dashed lines, respectively. The focal mechanism of the mainshock as estimated by GFZ is presented (see text for details).

Furthermore, wavelet-based methods have been introduced to characterize fractal signals [41–43] and to overcome effects associated with non-stationarities [44,45], a very frequent effect in the time dynamics of an earthquake sequence.

The occurrence of a strong earthquake onshore in Central Crete is rare in recent and historical earthquake catalogs and this makes its study attractive. We note, that according to [9] the mean recurrence interval of Kastelli fault, for the last 13 ka is estimated to about 812 years. The goal of the present work is to test and evaluate the seismicity patterns in terms of MRWA and NT analyses, as applied in the evolution of seismicity prior to the recent  $M_w=6.0$  Central Crete strong event, recognizing the critical stages in earthquake preparation processes. More specifically, the initial application of MRWA in a broader time period reveals time segments where the NT analysis is then used to investigate for indicators suggesting the entrance to the critical stage prior to the  $M_w=6.0$  Central Crete earthquake, integrated with the results of MRWA applied to the interevent time series of the successive events, in order to define, with an objective technique, the starting point for the analysis in the NT domain. The description of seismicity evolution with the NT parameters, integrated with the results of MRWA, represents a novel framework that may lead to a better understanding of the evolution of earthquake generation processes and to the recognition of the period where an activated fault zone is in the critical state.

## 2. Principles of Methodology Applied and Data Selection and Analysis.

### 2.1 Data Selection

The upgrading of the regional seismological networks [46-51] provides a complete spatial coverage in the broader area of Greece and an accurate catalogue of microseismicity, with a magnitude of completeness ( $M_c$ ) down to 2.0, in the studied area (see Fig. 3 in [51]), enabling the application of such methodologies. The earthquake catalogs used herein are from the revised solutions announced by the Hellenic Unified Seismological Network (<http://www.gein.noa.gr/en/networks/husn>, last accessed on October 1<sup>st</sup>, 2021). [49]. Figure 1 presents the seismic activity observed in the region of Central Crete for a period starting from 15 September 2017 approximately 1473 days before the September 27, 2021, mainshock. In the present work MRWA and MT methods applied using the seismicity catalogues that record the events located within circled with the epicenter as a center and radius of 25 and 50 km and magnitude thresholds of 2.0, 2.5 and 3.0, respectively. In Figure 2, the time–magnitude plot for a radius of 25 and 50 km around the epicenter and magnitude thresholds,  $M_{th} = 2.0$ ,  $M_{th} = 2.5$  and  $M_{th} = 3.0$  are presented. From the aforementioned catalogue six subcatalogues (SCx) according to selected magnitude threshold and epicentral radius were produced and presented in Table 1.

**Table 1.** Characteristics of time-magnitude subcatalogues that generated from seismic event catalogue covering the period from 15/9/2017 to 27/9/2021

Subcatalogue	Epicentral radius (km)	Magnitude threshold
SC1	25	2.0
SC2	50	2.0
SC3	25	2.5
SC4	50	2.5
SC5	25	3.0
SC6	50	3.0

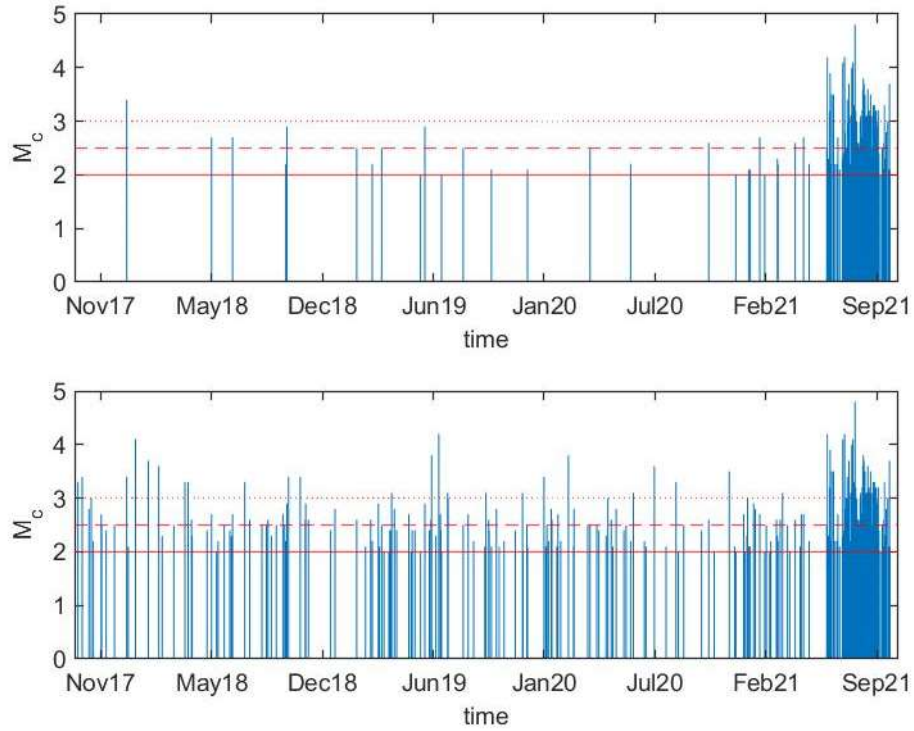


**Figure 2.** Time–Magnitude plot (from 15/9/2017 to 27/9/2021) for a radius of space 25km (top) and 50 km (bottom) around the epicenter. Horizontal lines delineate the three magnitude thresholds ( $M_{th}$ ) that used for the production of corresponding datasets:  $M_{th} = 2.0$  (red solid line),  $M_{th} = 2.5$  (red dashed line),  $M_{th} = 3.0$  (red dotted line).

## 2.2 Multiresolution Wavelets Analysis to the Seismicity of Central Crete

The temporal evolution of seismicity and the time-scaling properties are of crucial importance [53–55] for understanding the correlation properties of seismicity [56]. The analysis of time intervals between successive seismic events can be grouped in exponential or power laws revealing similar behaviors over different scales [57]. A detailed presentation is given in [27, 58]

Following [27, 58] the discrete wavelet transform (DWT) applied to transforms a data vector of length  $M$  into a different vector of the same length. For a point process such as that of the interevent times sequence, the wavelet coefficients can be derived from

$$W_{m,n}^{wav} = 2^{-m/2} \sum_{i=1}^L t_i \psi(2^{-m}i - n) \quad (1)$$

where the scale variable  $m$  and the translation variable  $n$  are integers,  $L$  represents the total number of interevent times  $t_i$  analyzed and  $\psi$  is the wavelet function. We note that already pointed out in [27, 58], smaller scales correspond to more rapid variations and, therefore, to higher frequencies.

Furthermore, as demonstrated in [27, 58] the standard deviation of wavelet coefficients as a function of scale, as described from

$$\sigma_{wav}(m) = \sqrt{\frac{1}{N-1} \sum_{n=1}^N (W_{m,n}^{wav} - \langle W_{m,n}^{wav} \rangle)^2} \quad (2)$$

analysed, where  $N$  is the number of wavelet coefficients at a given scale  $m$  and the brackets indicate the average among the coefficients at a scale  $m$ .

For each one of the SCs presented in Table 1 we produce a corresponding dataset with interevent times between two successive events versus the occurrence time of the second event until the major seismic event. The number of produced datasets is 6 and the time period that was covered for MRWA of interevent times spanned from 15 September 2017 until September 27, 2021, when the main event of  $M_w 6.0$  occurred. The produced point-process

datasets presented in Figure 3 (datasets from SC1, SC2), Figure 4 (datasets from SC3, SC4) and Figure 5 (datasets from SC5, SC6)

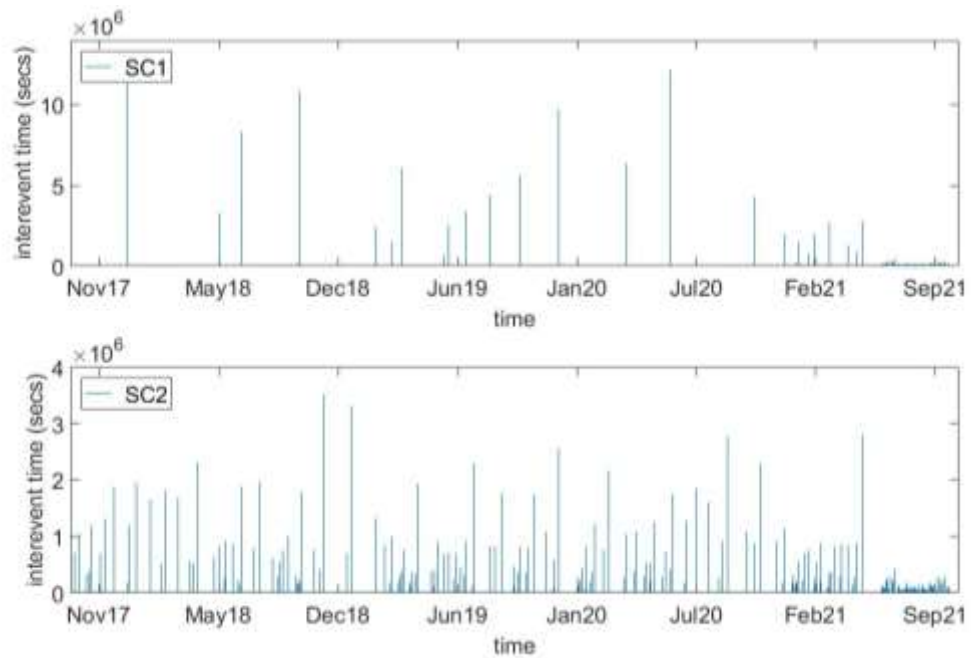


**Figure 3.** Dataset with interevent times between two successive events versus occurrence time of each event for SC1 (top) and SC2 (bottom) subcatalogues (as they defined in Table1). Low amplitude interevent times before September 2021 dictate increased seismic activity

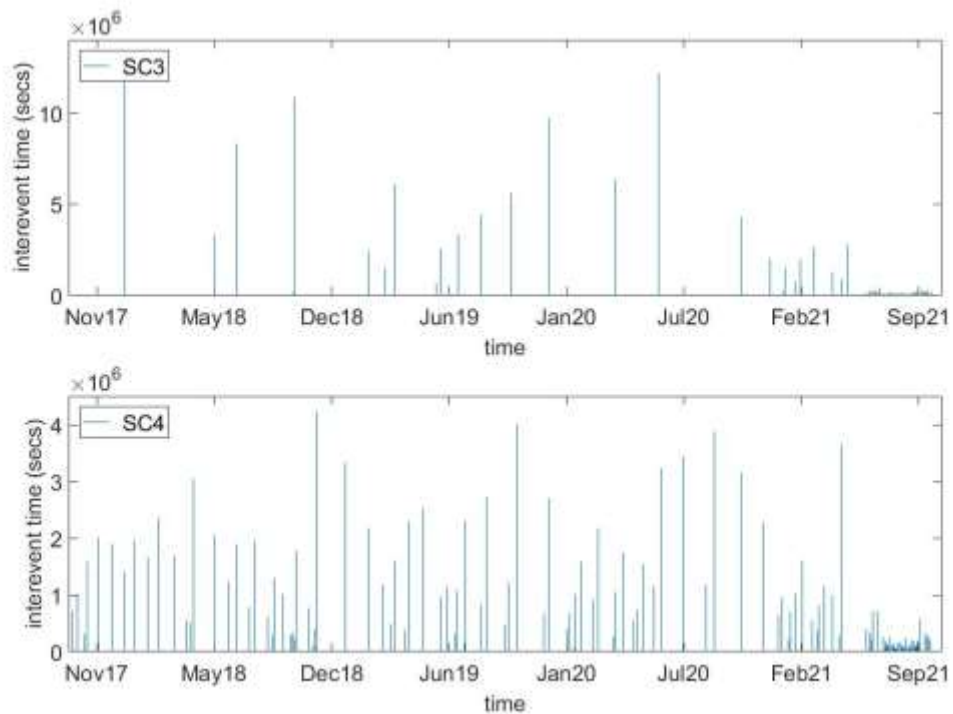


**Figure 4.** Dataset with interevent times between two successive events versus occurrence time of each event for SC3 (top) and SC4 (bottom) subcatalogues (as they defined in Table1). Low amplitude interevent times before September 2021 dictate increased seismic activity

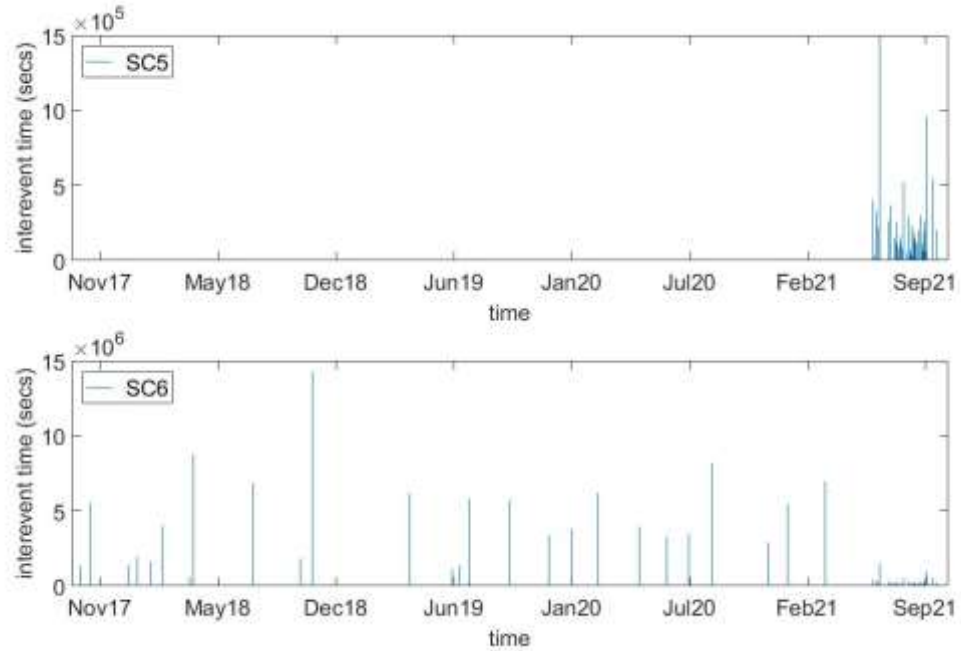


**Figure 5.** Dataset with interevent times between two successive events versus occurrence time of each event for SC3 (top) and SC4 (bottom) subcatalogues (as they defined in Table1). For better depiction of the whole time-series we are starting from 2<sup>nd</sup> event of the catalogue since the 1<sup>st</sup> interevent time between 1<sup>st</sup> and 2<sup>nd</sup> event produce two orders of magnitude higher value and thus suppresses the presentation of the last event of the catalogue where smaller values exist

The initial challenge in wavelet analysis is the selection of the wavelet basis function as well as the decomposition level of signal. Since there is no standard procedure for basis selection, several approaches have been proposed: from general quantitative approaches (maximum cross correlation, distribution error, maximum information criterion extraction, maximizing Shannon entropy, variance correlation, energy preservation [59]) to dedicated ones [60]. All these proposals they just re-validate that wavelet basis selection remains mainly an ad-hoc problem. In the current study the choice of wavelet basis is dictated by the requirement to identify a rather sharp change in a possible cyclic sequence. As a general rule if we want to identify closely spaced features wavelets with smaller support are more appropriate. The support of the wavelet should be small enough to separate the features of interest since wavelet bases with larger support tend to fail to identify closely spaced features. Following the same pre-processing approach as in [26,27,58], we tested several small support wavelets (i.e *haar*, *db2*, *db3*, *sym2*, *sym3*, *coif2*) at small scales up to  $m = 4$  and received quite similar results. Thus, in the current work, we present results from the analysis using the *db3* wavelet.

Here, the time evolution of the  $\sigma_{wav}(m)$ , using fixed event number windows of 16 events shifting through the entire series is investigated, where the shift between successive windows was fixed in 4 events (3 in the case  $M_{th} = 3.0$  and  $R=25\text{km}$  due to limited number of events). Consistently with the length of the time window, we analysed the time variation of the  $\sigma_{wav}(m)$  for lower scales ( $m = 1$  to 4) since the number of available events is limited. Each calculated value is associated with the time of the last event in the window. Figure 8 shows a representative set of results for the time evolution of the  $\sigma_{wav}(m)$  using the *db3* wavelet with four scales for MRWA, for the seismicity observed around the epicenter of the mainshock and within a radius of 25 km and 50 km, respectively.

An initial comment from Figure 6 is the significant temporal variability in the strength of the multiscale properties of the interevent times. As observed in previous studies [26, 27, 58], before the major event of the seismic sequence a significant decrease in the temporal evolution of the  $\sigma_{wav}, m(t)$  appeared, especially at lower scales. Plots at Figure 8 dictate the search for a time marker beginning several weeks before the major event for all the scales analyzed. The sharp decrease, which is observed before the major event, can be qualified as such a time marker since the decrease is evident for several days and is clearly identifiable. From the Figure 6 which corresponds to  $M_{th} = 2.0$ , the candidate time marker is 24-Jul-2021 while for  $M_{th} = 2.5$  (Figure 7) and  $M_{th} = 3.0$  (Figure 8) the same time marker is the dominating one.

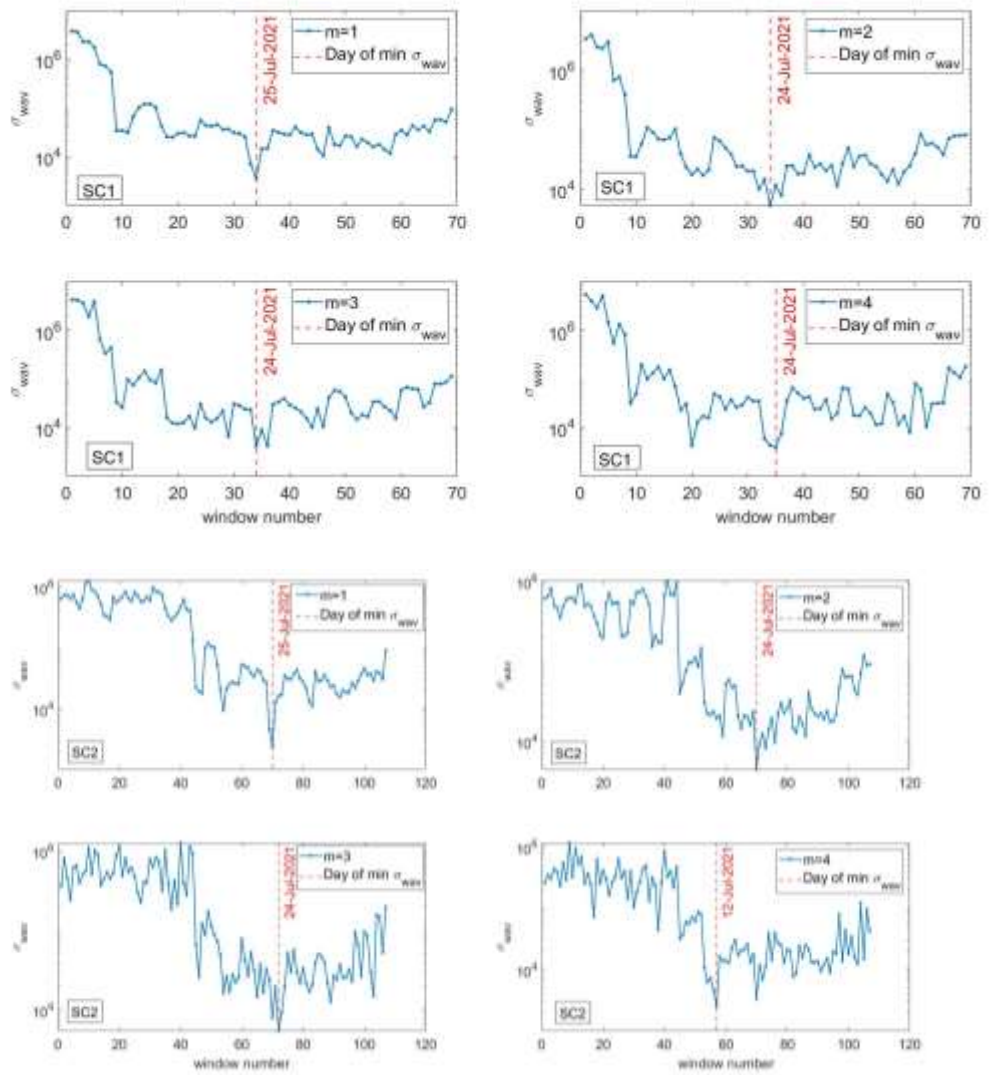


**Figure 6.** Time variation of  $\sigma_{wav}(m)$  with scale  $m$  ranging from 1 up to 4, for moving windows with length of 16 events and a shift of 4 events within a magnitude threshold,  $M_{th} = 2.0$  and radius  $R = 25$  km (interevent times from SC1 subcatalogue – top four plots) and 50 km (interevent times from SC2 subcatalogue - bottom four plots) around the epicenter. Red vertical line indicates the day of minimum in variance, observed at each scale.

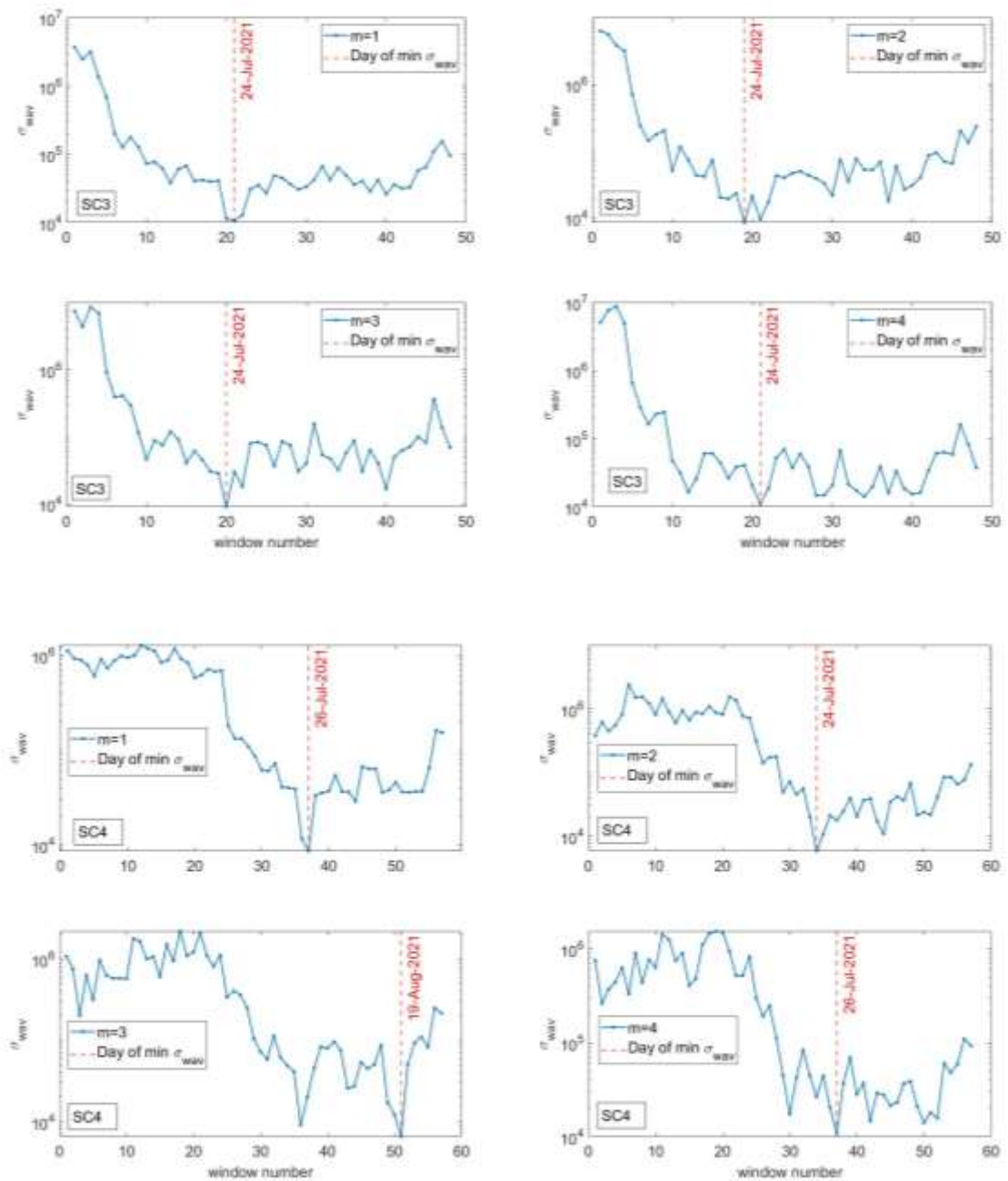


**Figure 7.** Time variation of  $\sigma_{wav}(m)$  with scale  $m$  ranging from 1 up to 4, for moving windows with length of 16 events and a shift of 4 events within a magnitude threshold,  $M_{th} = 2.5$  and radius  $R = 25$  km (interevent times from SC3 subcatalogue – top four plots) and 50 km (interevent times from SC4 subcatalogue - bottom four plots) around the epicenter. Red vertical line indicates the day of minimum in variance, observed at each scale.

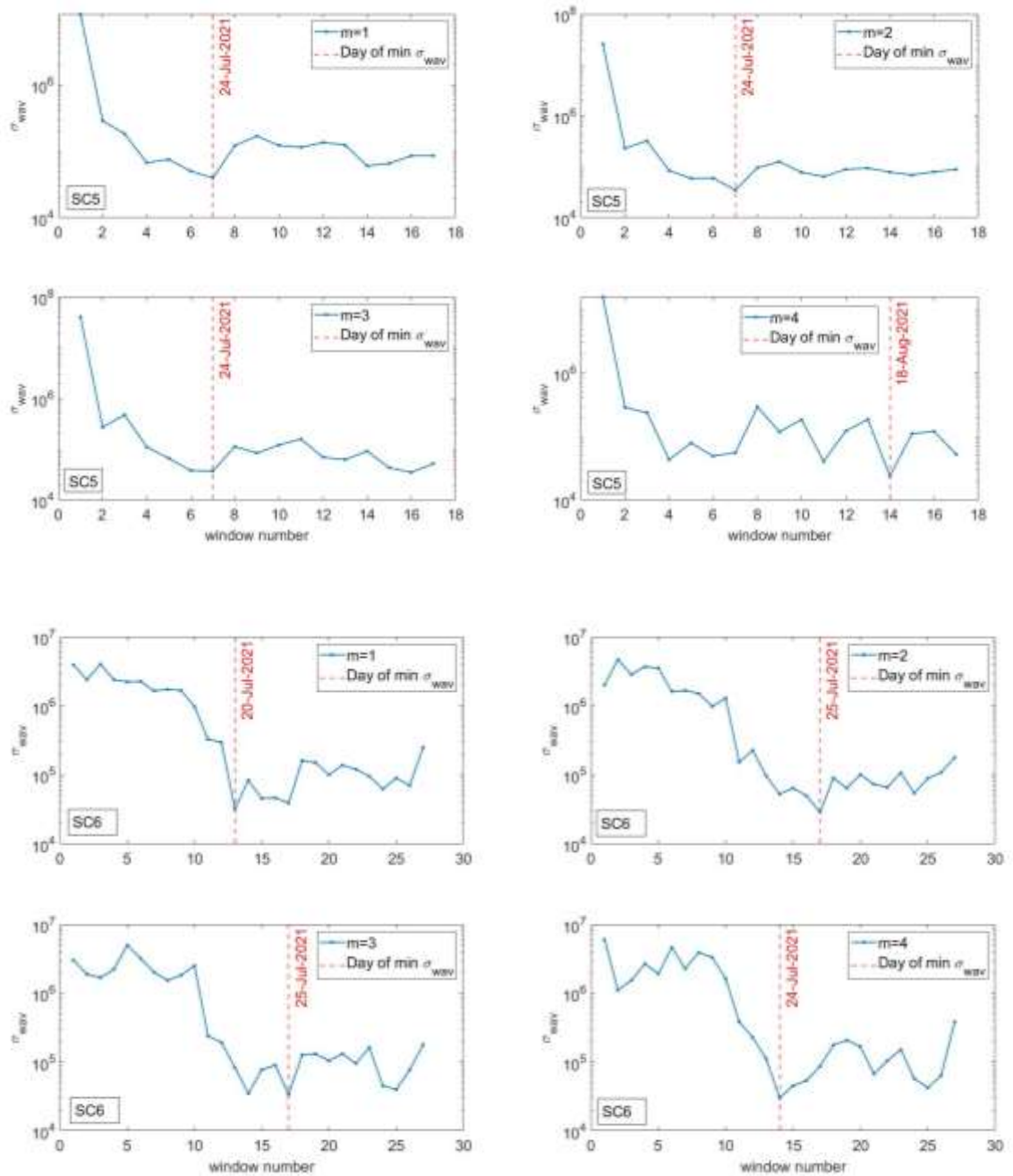


**Figure 8.** Time variation of  $\sigma_{wav}(m)$  with scale  $m$  ranging from 1 up to 4, for moving windows with length of 16 events and a shift of 3 events within a magnitude threshold,  $M_{th} = 3.0$  and radius  $R = 25$  km (interevent times from SC5 subcatalogue – top four plots) and 50 km (interevent times from SC6 subcatalogue - bottom four plots) around the epicenter. Red vertical line indicates the day of minimum in variance, observed at each scale.

Translating the result from lower scales in an alternative way, we propose the use of the observed time marker of 24-Jul-2021, which appear several weeks before the major event, as the initiation point for the natural time analysis that follows. This lead time is consistent with the fact that in natural time analysis of the magnitude time series clear changes in the temporal correlations are observed few months before major earthquakes in California and Japan by means of detrended fluctuation analysis [59-61].

### 2.3. Natural Time Analysis of Seismicity before the Central Crete Mw6.0 Earthquake

Here we summarize the principles of Natural time Analysis, as applied in the case of central Crete Mw6.0 pre-seismic pattern. The analysis of a complex system in the NT domain has been introduced in [28,34]. In the case of seismicity, the natural time  $\chi$ , defined as  $\chi_k = k/N$ , serves as an index for the occurrence of the  $k^{\text{th}}$  event out of  $N$  total events. The seismic moment released during the  $k^{\text{th}}$  event is then considered, forming the pair  $(\chi_k, M_k)$  for further analysis (see [30]). The evolution of  $(\chi_k, M_k)$  is further described by the continuous function  $F(\omega)$ , defined as:  $F(\omega) = \sum_{k=1}^N M_k \exp\left(i\omega \frac{k}{N}\right)$  (3) where  $\omega = 2\pi\phi$  and  $\phi$  stands for the natural frequency.

$F(\omega)$  is normalized by division with  $F(0)$

$$\Phi(\omega) = \frac{\sum_{k=1}^N M_k \exp\left(i\omega \frac{k}{N}\right)}{\sum_{n=1}^N M_n} = \sum_{k=1}^N p_k \exp\left(i\omega \frac{k}{N}\right) \quad (1)$$

where  $p_k = M_k / \sum_{n=1}^N M_n$ . The quantity  $p_k$  describes the probability to observe an earthquake event at natural time  $\chi_k$ . The normalized power spectrum can then be obtained from (4), as  $\Pi(\omega) = |\Phi(\omega)|^2$ . In the context of probability theory, and for natural frequencies of  $\phi$  less than 0.5,  $\Pi(\omega)$  reduces to a characteristic function for the probability distribution  $p_k$ . It has been shown that the following relation holds [22, 27, 30-38, 62, 63]

$$\Pi(\omega) = \frac{18}{5\omega^2} - \frac{6 \cos \omega}{5\omega^2} - \frac{12 \sin \omega}{5\omega^3} \quad (2)$$

As presented in [28, 34] for  $\omega \rightarrow 0$ , (4) leads to

$$\Pi(\omega) \approx 1 - \kappa_1 \omega^2 \quad (3)$$

where  $\kappa_1$  is the variance in natural time, given as

$$\kappa_1 = \langle \chi^2 \rangle - \langle \chi \rangle^2 = \sum_{k=1}^N p_k \chi_k^2 - \left( \sum_{k=1}^N p_k \chi_k \right)^2 \quad (4)$$

It has been shown that the properties of  $\Pi(\omega)$  at  $\omega \rightarrow 0$ , i.e., the values of  $\kappa_1 = 0.07$ , can signify the approach of a complex system towards some critical point [34], such as that of an impending large earthquake (see [31,37] and references therein). Theoretically, it has been shown that  $\kappa_1$  approaches 0.070 as  $N \rightarrow \infty$ , when there are no long-ranged correlations in the system [34].

As a new event occurs, the pair  $(\chi_k, p_k)$  is rescaled and  $\kappa_1$  varies. It has been verified that when the parameter  $\kappa_1$  converges to the value 0.070, the system enters a critical state [34, 35].

Furthermore, the entropy in the NT domain,  $S_{nt}$ , is defined as [34]

$$S_{nt} = \langle \chi \ln \chi \rangle - \langle \chi \rangle \ln \langle \chi \rangle = \sum_{k=1}^N p_k \chi_k \ln \chi_k - \left( \sum_{k=1}^N p_k \chi_k \right) \ln \left( \sum_{k=1}^N p_k \chi_k \right)$$

where  $\langle f(\chi) \rangle = \sum_{k=1}^N p_k f(\chi_k)$ .

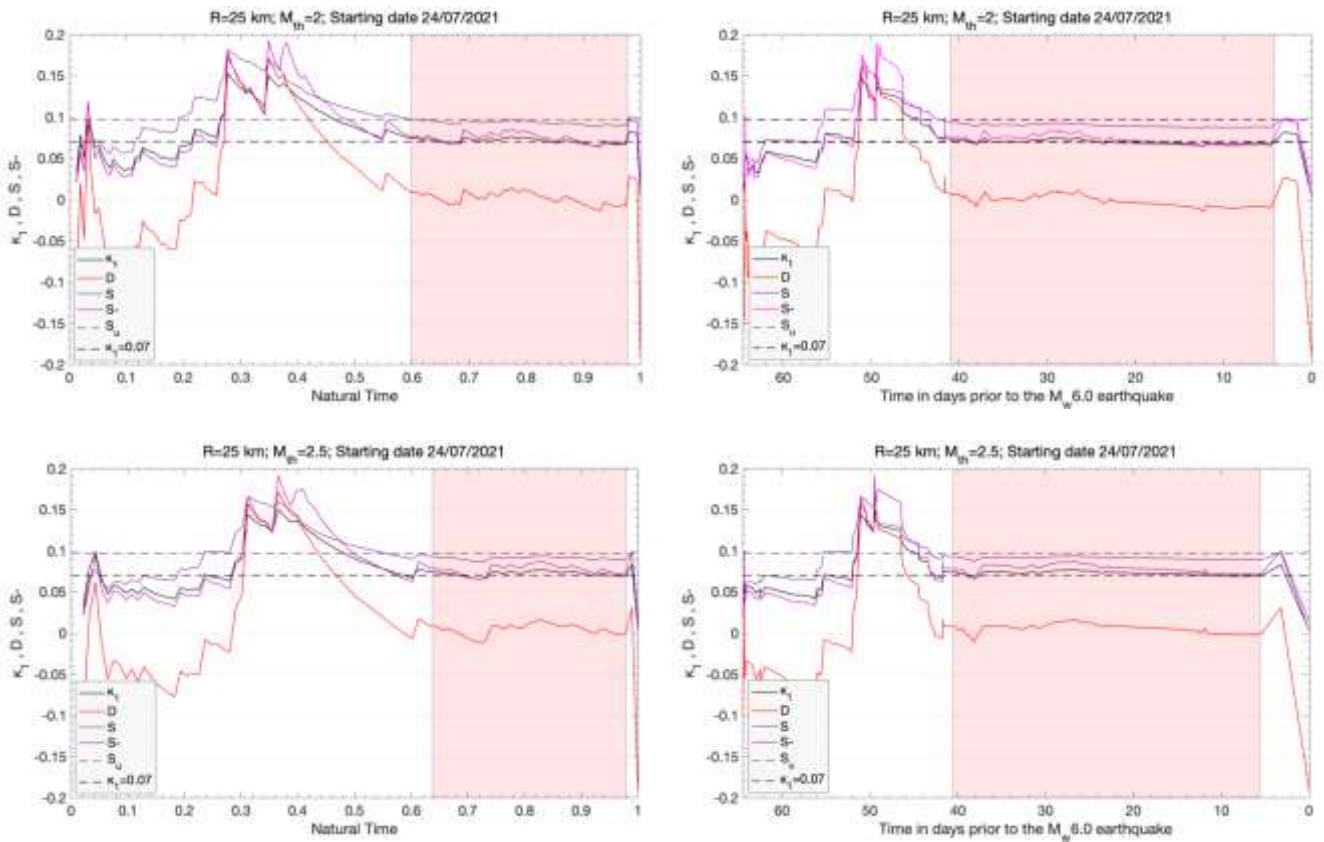
The entropy,  $S_{nt}$ , is a dynamic quantity that depends on the sequential order of events. Moreover, upon the time reversal  $T$ , i.e.,  $Tp_m = p_{N-m+1}$ , the entropy,  $S_{nt-}$ , is further defined. When the analysed seismicity approaches a “true” critical state, the following conditions should be fulfilled [27, 34, 63]:

- (i). The “average” distance  $D$ , defined by the normalized power spectra  $\Pi(\omega)$  of the evolving seismicity and by the theoretical estimation of  $\Pi(\omega)$  for  $\kappa_1 = 0.070$ , should be less than  $10^{-2}$ .
- (ii). The parameter  $\kappa_1$  should approach the critical value of  $\kappa_1 = 0.070$  by “descending from above”.
- (iii). Both natural time entropies,  $S_{nt}$  and  $S_{nt-}$ , should be lower than the entropy of uniform noise  $S_u = (\ln 2/2) - 1/4$  when  $\kappa_1$  approaches 0.070.
- (iv). Since the dynamic evolution of the system is expected to be self-similar in the critical state, the time of the true coincidence should not vary upon changing

(within reasonable limits) either the magnitude threshold,  $M_{th}$ , or the area used in the calculation.

In [27, 58], proposed the use of the time marker indicated by MRWA in the seismicity evolution before the major event as the initiation point for the NT analysis. In the frame of this approach, the two independent methods (MRWA and NT analysis) were integrated to identify the approach to the critical stage in the earthquake preparation process. In particular, the initial application of MRWA in a broader time period of the regional seismicity before the major event reveals time segments where the NT analysis is going to investigate for indicators suggesting the entrance to the critical stage.

In Figure 9, the computed parameters  $D$ ,  $\kappa_1$ ,  $S_{nt}$  and  $S_{nt-}$ , as evolved event by event, are plotted in the natural time and conventional time domains as they approach the critical stage in the regional seismicity of Central Crete, for threshold magnitudes of  $M_{th} = 2.0, 2.5$  and  $3.0$  and for areas of radius  $R = 25$  km and  $R = 50$  km, respectively, around the epicenter of the  $M_w 6.0$  main event. This analysis clearly demonstrates that, from about August 17, 2021 (i.e., about 41 days before the  $M_w 6.0$  earthquake of September 27, 2021), the estimated parameters suggest that a critical stage has been approached. In all cases, for  $M_{th} = 2.0, 2.5$  and  $3.0$ , and  $R = 25$  km and  $R = 50$  km, the NT analysis starts at approximately two months before the main event, i.e. at 24 July, 2021, around the corresponding time marker indicated by MRWA (see Figures 8-10). It may, thus, be considered that the critical point for the regional seismicity was approached around that time. In Figure 9, we observe that all the requirements (i-iv) are fulfilled a few days before the mainshock for all the cases that we study. The results, thus, indicate that the regional seismicity presented criticality characteristics before the main event.



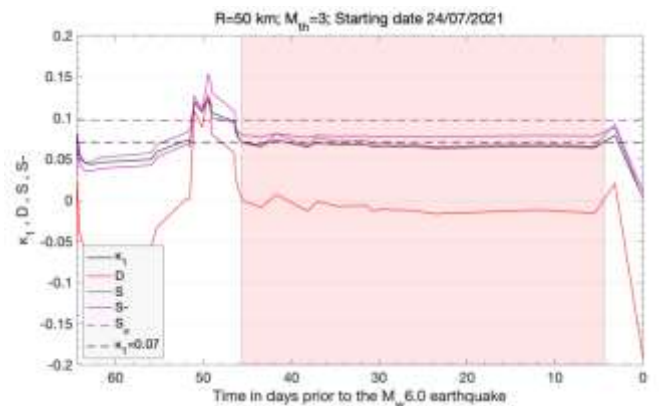
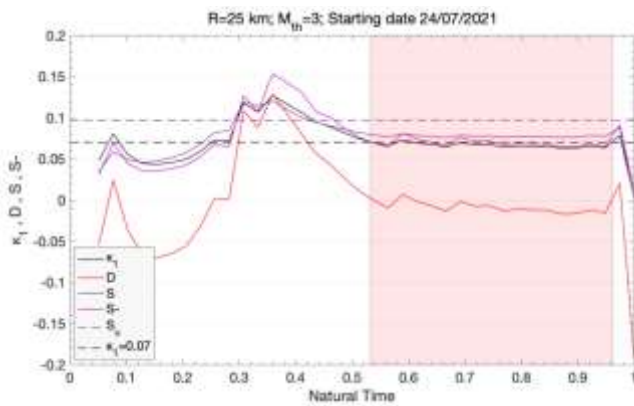
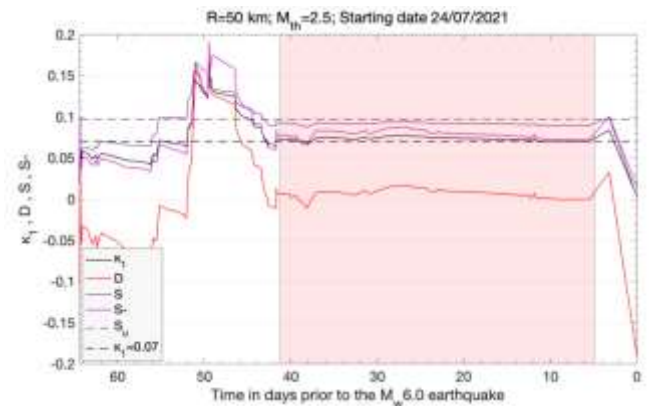
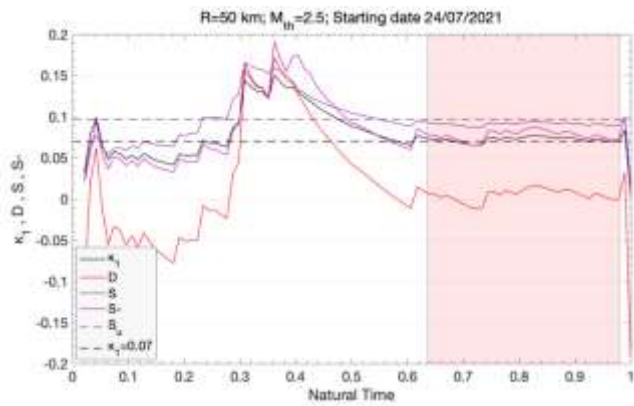
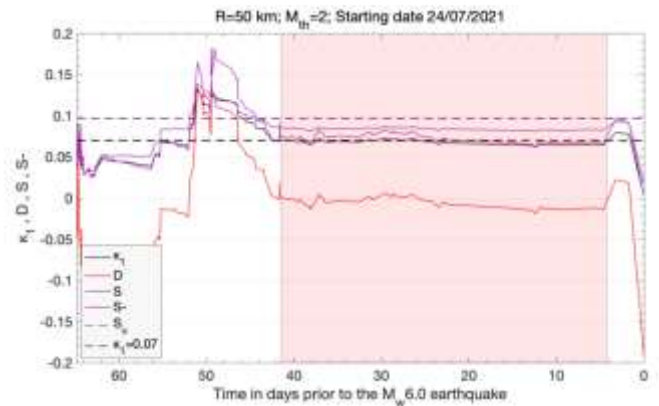
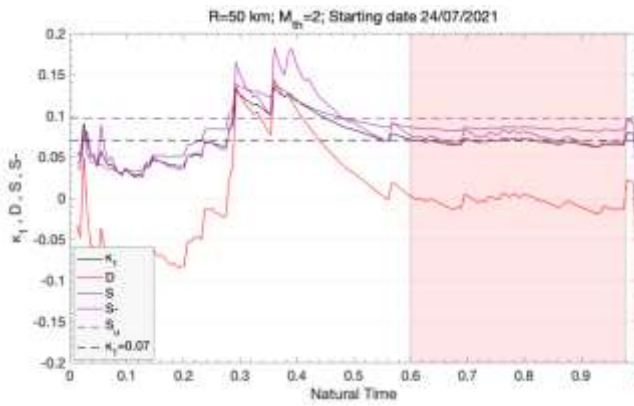
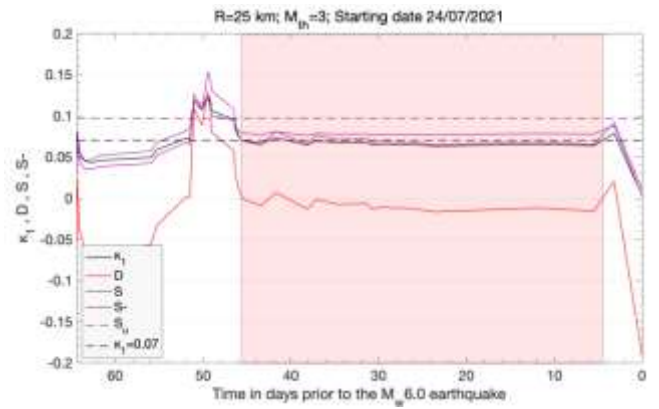
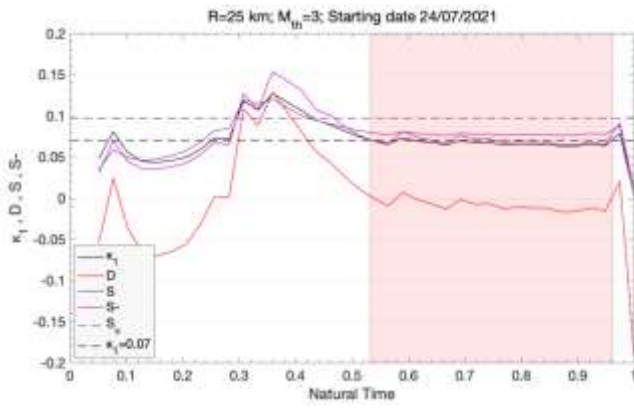


**Figure 9.** Time evolution of the NT analysis parameters  $\kappa_1$ ,  $D$ ,  $S_{nt}$  and  $S_{nt-}$ , as they evolve event by event prior to the Central Crete  $M_w$ 6.0 mainshock in Natural Time (left column) and conventional time (days; right column), considering a radius  $R = 25$  km (top 3 rows) and 50 km (bottom 3 rows) around the  $M_w = 6.0$  epicenter and a magnitude threshold,  $M_{th} = 2.0, 2.5$  and 3.0. The dashed horizontal lines indicate the entropy limit of  $S_u = 0.0966$  and the value  $\kappa_1 = 0.070$ . The shaded rectangle marks the time when the critical stage of  $\kappa_1 = 0.070$  is approached.

### 3. Concluding Remarks

In the present work, the evolution of the regional patterns of seismicity in the area of the Central Crete ( $M_w$ 6.0) strong earthquake on September 27, 2021, investigated, using MRWA and NT analysis. The applied methods have suggested as able to define the when the fault system is in a critical stage during the preparation process of a major earthquake. The analysis was performed in the natural time domain, with an approximate starting point indicated by MRWA. The latter showed a decrease in the standard deviation of the wavelet coefficients  $\sigma_{wav}(m)$  at much lower scales, similar to the observations in [27, 58] prior to the occurrence of major events. Within this joint approach, the initial application of MRWA in regional seismicity around the epicenter, and for a wide time period before the mainshock, indicated a time segment where the NT analysis was applied in order to explore possible indicators that suggested the entrance to a critical stage. We note that the epicenter could have been also determined in advance by following the procedure described in [61].

The results demonstrated that regional seismicity approached criticality for a prolonged period of approximately 40 days before the  $M_w$ 6.0 earthquake that occurred on September 27, 2021 on-shore of Central Crete, in agreement with the results in [58]. In other words, the NT analysis parameters  $\kappa_1$ ,  $D$ ,  $S_{nt}$  and  $S_{nt-}$ , that characterizes the evolution of the regional seismicity, approach the theoretical values of critical point phenomena for a prolonged period of 40 days before the  $M_w$ 6.0 mainshock, in a similar way to that of non-equilibrium critical systems. Hence, the analysis of the regional seismicity in the natural time domain, initiated at approximately the time marks indicated by the results of MRWA, pointed to an approximate date of the impending large  $M_w$ 6.0 earthquake of Central Crete, within a narrow time window in the order of a few days. These results lay further support to the methodology introduced in [27, 58] regarding the combination of MRWA and NT analyses for the identification of critical stages of regional seismicity prior to strong earthquakes, providing a novel and promising framework for better understanding the evolution of earthquake generation processes.

### References

- McKenzie, D. Active Tectonics of the Mediterranean Region. *The Geophysical Journal of the Royal Astronomical Society* **1972**, 30,109–185, DOI: 10.1111/j.1365-246X.1972.tb02351.x.
- Le Pichon, X.; Angelier, J. The Hellenic Arc and Trench System: a key to the neotectonic evolution of the eastern Mediterranean area. *Tectonophysics* **1979**, 60, 1–42.
- Reilinger, R.; McClusky, S.; Paradissis, D.; Ergintav, S.; Vernant, P. Geodetic constraints on the tectonic evolution of the Aegean region and strain accumulation along the Hellenic subduction zone. *Tectonophysics* **2010**, 488, 22–30. 10.1016/j.tecto.2009.05.027.
- Comninakis, P.; Papazachos, B. Space and time distribution of the intermediate focal depth earthquakes in the Hellenic Arc. *Tectonophysics* **1980**, 70, T35–T37.
- Delibasis, N.; Ziazia, M.; Voulgaris, N.; Papadopoulos, T.; Stavrakakis, G.; Papanastassiou, D.; Drakatos, G. Microseismic activity and seismotectonics of Heraklion Area (central Crete Island, Greece). *Tectonophysics* **1999** 308, 227–248.
- Armijo, R.; Lyon-Caen, H.; Papanastassiou, D. East-west extension and Holocene normal faults scraps in the Hellenic arc. *Geology* **1992**, 20, 491–494.
- Shaw, B.; Jackson, J. Earthquake mechanisms and active tectonics of the Hellenic subduction zone. *Geophysical Journal International* **2010**, Vol 181, 2, 966–984, DOI: 10.1111/j.1365-246X.2010.04551.x.
- Ten Veen, J.H.; Meijer, P.T. Late Miocene to recent tectonic evolution of Crete (Greece): geological observations and model analysis. *Tectonophysics* **1998**, 298, 1–3, 191–208, DOI: 10.1016/S0040-1951(98)00184-X.
- Caputo R.; Catalano, S.; Monaco, C.; Romagnoli, G.; Tortorici, G.; Tortorici, L. Active faulting on the island of Crete (Greece), *Geophys. J. Int.* **2010**, 183, 111–126, doi: 10.1111/j.1365-246X.2010.04749.x.
- Vallianatos, F.; Kokinou, E.; Sammonds, P. Non Extensive statistical physics approach to fault population distribution. A case study from the Southern Hellenic Arc (Central Crete) *Acta Geophysica* **2011**, 59(4), 770–784.
- Vasilakis, E. Study of the tectonic features of the Messara Basin, Central Crete with remote sensing and GIS. PhD thesis **2006**. National and Kapodistrian University of Athens, Section of Geophysics—Geothermics, Department of Geology and Geoenvironment.
- Caputo, R.; Catalano, S.; Monaco, C.; Romagnoli, G.; & al., e. Middle-late quaternary geodynamics of Crete, southern Aegean, and seismotectonic implications. *Bulletin of the Geological Society of Greece* **2010**, 43(1), 400–408, doi: https://doi.org/10.12681/bgsg.11191
- Caputo, R.; Pavlides, S. *Greek Database of Seismogenic Sources (GreDaSS)*; Università Degli Studi di Ferrara: Ferrara, Italy, 2013.
- Bak, P.; Tang, C. Earthquakes as a self-organized critical phenomenon. *J. Geophys. Res. Space Phys.* **1989**, 94, 15635–15637, doi:10.1029/jb094ib11p15635.
- Kiyashchenko, D.; Smirnova, N.; Troyan, V.; Vallianatos, F. Dynamics of multifractal and correlation characteristics of the spatio-temporal distribution of regional seismicity before the strong earthquakes. *Nat. Hazards Earth Syst. Sci.* **2003**, 3, 285–298.

16. Kiyashchenko, D.; Smirnova, N.; Troyan, V.; Vallianatos, F. Seismic hazard precursory evolution: Fractal and multifractal aspects. *Phys. Chem. Earth* **2004**, *29*, 367–378.
17. Michas, G.; Vallianatos, F.; Sammonds, P. Non-extensivity and long-range correlations in the earthquake activity at the West Corinth rift (Greece). *Nonlinear Process. Geophys.* **2013**, *20*, 713–724, doi:10.5194/npg-20-713-2013.
18. Rundle, J.B.; Turcotte, D.L.; Shcherbakov, R.; Klein, W.; Sammis, C. Statistical physics approach to understanding the multiscale dynamics of earthquake fault systems. *Rev. Geophys.* **2003**, *41*(4), 5-1 – 5-30.
19. Sornette, D. *Critical Phenomena in Natural Sciences*; Springer: Berlin/Heidelberg, Germany, 2000.
20. Tsallis, C. *Introduction to Nonextensive Statistical Mechanics: Approaching a Complex World*; Springer: Berlin, Germany, 2009.
21. Uritsky, V.; Smirnova, N.; Troyan, V.; Vallianatos, F. Critical dynamics of fractal fault systems and its role in the generation of pre-seismic electromagnetic emissions. *Phys. Chem. Earth* **2004**, *29*, 473–480, doi:10.1016/j.pce.2003.11.015.
22. Vallianatos, F.; Michas, G.; Benson, P.; Sammonds, P. Natural time analysis of critical phenomena: The case of acoustic emissions in triaxially deformed Etna basalt. *Phys. A Stat. Mech. Appl.* **2013**, *392*, 5172–5178.
23. Vallianatos, F.; Michas, G.; Papadakis, G. Non-extensive and natural time analysis of seismicity before the Mw6.4, October 12, 2013 earthquake in the South West segment of the Hellenic Arc. *Phys. A Stat. Mech. Appl.* **2014**, *414*, 163–173, doi:10.1016/j.physa.2014.07.038.
24. Chatzopoulos, G. Accelerating deformation seismicity patterns before the 3 March 2021 Thessaly strong earthquake. First results. *Bull. Geol. Soc.* **2021**, *58*, 87–104, doi:10.12681/bgsg.27155.
25. Telesca, L.; Lapenna, V.; Alexis, N. Multiresolution wavelet analysis of earthquakes. *Chaos Solitons Fractals* **2004**, *22*, 741–748, doi:10.1016/j.chaos.2004.02.021.
26. Telesca, L.; Hloupis, G.; Nikolintaga, I.; Vallianatos, F. Temporal patterns in southern Aegean seismicity revealed by the multiresolution wavelet analysis. *Commun. Nonlinear Sci. Numer. Simul.* **2007**, *12*, 1418–1426.
27. Vallianatos, F.; Michas, G.; Hloupis, G. Multiresolution wavelets and natural time analysis before the January–February 2014 Cephalonia (Mw6.1 & 6.0) sequence of strong earthquake events. *Phys. Chem. Earth* **2015**, *85*, 201–209.
28. Uyeda, S.; Kamogawa, M.; Tanaka, H. Analysis of electrical activity and seismicity in the natural time domain for the volcanic-seismic swarm activity in 2000 in the Izu Island region, Japan. *J. Geophys. Res. Space Phys.* **2009**, *114*, 2310, doi:10.1029/2007jb005332.
29. Varotsos, P.A.; Sarlis, N.; Skordas, E.; Lazaridou, M.S. Natural entropy fluctuations discriminate similar-looking electric signals emitted from systems of different dynamics. *Phys. Rev. E* **2005**, *71*, 11110, doi:10.1103/physreve.71.011110.
30. Varotsos, P.; Sarlis, N.; Tanaka, H.K.; Skordas, E. Similarity of fluctuations in correlated systems: The case of seismicity. *Phys. Rev. E* **2005**, *72*, 41103, doi:10.1103/physreve.72.041103.
31. Varotsos, P.A.; Sarlis, N.; Skordas, E.; Tanaka, H.K.; Lazaridou, M.S. Entropy of seismic electric signals: Analysis in natural time under time reversal. *Phys. Rev. E* **2006**, *73*, 31114, doi:10.1103/physreve.73.031114.
32. Varotsos, P.A.; Skordas, E.; Sarlis, N.; Lazaridou, M.S. Fluctuations, under time reversal, of the natural time and the entropy distinguish similar looking electric signals of different dynamics. *J. Appl. Phys.* **2008**, *103*, 14906, doi:10.1063/1.2827363.
33. Varotsos, P.; Sarlis, N.; Skordas, E. Detrended fluctuation analysis of the magnetic and electric field variations that precede rupture. *Chaos Interdiscip. J. Nonlinear Sci.* **2009**, *19*, 23114, doi:10.1063/1.3130931.
34. Varotsos, P.A.; Sarlis, N.; Skordas, E.S. Natural Time Analysis: The New View of Time. In *Natural Time Analysis: The New View of Time*; Springer: New York, NY, USA, 2011.
35. Varotsos, P.; Sarlis, N.V.; Skordas, E.S.; Uyeda, S.; Kamogawa, M. Natural time analysis of critical phenomena. *Proc. Natl. Acad. Sci. USA* **2011**, *108*, 11361–11364, doi:10.1073/pnas.1108138108.
36. Sarlis, N.; Skordas, E.; Lazaridou, M.S.; Varotsos, P. Investigation of seismicity after the initiation of a Seismic Electric Signal activity until the main shock. *Proc. Japan Acad. Ser. B* **2008**, *84*, 331–343.
37. Sarlis, N.; Skordas, E.; Varotsos, P. Multiplicative cascades and seismicity in natural time. *Phys. Rev. E* **2009**, *80*, 22102, doi:10.1103/physreve.80.022102.
38. Sarlis, N.; Skordas, E.; Varotsos, P. Nonextensivity and natural time: The case of seismicity. *Phys. Rev. E* **2010**, *82*, 21110, doi:10.1103/physreve.82.021110.
39. Abe, S.; Sarlis, N.V.; Skordas, E.S.; Tanaka, H.K.; Varotsos, P.A. Origin of the Usefulness of the Natural-Time Representation of Complex Time Series. *Phys. Rev. Lett.* **2005**, *94*, 170601, doi:10.1103/physrevlett.94.170601.
40. Saltas, V.; Vallianatos, F.; Triantis, D.; Stavrakas, I. Complexity in Laboratory Seismology: From Electrical and Acoustic Emissions to fracture. In *Complexity of Seismic Time Series*; Chelidze, T., Telesca, L., Eds.; Elsevier: Amsterdam, The Netherlands, 2018.
41. Thurner, S.; Lowen, S.B.; Feurstein, M.C.; Heneghan, C.; Feichtinger, H.G.; Teich, M.C. Analysis, Synthesis, and Estimation of Fractal-Rate Stochastic Point Processes. *Fractals* **1997**, *5*, 565–595, doi:10.1142/s0218348x97000462.
42. Abry, P.; Flandrin, P.; Taqqu, M.S.; Veitch, D. Wavelets for the analysis, estimation, and synthesis of scaling data. In *Self-Similar Network Traffic and Performance Evaluation*; Wiley: Hoboken, NJ, USA, 2000.
43. Abry, P.; Flandrin, P.; Taqqu, M.S.; Veitch, D. Self-similarity and long-range dependence through the wavelet lens. In *Theory and Applications of Long-Range Dependence*; Doukhan, P., Oppenheim, G., Taqqu, M.S., Eds.; Birkhäuser: Basel, Switzerland, 2002; pp. 527–556.
44. Wornell, G.W.; Gaumond, C.F. Signal Processing with Fractals: A Wavelet Based Approach. *J. Acoust. Soc. Am.* **1999**, *105*, 18, doi:10.1121/1.424548.
45. Teich, M.C.; Heneghan, C.; Lowen, S.B.; Turcott, R.G. Estimating the Fractal Exponent of Point Processes in Biological Systems Using Wavelet- and Fourier-Transform Methods. In *WAVELETS in Medicine and Biology*; Informa UK Limited: London, UK, 2017; pp. 383–412.
46. Evangelidis, C.P.; Triantafyllis, N.; Samios, M.; Boukouras, K.; Kontakos, K.; Ktenidou, O.-J.; Fountoulakis, I.; Kalogeras, I.; Melis, N.S.; Galanis, O.; et al. Seismic Waveform Data from Greece and Cyprus: Integration, Archival, and Open Access. *Seism. Res. Lett.* **2021**, *92*, 1672–1684, doi:10.1785/0220200408.
47. Hloupis, G.; Papadopoulos, I.; Makris, J.P.; Vallianatos, F. The South Aegean seismological network—HSNC. *Adv. Geosci.* **2013**, *34*, 15–21.

48. Chatzopoulos, G.; Papadopoulos, I.; Vallianatos, F. The Hellenic seismological network of Crete (HSNC): Validation and results of the 2013 aftershock sequences. *Adv. Geosci.* **2016**, *41*, 65–72.
49. Chouliaras, G. Investigating the earthquake catalog of the National Observatory of Athens. *Natural Hazards Earth System Sciences* **2009**, *9*, 905–912, doi:10.5194/nhess-9-905-2009
50. Chouliaras, G.; Melis, N.S.; Drakatos, G.; Makropoulos, K. Operational network improvements and increased reporting in the NOA (Greece) seismicity catalog. *Advances in Geosciences* **2013**, *36*, 7–9, doi:10.5194/adgeo-36-7-2013.
51. Mignan, A.; Chouliaras, G. Fifty Years of Seismic Network Performance in Greece (1964–2013): Spatiotemporal Evolution of the Completeness Magnitude. *Seismological Research Letters* **2014**, *85* (3): 657–667, doi:10.1785/0220130209
52. National Observatory of Athens Seismic Network (HL). International Federation of Digital Seismograph Networks. <https://doi.org/10.7914/SN/HL> (accessed on October 1st, 2021).
53. Godano, C.; Caruso, V. Multifractal analysis of earthquake catalogues. *Geophys. J. Int.* **1995**, *121*, 385–392.
54. Öncel, A.O.; Main, I.G.; Alptekin, O.; Cowie, P.A. Spatial variation in the fractal properties of seismicity in the north Anatolian fault zone. *Tectonophysics* **1996**, *257*, 189–202.
55. Hainzl, S.; Scherbaum, F.; Beauval, C. Estimating Background Activity Based on Interevent-Time Distribution. *Bull. Seismol. Soc. Am.* **2006**, *96*, 313–320.
56. Corral, Á.; Christensen, K. Comment on “Earthquakes Descaled: On Waiting Time Distributions and Scaling Laws.” *Phys. Rev. Lett.* **2006**, *96*, 109801, doi:10.1103/PhysRevLett.96.109801.
57. Abe, S.; Suzuki, N. Scale-free statistics of time interval between successive earthquakes. *Phys. A Stat. Mech. Appl.* **2005**, *350*, 588–596, doi:10.1016/j.physa.2004.10.040.
58. Vallianatos, F., Michas, G., & Hloupis, G. (2021). Seismicity Patterns Prior to the Thessaly (Mw6.3) Strong Earthquake on 3 March 2021 in Terms of Multiresolution Wavelets and Natural Time Analysis. *Geosciences*, *11*(9), 379.
59. Sarlis, N.V.; Skordas, E.S.; Varotsos, P.A. Order parameter fluctuations of seismicity in natural time before and after mainshocks. *Europhysics Letters* **2010**, *91*, 59001
60. Varotsos, P.A.; Sarlis, N.V.; Skordas, E.S. Study of the temporal correlations in the magnitude time series before major earthquakes in Japan. *Journal of Geophysical Research: Space Physics* **2014**, *119*, 9192–9206, doi:10.1002/2014JA020580.
61. Sarlis, N.V.; Skordas, E.S.; Varotsos, P.A.; Nagao, T.; Kamogawa, M.; Uyeda S. Spatiotemporal seismicity variations and epicenter. *Proceedings of the National Academy of Sciences* **2015**, *112* (4) 986–989; DOI: 10.1073/pnas.142289311
62. Ngui, W. K., Leong, M. S., Hee, L. M., & Abdelrhman, A. M. (2013). Wavelet Analysis: Mother Wavelet Selection Methods. *Applied Mechanics and Materials*, *393*, 953–958. <https://doi.org/10.4028/www.scientific.net/amm.393.953>
63. D.R. Wijayaab, R. Sarnoa, E. Zulaikac, Information Quality Ratio as a novel metric for mother wavelet selection, *Chemometrics and Intelligent Laboratory Systems*, Vol.160, 15 January 2017, Pages 59-71



## **Chapter 3**

Satellite-Observed Thermal Anomalies and  
Deformation Patterns Associated  
to the 2021, Central Crete  
Seismic Sequence

**Abstract:** Nowadays, there has been a growing interest in understanding earthquake forerunners, i.e., anomalous variations that are possibly associated with the complex process of earthquake evolution. In this context, the Robust Satellite Technique was coupled with 10 years (2012–2021) of daily night-time MODIS-Land Surface Temperature remote sensing data to detect thermal anomalies likely related to the 27 September 2021, strong onshore earthquake of magnitude Mw6.0 occurring near the Arkalochori village in Central Crete, Greece. Eight intense (signal-to-noise ratio  $> 3$ ) and infrequent, quite extensive, and temporally persistent thermal signal transients were detected and characterized as pre-seismic anomalies, while one thermal signal transient was identified as a co-seismic effect on the day of the main tectonic event. The thermal anomalies dataset was combined with tectonic parameters of Central Crete, such as active faults and fault density, seismogenic zones and ground displacement maps produced using Sentinel-1 satellite imagery and the Interferometric Synthetic Aperture Radar technique. Regarding the thermal anomaly of 27 September, its greatest portion was observed over the footwall part of the fault where a significant subsidence up to 20 cm exists. We suggest that the thermal anomalies are possibly connected with gas release which happens due to stress changes and is controlled by the existence of tectonic lines and the density of the faults, even if alternative explanations could not be excluded.

---

## 1. Introduction

Recently, a growing interest in the physics of precursors that could be used to develop a system for short-term (days to weeks) forecasting of strong earthquake events and support the understanding of the evolution of seismicity exists [1]. To create a multiparametric prediction system, it would first be necessary to identify the parameters whose anomalous variants might be potentially related to the complex and dynamic tectonic processes [2,3].

Among the various parameters, variations in the Earth's emitted thermal radiation measured by space-born sensors operating in the thermal infrared (TIR) spectrum and the variations on the Earth's surface deformation recorded by satellite radar interferometry have long been suggested as potential precursors [3,4]. Nevertheless, although much research has been undertaken on the investigation of several precursors simultaneously (e.g., [5]), the analysis of patterns of the different parameters has attracted less attention.

Several satellite sensors, which have channels in the infrared portion of the electromagnetic spectrum, can monitor Earth's thermal field and generate a Land Surface Temperature (LST) product with variable spatiotemporal resolution depending on the satellite/sensor system chosen [6–9]. Therefore, LST can be used as a critical guide to the understanding of land surface processes at various scales [10–20] and environments, especially in areas with a variability in geophysical parameters such as vegetation, topography, geology and geomorphometry.

On 27 September 2021, a rare and strong onshore earthquake of magnitude Mw6.0 occurred in Central Crete, near the village of Arkalochori at 06:17:21 UTC [21]. The epicenter of the seismic event was located at latitude 35.15 N and longitude 25.27 E, while the focal depth was about 10 km and associated with the Kastelli Fault Zone [22] whose mean recurrence interval has been estimated at approximately 800 years [23]. Since the beginning of June, almost 4 months earlier, a significant number of foreshocks had been recorded in the broader area, while a rich aftershock sequence was observed in the months after the main shock occurrence [21,22,24,25]. On 24 July, a strong preseismic event appeared with magnitude Mw4.8. After that, more than 250 earthquakes with magnitudes up to 3.8 were recorded in an approximately N-S-oriented, 15-km-long area west of Arkalochori until the occurrence of the main event [24,26]. Eight aftershocks of magnitudes equal to or greater than M4.2 occurred during the day of the main event, while the strongest aftershock occurred on 28 September with Mw5.3. The earthquake had devastating consequences in the area near the Arkalochori village as one person lost his life, while many buildings collapsed affecting thousands of people.

The objective of the present work is to identify thermal anomalies associated with the rare major tectonic deformation event of Central Crete and to correlate them with co-seismic regional crustal deformation. Thermal and

crustal deformation anomalies will be calculated using data mining techniques over a period of three months before and one month after the occurrence of the earthquake; similarities or discrepancies between the behavioral changes of these anomalies will then be analyzed. Based on a preliminary analysis, we note that in the period May 2021 to July 2021, where the first foreshock appeared, no thermal anomalies were observed in the region.

The Robust Satellite Techniques (RST) [27–29] was used to detect the spatial evolution of thermal anomalies probably connected with the evolution of the seismic sequence. During the last two decades, the RST has been widely used to distinguish thermal signals possibly related with earthquake evolution from variations in the Earth’s thermal emission due to other phenomena [27–29]. For the RST, any anomaly in the space–time domain is considered as a deviation from a “normal” behavior. The latter can be calculated by processing a multiyear dataset of cloud-free satellite images of the same month, the same spectral channel (s) and the same acquisition times.

In addition, the regional co-seismic deformation was mapped using the Interferometric Synthetic Aperture Radar (InSAR) technique. The term SAR stands for Synthetic Aperture Radar [30]. SAR systems that record microwave radiation are called active because of their ability to emit pulses of microwave radiation lasting a few minutes, thus being autonomous sources of energy. The recording of the pulse return time by the satellite sensors determines the position of the earth features on the image. Compared to conventional geodetic methods, the ability of radar to measure distances through time and at an angle, over long distances from either two different systems or with repeated shots of the same system was a new technique, Interferometric SAR (InSAR). Differential Interferometry (Differential InSAR technique-DInSAR) is an advanced technique [31] aimed at detecting surface movements due to geophysical phenomena or human interventions. Since the 1990s, the DInSAR technique has proven to be an interesting tool for measuring and observing ground deformation suitable for analyzing geodynamic processes (e.g., [32–35]). In this context, we used SAR images of the Sentinel-1 Copernicus satellite in both ascending and descending orbits to create the differential interferograms and to produce deformation patterns through phase unwrapping, using open ESA’s SNAP software.

The contribution of the present work is to study thermal anomalies observed before a very rare and strong earthquake event. Its innovation is that it associates the observed thermal anomalies with regional tectonic characteristics. We note that the thermal anomalies mapped in the area are coupled with co-seismic deformation patterns observed by the InSAR method.

## 2. Geotectonic Setting

Crete is situated at the southernmost part of the Hellenic Island arc and has high seismic activity due to the subduction of the African plate underneath the Eurasian plate [36–38]. Both extensional and compressional stresses that exist in this area result in the creation of an extremely complex tectonic environment characterized by significant horizontal and vertical movements [39]. The Heraklion tectonic graben to the north and the Messara tectonic graben in the southwest dominate the central Crete region on shore (Figure 1).

The Heraklion graben is bounded on the west by the Ida Mountains and on the east by the Dicti Mountains along the eastern Psiloritis and Kastelli fault zones, respectively, [39–41]. Both fault zones exhibit an almost NE–SW direction, with the eastern Psiloritis fault zone being more prominent due to the topography of the Ida Mountains. The Messara graben is bounded to the north by the Ida Mountains and to the south by the Asteroussia Mountains, along two EW oriented fault zones (Figure 1). According to previous studies [38,41,42] the faults on Central Crete can be classified in four groups. The first group consists of E–W trending faults that cut mainly bedrock or bound bedrock and Miocene sediments. The second group consists of large and medium N–S striking faults that cut the aforementioned group. The third and fourth groups are trending towards NE–SW and NW–SE, respectively. The geology of the area of interest is composed mainly of Miocene to Pliocene sediments which cover the central and western part of the study area overlaid by Quaternary deposits forming depositional plains. The Neogene deposits were formed in terrestrial to deep marine environments, giving evidence for significant changes in depositional depths attributed to vertical movements and climatic changes [43]. Carbonates of the Tripolis nappe are exposed in the northeastern part of the area. Dissected hills of phyllites and quartzites coupled with Plattenkalk limestones are mainly outcroppings to the eastern part of the area of interest [43].

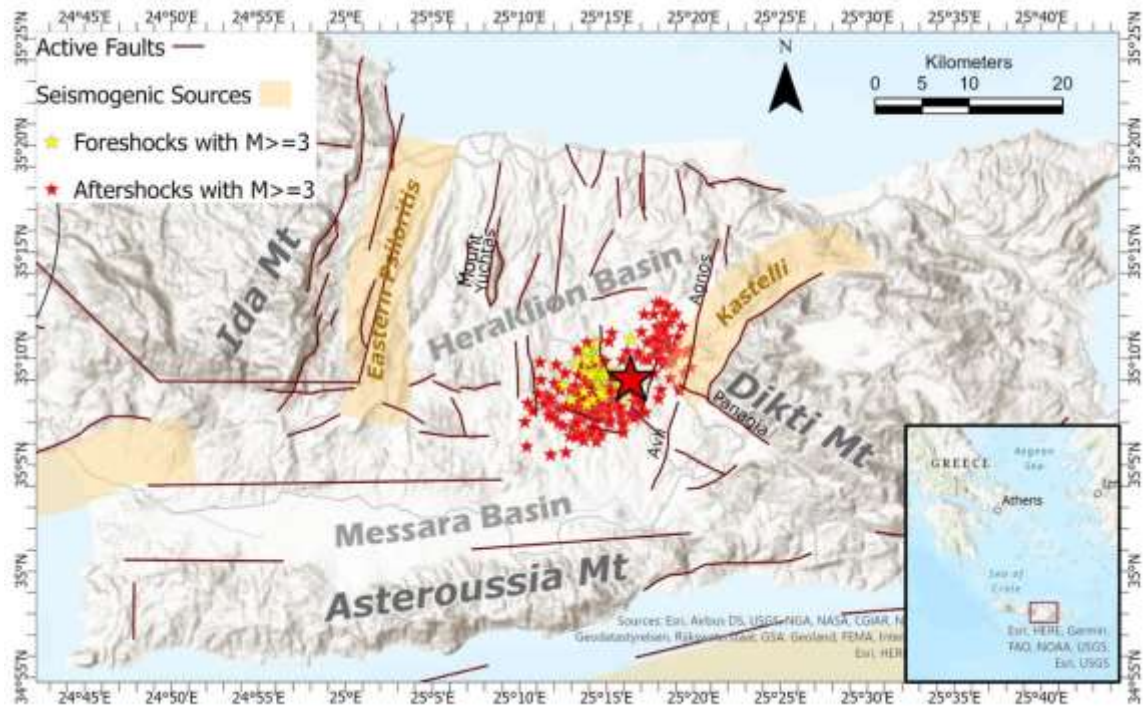


**Figure 1.** The map of Central Crete showing the epicenter of the main event and the foreshocks and aftershocks with magnitudes greater than or equal to M3.0 [26], the major active faults (adopted from [40]) and the seismogenic sources (adopted from [41]) located in the area.

### 3. Materials and Methods

#### 3.1. Robust Satellite Techniques

The Robust Satellite Technique (RST) [27–29] is applied herein to distinguish anomalous thermal variations probably related to earthquake activity from normal variations in Earth’s thermally emitted radiation due to other phenomena. The RST is a well-known multitemporal remotely sensed data analysis technique having as its main advantage the reduction of “natural noise” [28]. The cause of this “natural noise” can be the atmospheric weather or several variations in vegetation (natural or planted) or man-made constructions, topography and climate over space and time. As shown in previous works (e.g., [2,19,20,27,28,44,45]), the advantage of the RST methodology compared to other approaches is its ability to isolate residual thermal variations which are probably connected to tectonic activity. Over the past two decades, the RST method has been applied worldwide in several geotectonic regimes and to earthquakes with magnitudes greater than 4.0. Both polar and geostationary satellite images have been used, and connections between thermal anomalies and tectonic activity in a temporal window from 30 days before to 15 days after earthquakes occurrence have been found ([2] and references therein). Among others, TIR anomalies associated with the 7 September 1999, M5.9 earthquake in Athens [44], to the M7.8 Izmit earthquake on 17 August 1999 [28] and to the M5.8 earthquake in Abruzzo (Italy) on 6 April 2009 [46] have been reported. Moreover, the 10 years analysis of continuous data over Greece by [45] showed the general correlation between earthquakes and the thermal anomalies computed by the RST. A similar investigation of RST capabilities recently took place in Turkey and confirmed a nonrandom correlation between RST-based thermal anomalies and earthquake occurrence [20].

In the present work, the RETIRA-index computed as [28]:

$$\otimes_{\Delta T}(\mathbf{r}, t) = \frac{\Delta T(\mathbf{r}, t) - \mu_{\Delta T}(\mathbf{r})}{\sigma_{\Delta T}(\mathbf{r})} \quad (1)$$

where  $\mathbf{r} = (x, y)$  represents the accurate location of each pixel  $(x, y)$  on the satellite image,  $t$  is the acquisition time of the satellite image,  $\Delta T(\mathbf{r}, t)$  refers to the difference  $(T(\mathbf{r}, t) - T(t))$  of the observed TIR signal value  $T(x, y, t)$  with the spatial mean value  $T(t)$  of all the pixels of the satellite image.  $T(x, y, t)$  is measured for each pixel  $(\mathbf{r})$ , while  $T(t)$  is calculated in place on the satellite image, excluding the cloudy pixels;  $\mu_{\Delta T}(\mathbf{r})$  defines the time average and

$\sigma_{\Delta T}(\mathbf{r})$  the standard deviation of  $\Delta T(\mathbf{r},t)$  measured at site  $\mathbf{r}$ , computed only on cloud-free pixels of the homogenous satellite images.

The RETIRA index calculates the local spatiotemporal excess of the current  $\Delta T(\mathbf{r},t)$  signal over its historical mean value, weighted by its variability  $\sigma_{\Delta T}(x,y)$  at the given location. Using  $\Delta T(\mathbf{r},t)$  instead of  $T(\mathbf{r},t)$  reduces the possible contributions due to meteorological variations (e.g., periods of abnormally hot weather) and/or seasonal time changes. Note that the signal (S) is evaluated by comparing it to the standard deviation  $\sigma_{\Delta T}(\mathbf{r})$ ; therefore, the signal-to-noise ratio (S/N) can be used to characterize the intensity of anomalous thermal transients.

For the RETIRA index calculation, the MOD11A1 Version 6.1 product, available from 24 February 2000 was used. It provides daily per-pixel “Land Surface Temperature and Emissivity” with 1 km pixel size in a 1200 by 1200 km grid. The pixel temperature value is derived from the MOD11\_L2 ([https://doi.org/10.5067/MODIS/MOD11\\_L2.006](https://doi.org/10.5067/MODIS/MOD11_L2.006)), swath product [47]. The retrieved MODIS Land Surface Temperature uses the MODIS cloud mask product and as a result contains only cloud-free pixels. Images from LST were preferably taken at night because they are affected to a lesser extent by temperature differences between the ground and air than images taken at any other time of day. In addition, they are also less sensitive to local solar radiation variations and shade, an important source of land surface temperature variability not related to the seismic activity. Specifically, 10 years of remotely sensed data (from 2012 to 2021) were included in the calculation of the RETIRA index since the use of multi-year time series of satellite data is crucial to establish the required regional thermal background. Initially, the “Night-time and Surface Temperature” layer dataset was isolated for the 10-year period and then spatially subset to the Central Crete area. Monthly reference fields  $\mu_{\Delta T}(x,y)$  and  $\sigma_{\Delta T}(x,y)$  were then generated for the four months period, i.e., from July to October. Nevertheless, it has been shown that in cases where the cloudy fraction of the scene is greater than 80%, the remaining values lead to a non-reliable signal [45]. For this reason, such images were excluded from the computation of the final reference fields.

To identify any possible variations, a RETIRA index was calculated for each day of the period of 3 months before and a month after the main earthquake. We note that RETIRA is a Gaussian standardized variable, and the selection of its relative threshold value, quantitatively reflects the rareness and the significance of the identified anomalies. In this work, to define a thermal anomaly, we used a RETIRA index greater than 3, following a very strict rule as a distribution value greater than 3 or 4 suggests an anomaly with a probability 99.7% or 99.99%, respectively. In some cases, the computation of thermal anomalies is affected by relatively rare physical phenomena such as heat-waves, wildfires, cloud coverage and/or observational changes as in the case of inaccurate image navigation/co-location. The RETIRA index is based on time-averaged quantities and as shown in previous research [28,44,45] is sensitive to the abrupt appearance of extreme signal due to the abovementioned natural [48] or anthropogenic [44,49] phenomena. However, these signal variations are characterized by specific spatiotemporal patterns such as limited duration, similar and expected spatial distribution and known date of occurrence, allowing their exclusion from further analysis [28]. As a result, the RETIRA index anomalies related to seismicity were isolated from those due to wildfire and those induced by cloud-coverage or/and imprecise image navigation/co-location.

### 3.2. Interferometric Synthetic Aperture Radar (InSAR)

The Sentinel-1 mission of the European Commission (EC) and the European Space Agency (ESA), comprises a constellation of two polar-orbiting satellites, Sentinel-1A and Sentinel-1B, operating 24 hours per day with a short revisit cycle of 6 days. They are performing C-band synthetic aperture radar imaging under all weather conditions [50]. To map the co-seismic deformation due to the 27 September 2021 earthquake, we used one ascending and one descending SAR image pair (with acquisition dates of 23 September 2021–29 September 2021 and 25 September 2021–1 October 2021, respectively) from ESA’s Sentinel-1A and Sentinel-1B satellites. In both cases, the reference image was the one before the earthquake occurrence, while the repeat image was the one that refers to the date after the event.

Each reference–repeat pair was processed using the ESA’s open SNAP software, and two individual interferograms were generated. The topographic phase was subtracted using the SRTM 1 arc-second Digital Terrain Model, a 30 m resolution Shuttle Radar Topography Mission Digital Elevation Model (USGS 1 ARC-second SRTM DEM, <https://doi.org/10.5066/F7DF6PQS>, access on), while the signal-to-noise ratio was enhanced by applying the adaptive power spectrum filter of [51] with a coherence threshold of 0.4.

## 4. Results

We proceed now to present the results achieved after applying the RETIRA index and to compare them with the co-seismic crustal deformation pattern.

For a period of 10 years (i.e., 2012–2021) and for each of the 4 months spanning the period before and after the main event (i.e., July to October), 1230 images were obtained. Each cloud-free image contains 3525 pixels. The cloud-covered pixels in the images are recognized as “no data”, and as a result, pixels reduce as the cloud coverage increases. Finally, 1086 images were used in the calculation of the monthly reference fields  $\mu_{\Delta T}(x,y)$  and  $\sigma_{\Delta T}(x,y)$ . Then, the RETIRA index was computed for 105 images (i.e., for 105 of the 123 days in the period July to October 2022). Among the images used, 31 were in July, 31 in August, 28 in September and 15 in October. The remaining 20 images during September and October 2021 presented cloud cover greater than 80% and were therefore excluded from further analysis. The daily analysis led to the detection of 18 (out of the 105) images containing pixels with RETIRA values greater than three. Applying the previously described methodology to all MODIS-LST images from July 2021 to October 2021, we finally identified nine thermal anomalies, three for each of the months of July, August and September 2021 (Figures 2–4). During October 2021, there was no observed RETIRA index following the post-seismic thermal anomaly criteria.

In detail, eight quite intense (Signal/Noise > 3.0) and rare, spatially extensive TIR signal transients were identified before the main earthquake. The first was recorded on 2 July, a few hours after the occurrence of a M4.1 earthquake and three days before the 5 July M4.2 event. The second thermal anomaly was recorded on 30 July, 6 days after the 24 July M4.8 earthquake. A new thermal anomaly was mapped one day later (Figure 2). During 5, 10 and 29 August, three thermal anomalies were identified (Figure 3). We note that during August, the earthquake activity appeared with lower magnitude events, with the strongest on 8 August with a magnitude M3.8. The last two pre-seismic thermal anomalies were identified on 18 and 20 September, nine and seven days before the main event on 27 September, respectively, and the last thermal anomaly was detected on the day of the main earthquake (co-seismic anomaly) (Figure 4). As can be seen in Figures 2–4, in some cases the RETIRA index exceeded the value five (see dark brown pixels), and this could be used as an evaluation of the intensity of the thermal anomalous events. As for the spatial distribution of the observed thermal activity in Central Crete, the thermal anomaly of 2 July occurred to the south and east of the village of Arkalochori and occupied the southern part of the Kastelli seismogenic zone. In the northern part, the thermal anomaly spatially coincided with Mount Yuchtas, where a conjunction of two active tectonic faults exists. The 31 July thermal anomaly was also located near Mount Yuchtas and south of Arkalochori, while the thermal anomaly observed on 30 July was located to the south and was bounded by the two large faults, oriented east–west (Figure 2). On 5 August, one more thermal anomaly appeared near Mount Yuchtas northwest of Arkalochori. An extended thermal anomaly was identified on 10 August and occupied the previous area located further on north, south and southwest of Arkalochori. On 29 August, a much weaker, spatially limited thermal anomaly was located near Houdetsi village (Figure 3).

On 18 September, a thermal anomaly occurred north of the earthquake epicenter. Two days later, on 20 September, a RETIRA thermal anomaly with values up to 6.0 was observed over Mount Yuchtas, with the largest values occurring east of the mountain and extending to the south (Figure 4).

On the day of the earthquake occurrence, the thermal anomaly was located near an east–west oriented zone south of the epicenter, occupying an extensive area bounded by the villages of Metaxochori to the north and Ligortynos to the south, reaching as far as the vicinity of Arkalochori (Figure 4).

To visualize the frequency of thermal anomalies and their spatial distribution, Figure 5a was constructed. With the aim to define the areas where the thermal anomalies were spatiotemporally persistent, a map showing the frequency of the occurrence of thermal anomalies (i.e., the number of times a pixel participated in one of the nine identified thermal anomalies during the period from July to September 2021) was created. The frequency map of thermal anomalies was then compared with the normalized map of fault density obtained by calculating the density of linear features (faults) in the neighborhood of each output raster cell according to [52]. More specifically, a normalized lineament density map was created by counting the faults per unit area (number/km<sup>2</sup>), dividing the output by the maximum calculated density and then plotted in the respective grid centers.

The frequency ranges from one to four indicating that especially in the vicinity of Mount Yuchtas, the thermal anomalies were particularly persistent, as they occurred on four of the nine days in total. The frequency map of thermal anomalies was then compared with the normalized fault density map (Figure 5b). It is worth noting that the region north of the earthquake epicenter exhibits a medium-high value of fault density and the highest persistence of thermal anomalies, in contrast to the area south of Arkalochori, which shows anomalies with medium persistence and low fault density (Figure 5).

We proceed now to present the two co-seismic interferograms that emerged for the Arkalochori earthquake of 27 September 2021. The two wrapped (ascending and descending) interferograms are of good quality due to the low temporal geometric baselines and the high temporal resolution of Sentinel-1. As a result, the interferograms exhibit high coherence, with 80% and 68% at  $\geq 0.4$  and 0.6, respectively. They contain the phase difference between master and slave images produced by the main seismic event and its aftershocks until 29 September (ascending orbit) and 1 October (descending orbit). A clear pattern of six fringes, i.e., six concentric “circles” quite similar in shape, forming a lobe (Figure 6a,b), which is misaligned mainly due to the different geometry of the images in the two different orbits, is evident, indicating subsidence. Each interference fringe is a phase change which corresponds to motion of 2.8 cm in the satellite line of sight. The two wrapped interferograms were then used in the second stage; to calculate the terrain displacement, an unwrapping process was performed, and the phase unit was transformed into distance units in the line of sight (LoS) (differential interferograms) for every interferometric pair.

The InSAR results show that the area surrounding Arkalochori moved roughly downwards and are in a good agreement with previous works [21,22,53]. Note that dip-slip earthquakes have a very asymmetrical displacement pattern: i.e., the subsidence will be larger than the uplift for normal-faulting earthquakes. The terrain displacement products are similarly shifted. In the ascending orbit, we observe the epicenter of the main earthquake in the center of the ground deformation which has a maximum value of 18 cm (Figure 6c) which is the result of the superimposed effect of all the seismic events, mainly between 27 September and 29 September. In the descending orbit, the ground deformation has a maximum value of about 20 cm which results from the seismic events mainly between 27 September to 1 October and is located mainly east of the epicenter of the main earthquake (Figure 6d).

Finally, to map the vertical (up–down) and horizontal (east–west) displacement, decomposition of ascending and descending LOS displacement products was performed. After the decomposition, the ground deformation in the vertical (up–down) direction showed subsidence up to 20 cm, while no uplift displacement was detected (Figure 7a). The horizontal (east–west) displacement map indicated a maximum displacement of about 8 cm towards the east of the footwall block and about 6 cm towards the west of the hanging wall (Figure 7b) in agreement with that observed in [21,22] and modeled in [53], probably attributed to the strike–slip component of the earthquake focal mechanism as suggested in [21].

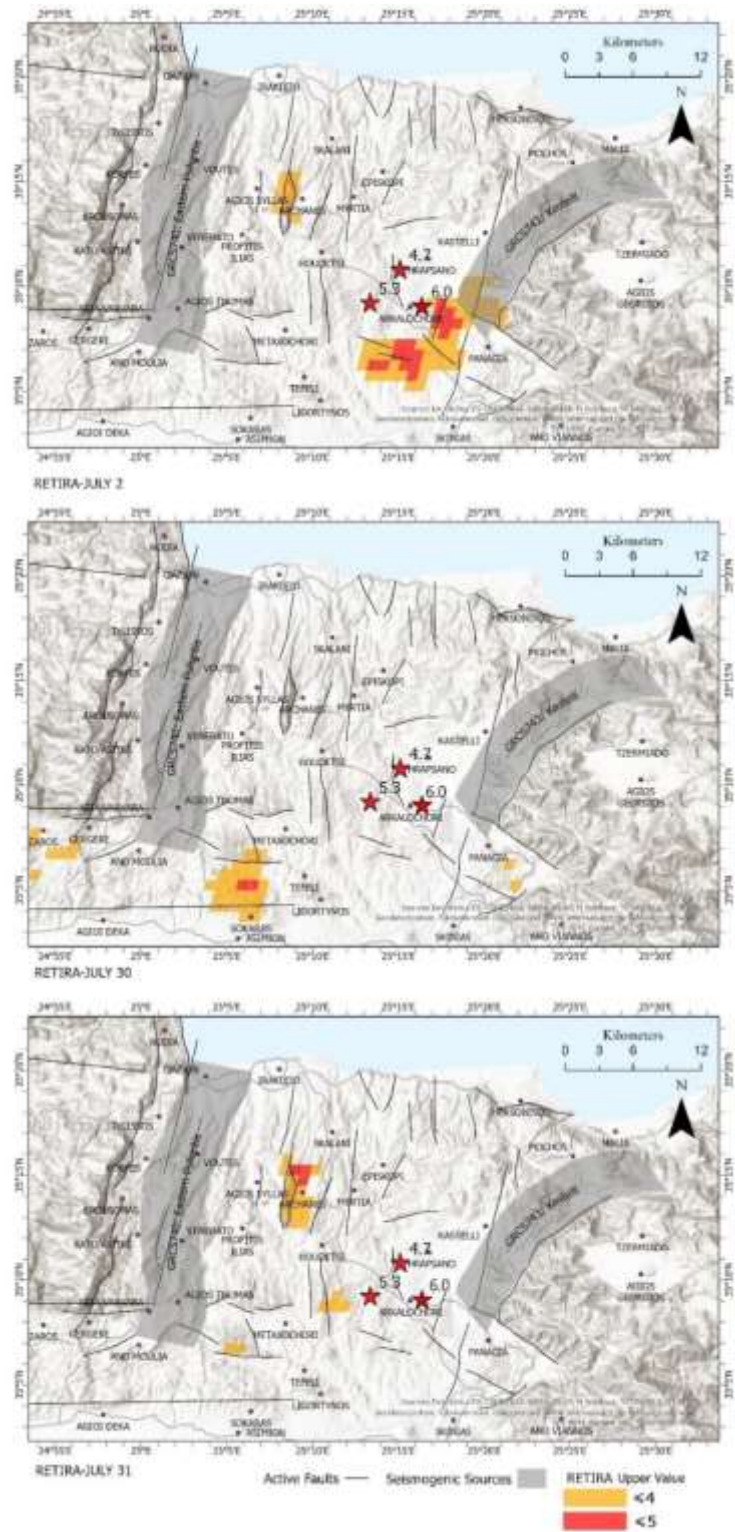


**Figure 2.** RETIRA thermal anomalies observed in the broader earthquake area of Central Crete during July 2021 are depicted with graduated colors depending on their value. The seismicogenic source zones and the active faults are also indicated.

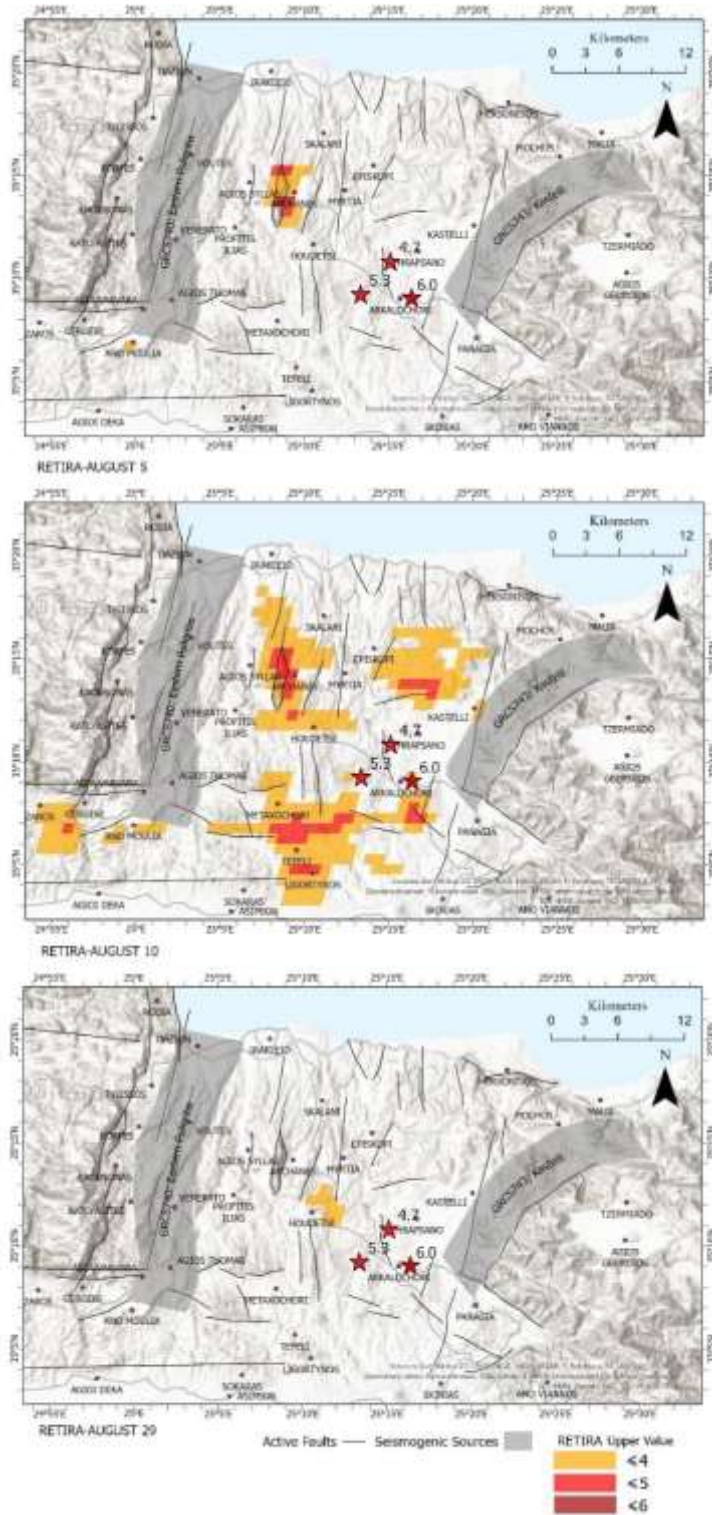


**Figure 3.** RETIRA thermal anomalies during August 2021 as observed on Central Crete are depicted with graduated colors depending on their value. The seismicogenic source zones and the active faults are also indicated.

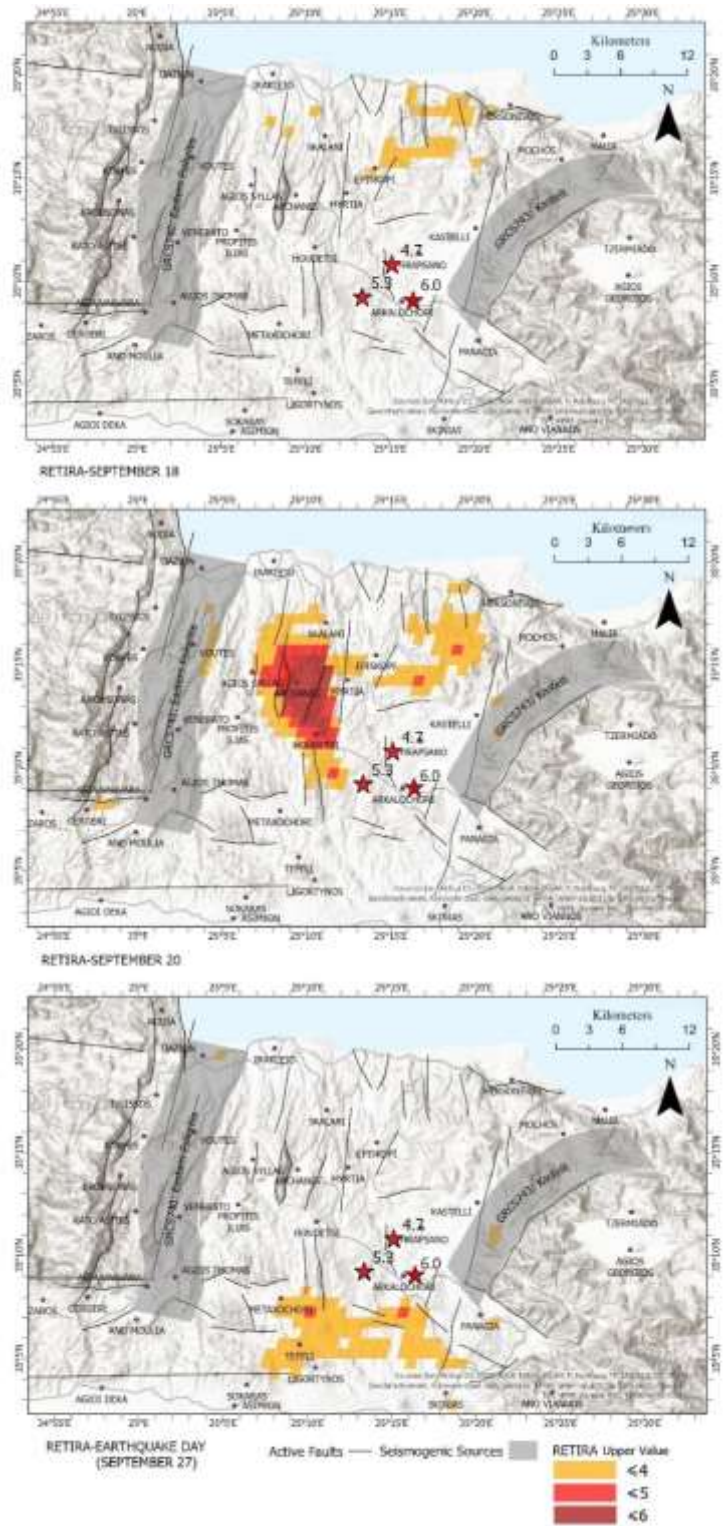


**Figure 4.** Pre-seismic and co-seismic (last image) RETIRA thermal anomalies of the broader earthquake area of Central Crete occurring during September 2021.

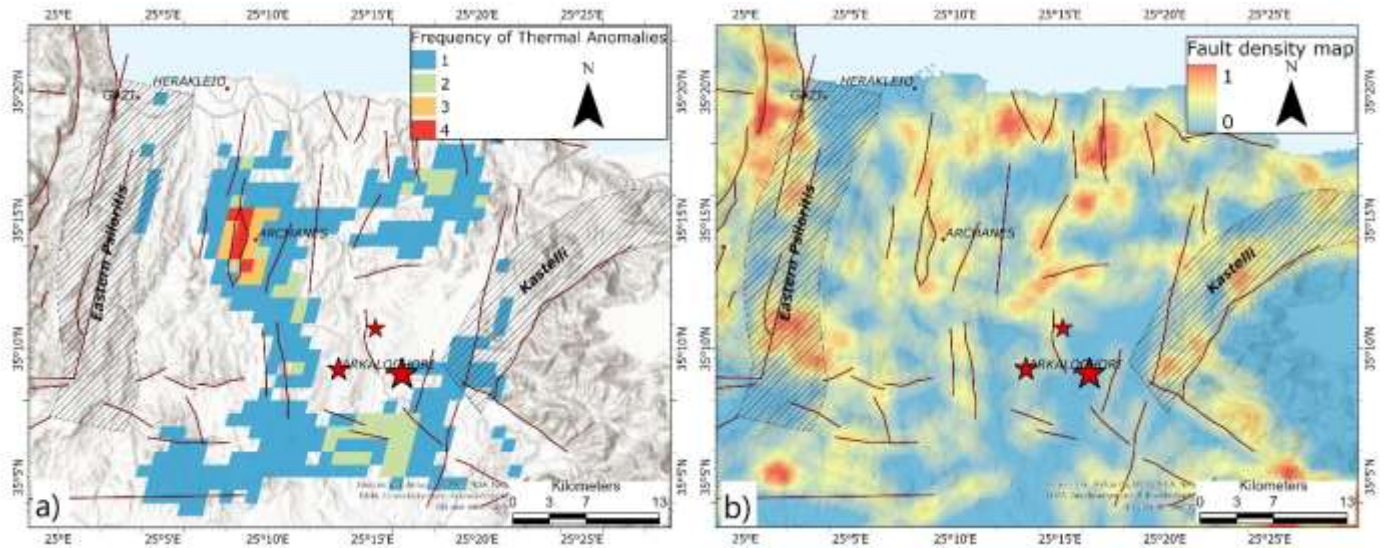


**Figure 5.** (a) Frequency map counting for each pixel the number of times it participated in one of the nine identified thermal anomalies during the pre-seismic period from July to September 2021; (b) normalized density faults map (see details in the text).

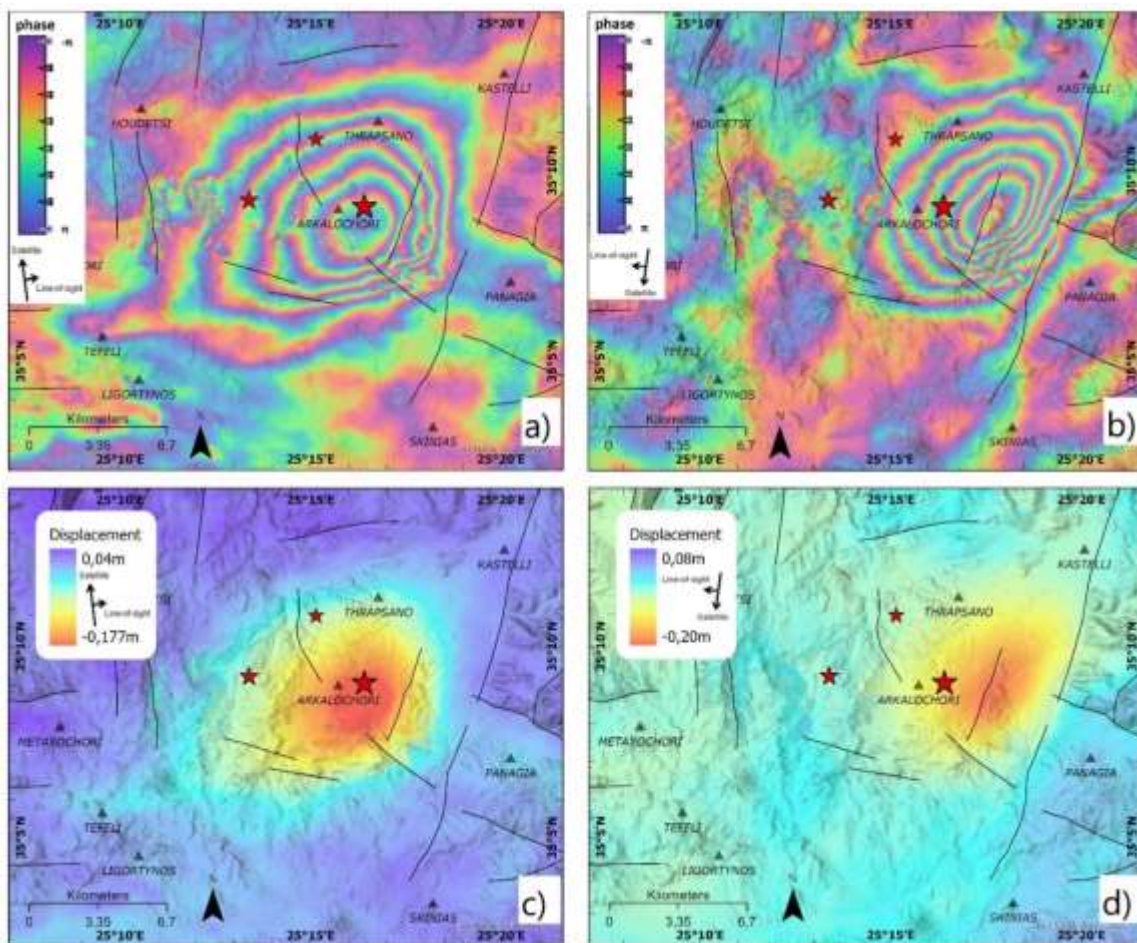


**Figure 6.** (a,b). Wrapped ascending (image pair 23 September–29 September 2021(track 102)) and descending (image pair 25 September–1 October 2021 (track 36)) co-seismic interferograms over the Arkalochori area; (c,d) LoS displacement maps in the ascending and descending orbit.

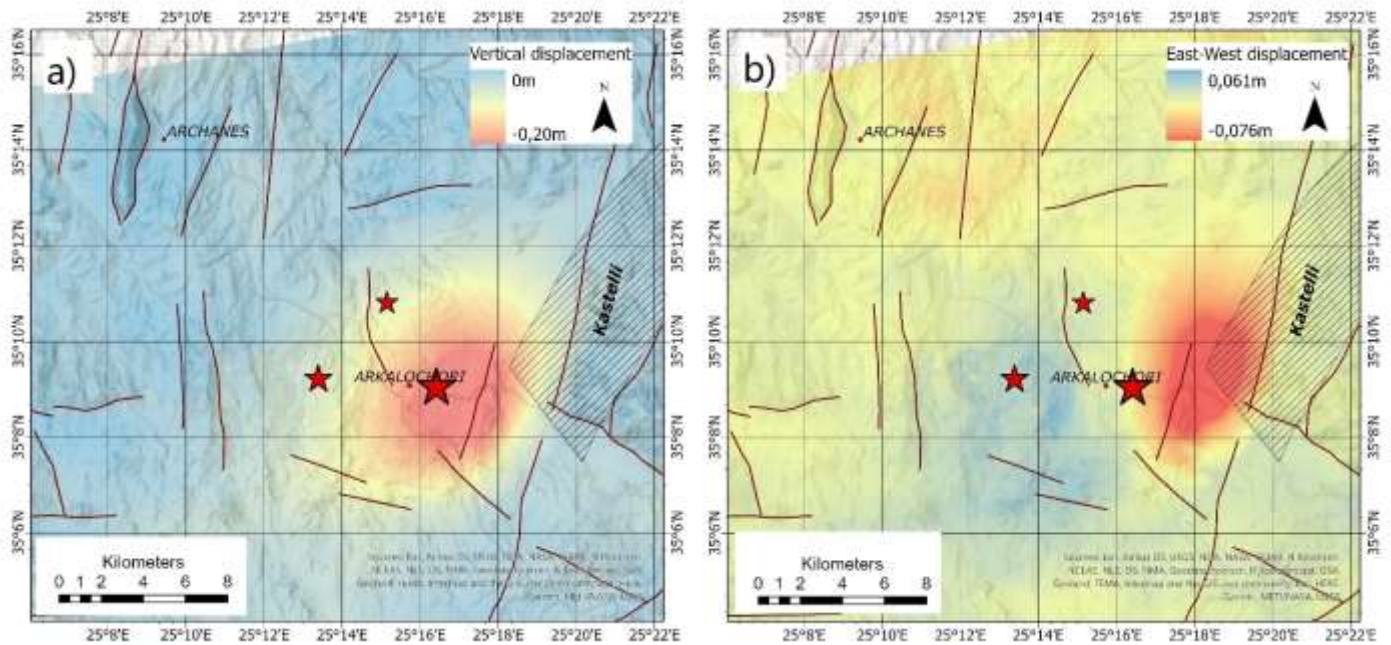


**Figure 7.** Displacement maps for: (a) the vertical (up–down); and (b) the E–W direction for Central Crete due to the 27 September 2021 earthquake overlain by the active faults of the broader area.

## 5. Discussion and Conclusions

In the present work the RST (Robust Satellite Technique) was used to detect and map thermal anomalies possibly associated to the 27 September 2021, strong, rare, and unexpected earthquake of magnitude Mw6.0 occurring on-shore of Central Crete (Greece), in the vicinity of Arkalochori village. A total of 10 years (2012–2021) of daily night-time Land Surface Temperature (LST) remote sensing data from Moderate Resolution Imaging Spectroradiometer (MODIS) were used to create the background pattern of the area. The seismic activity began several months before the main event, and nine intense (signal-to-noise ratio > 3), infrequent, spatially extensive, and temporally persistent TIR signal transients were identified from July to September 2021. Eight of them could be characterized as pre-seismic thermal anomalies, while the last one as co-seismic, since it was observed the day the main event occurred. Concerning their spatial distribution, five of the pre-seismic thermal anomalies coincided with the Mount Yuchtas area, while two (observed on 2 July and 10 August, respectively) were located south of Arkalochori village in the proximity of the Kastelli seismogenic source. Similar spatial distribution existed in the thermal anomaly observed during the day the main event occurred. The latter possibly implies that the two thermal anomalies observed south of the earthquake epicenter before the earthquake occurrence could be related to the future co-seismic displacement of the region due to the activation of the Kastelli zone.

Moreover, using InSAR patterns, we confirmed that the Mw = 6.0 earthquake and its strongest aftershock of 28 September 2021 (Mw5.3) produced mainly subsidence up to 20 cm combined with a less important horizontal eastward movement up to 6 cm and a westward movement up to 8 cm to the west and to the east of Arkalochori town respectively.

The superimposition of the frequency thermal anomaly map to the ground deformation maps (produced using Sentinel-1 satellite images) (Figure 8) reveals the existence of a common area in the south of Arkalochori village. As far as we know, this is the first time that the spatiotemporal correlation between the two different phenomena, i.e., thermally emitted radiation anomalies and the Earth's surface deformation, has been revealed.

Concerning the day the main event occurred, the two datasets partially overlap with a great portion of thermally anomalous pixels to be contained by the area that significantly deformed. This is more evident in the case of horizontal displacement where a significant portion of the thermal anomaly coincided with the westward-moving terranes and the southern part of the Kastelli fault zone.

What is worth noting is the fact that part of the deformed area was characterized as thermally anomalous twice during the four months (Figure 8). This observation, although needing further investigation, could be of great importance for the development of a short-term forecasting system of strong earthquake events.

Herein, we attempt to propose a preliminary physical mechanism for the observed thermal anomalies in agreement with the deformation pattern associated to the Mw6.0 main event. Thermal anomalies seem to exhibit a selective spatial distribution, as they appear to be preferentially concentrated in areas with high fault densities, such as areas where two faults are joined, as in the case of Mount Yuchtas. This significant increase of thermal radiation can be attributed to greenhouse gas (mainly CO<sub>2</sub> and CH<sub>4</sub>) reservoirs whose spatial relationship with seismogenic fault systems has been reported (e.g., [55,56]). As stated by [55], an increase of stress can cause the release of gases, such as CO<sub>2</sub>, CH<sub>4</sub> and N<sub>2</sub>, that are trapped in the pores of the rocks. The gases are released from the Earth's surface with the activation of cracks since micro-fracturing can lead to permeability changes and gas diffusion, which is supported by their high mobility [56,57]. In some cases, and especially in extensional tectonic environments, CO<sub>2</sub> is produced from the melting of subducted carbonates and accumulates in crustal reservoirs triggering earthquakes at crustal depth [58,59].

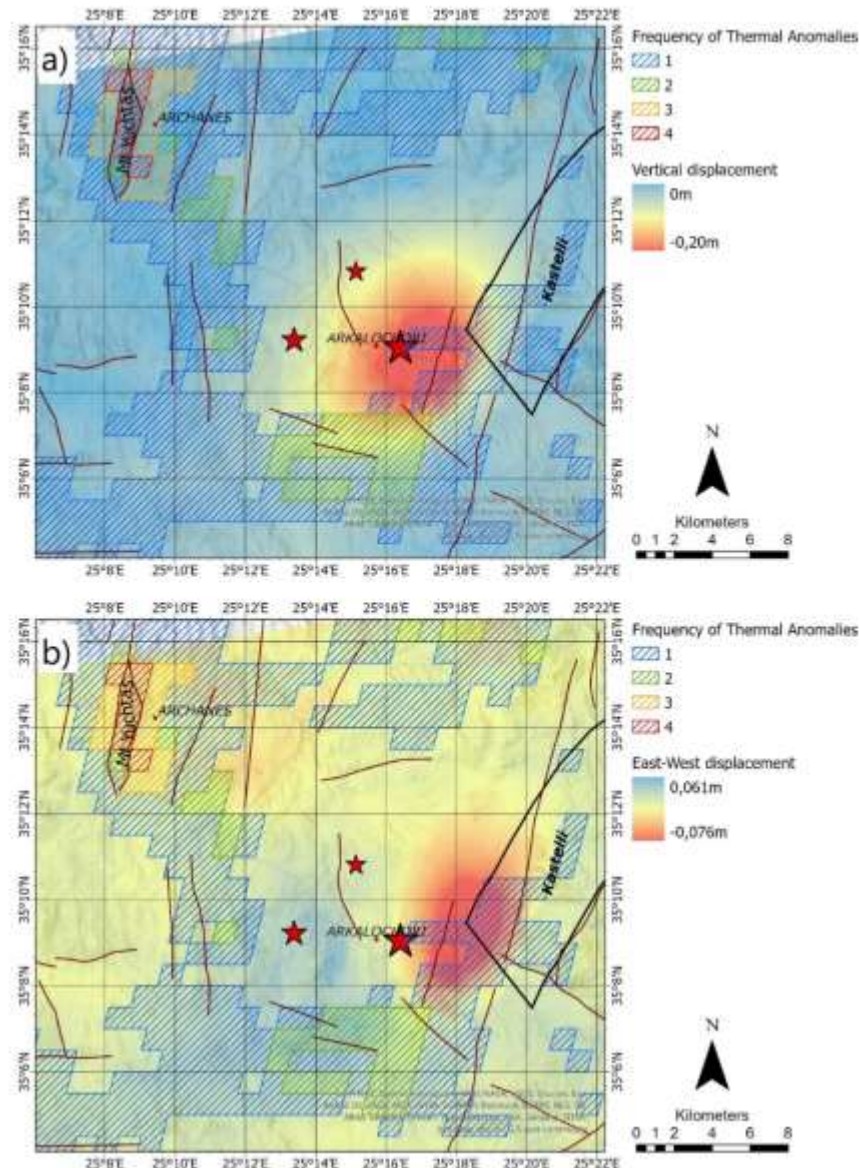


**Figure 8.** Displacement maps for: (a) the vertical (up–down); and (b) the E–W direction for the Central Crete earthquake overlain by the thermal anomaly frequency map.

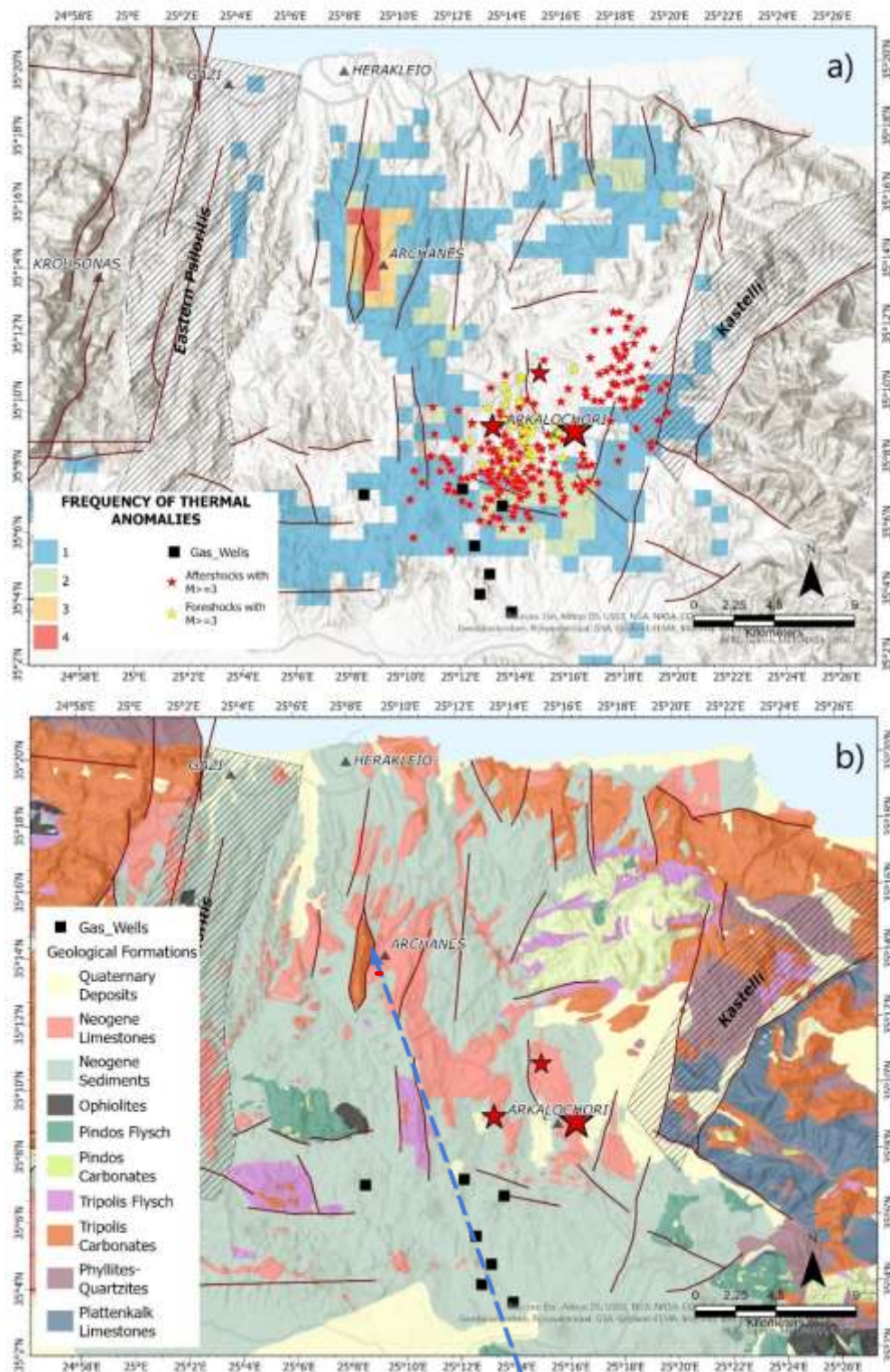


**Figure 9.** (a) Frequency of thermal anomalies combined with the wells that encountered gas, the active faults and the strongest earthquakes; and (b) the lithological map of the study area [54] showing the extended Neogene sediments and the proposed route followed by the gases before being released in the vicinity of Mount Youchtas.

Further analysis of the proposed mechanism could help in understanding the earthquake preparation process and may indicate a hopeful pathway of research. The RST technique in combination with InSAR images and geological data can play a very important role in this direction. In conclusion, the present work is an attempt that will increase

the scientific effort to define earthquake forerunners, and its future fusion with other state-of-the-art methods (e.g., [5]) will support our knowledge for earthquake preparatory processes. An alternative explanation which could be active in parallel with that proposed above is based on the activation of electrical charges (electrons and positive holes) in rocks by the activation of peroxy defects during the increasing of tectonic stresses prior to any major seismic activity [60]. The positive holes are able to flow out of the stressed rock volume through the surrounding unstressed rock traveling fast, while electrons remain trapped locally [61]. The presence of hole charge carriers that form a surface charge layer could be an alternative explanation since when holes accumulate in the surface or near surface structure, they can recombine and return to the self-trapped positive hole pair from which they exited before their stress activation at depth. Furthermore, laboratory experiments till failure on a constant rated load anorthosite sample (a nominally monomineralic feldspar rock) suggests an IR emission that appears and disappears as the stress build-up progresses, interpreted as a hole pair recombination process ([60,61] and references therein).

The hypothesis of thermal anomalies due to the release of gases is suggested for the Central Crete earthquake sequence, and it is reinforced by the recent report of the presence of biogenic gases in water wells in the Messara basin [62] and the broader Arkalochori area as well [63] (Figure 9). The extended thick Neogene sediments are suggested as the host of the gas whose migration follows the general dip direction of the Miocene strata and the faults charging the sediments located several kilometers away to the NNW of the basin depocenter. This could explain the intense and persistent thermal anomalies on Mount Yuchtas. Given the fact that the Neogene sediments are extremely extended in the study area, with the western and the eastern parts of the Messara basin exhibiting the greatest depths, while the central part is significantly more elevated, one could similarly explain the existence of thermal anomalies southeast of Arkalochori and the absence of the phenomenon to the north and northeast of Arkalochori (Figure 9). The continuously increasing stress during the preseismic phase resulted to an increase in degassing activity. As the stress evolution creates a network of micro- and meso-scaled cracks that superimposed to the already existing faulting system, a pathway is created that supports the discharge of trapped gas buffers. As the earthquake approaches, due to the creation of a significant fracture in the rupture zone, a new rise in degassing activity can occur before normality is gradually restored [20]. The absence of thermal anomalies during October could indicate that after the earthquake occurrence, the stress field relaxed ([64] and references therein) and thus reduced the above-described processes. A crucial note is that the appearance of thermal anomalies was in the time period where the system presented critical dynamics [25].

## References

1. Ouzounov, D.; Pulinet, S.; Hattori, K.; Taylor, P. Pre-Earthquake Processes: A Multidisciplinary Approach to Earthquake Prediction Studies. In *Geophysical Monograph Series*; John Wiley & Sons Inc.: Hoboken, NJ, USA, 2018; 365p.
2. Genzano, N.; Filizzola, C.; Lisi, M.; Pergola, N.; Tramutoli, V. Toward the development of a multi parametric system for a short-term assessment of the seismic hazard in Italy. *Ann. Geophys.* **2020**, *63*, PA550.
3. Picozza, P.; Conti, L. Looking for earthquake precursors from space: A critical review. *Front. Earth Sci.* **2021**, *9*, 578.
4. Tramutoli, V.; Aliano, C.; Corrado, R.; Filizzola, C.; Genzano, N.; Lisi, M.; Martinelli, G.; Pergola, N. On the possible origin of thermal infrared radiation (TIR) anomalies in earthquake-prone areas observed using robust satellite techniques (RST). *Chem. Geol.* **2013**, *339*, 157–168.
5. De Santis, A.; Marchetti, D.; Pavón-Carrasco, F.J.; Cianchini, G.; Perrone, L.; Abbattista, C.; Alfonsi, L.; Amoroso, L.; Campuzano, S.A.; Carbone, M.; et al. Precursory worldwide signatures of earthquake occurrences on Swarm satellite data. *Sci. Rep.* **2019**, *9*, 20287 <https://doi.org/10.1038/s41598-019-56599-1>.
6. Li, Z.L.; Tang, B.H.; Wu, H.; Ren, H.; Yan, G.; Wan, Z.; Sobrino, J.A. Satellite-derived land surface temperature: Current status and perspectives. *Remote Sens. Environ.* **2013**, *131*, 14–37.
7. Lillesand, T.M.; Kiefer, R.W.; Chipman, J.W. *Remote Sensing and Image Interpretation*; John Wiley & Sons: Hoboken, NJ, USA, 1987.
8. Anderson, M.C.; Allen, R.G.; Morse, A.; Kustas, W.P. Use of Landsat thermal imagery in monitoring evapotranspiration and managing water resources. *Remote Sens. Environ.* **2012**, *122*, 50–65.
9. Vollmer, M.; Möllmann, K.P. *Infrared Thermal Imaging: Fundamentals, Research and Applications*, 2nd ed.; John Wiley & Sons: Hoboken, NJ, USA, 2017, ISBN: 978-3-527-41351-5.
10. Anderson, M.; Kustas, W. Thermal remote sensing of drought and evapotranspiration. *EOS Trans. Am. Geophys. Un.* **2008**, *89*, 233–234.
11. Kustas, W.; Anderson, M. Advances in thermal infrared remote sensing for land surface modeling. *Agric. Forest Meteorol.* **2009**, *149*, 2071–2081.
12. Karnieli, A.; Agam, N.; Pinker, R.T.; Anderson, M.; Imhoff, M.L.; Gutman, G.G.; Panof, N.; Goldberg, A. Use of NDVI and land surface temperature for drought assessment: Merits and limitations. *J. Clim.* **2010**, *23*, 618–633.
13. Ganas, A.; Lagios, E.; Petropoulos, G. and Psiloglou, B. Thermal imaging of Nisyros volcano (Aegean Sea) using ASTER data: Estimation of radiative heat flux. *Int. J. Remote Sens.* **2010**, *31*, 4033–4047.

14. Keramitsoglou, I.; Kiranoudis, C.T.; Ceriola, G.; Weng, Q.; Rajasekar, U. Identification and analysis of urban surface temperature patterns in Greater Athens, Greece, using MODIS imagery. *Remote Sens. Environ.* **2011**, *115*, 3080–3090. <https://doi.org/10.1016/j.rse.2011.06.014>.
15. Christman, Z.; Rogan, J.; Eastman, J.R.; Turner, B.L. Distinguishing Land Change from Natural Variability and Uncertainty in Central Mexico with MODIS EVI, TRMM Precipitation, and MODIS LST Data. *Remote Sens.* **2008**, *8*, 478 <https://doi.org/10.3390/rs8060478>.
16. Scambos, T.A.; Campbell, G.G.; Pope, A.; Haran, T.; Muto, A.; Lazzara, M.; Reijmer, C.H.; van den Broeke, M.R. Ultralow surface temperatures in East Antarctica from satellite thermal infrared mapping: The coldest places. *Earth Geophys. Res. Lett.* **2018**, *45*, 6124–6133.
17. Aguilar-Lome, J.; Espinoza-Villar, R.; Espinoza, J.C.; Rojas-Acuña, J.; Willems, B.L.; Leyva-Molina, W.M. Elevation-dependent warming of land surface temperatures in the Andes assessed using MODIS LST time series (2000–2017). *Int. J. Appl. Earth Obs.* **2018**, *77*, 119–128.
18. Peleli, S.; Kouli, M.; Marchese, F.; Lacava, T.; Vallianatos, F.; Tramutoli, V. Monitoring temporal variations in the geothermal activity of Miocene Lesvos volcanic field using remote sensing techniques and MODIS—LST imagery. *Int. J. Appl. Earth Obs. Geoinf.* **2021**, *95*, 102251. <https://doi.org/10.1016/j.jag.2020.102251>.
19. Kouli, M.; Peleli, S.; Saltas, V.; Makris, J.P.; Vallianatos, F. Robust Satellite Techniques for mapping thermal anomalies possibly related to seismic activity of March 2021, Thessaly Earthquakes. *Bull. Geol. Soc. Greece* **2021**, *58*, 105–130. <https://doi.org/10.12681/bgsg.27058>.
20. Filizzola, C.; Corrado, A.; Genzano, N.; Lisi, M.; Pergola, N.; Colonna, R.; Tramutoli, V. RST Analysis of Anomalous TIR Sequences in Relation with Earthquakes Occurred in Turkey in the Period 2004–2015. *Remote Sens.* **2022**, *14*, 381. <https://doi.org/10.3390/rs14020381>.
21. Triantafyllou, I.; Karavias, A.; Koukouvelas, I.; Papadopoulos, G.A.; Parcharidis, I. The Crete Isl. (Greece) Mw6.0 Earthquake of 27 September 2021: Expecting the Unexpected. *Geo. Hazards* **2022**, *3*, 6.
22. Vassilakis, E.; Kaviris, G.; Kapetanidis, V.; Papageorgiou, E.; Fomelis, M.; Konsolaki, A.; Petrakis, S.; Evangelidis, C.P.; Alexopoulos, J.; Karastathis, V. The 27 September 2021 Earthquake in Central Crete (Greece)—Detailed Analysis of the Earthquake Sequence and Indications for Contemporary Arc-Parallel Extension to the Hellenic Arc. *Appl. Sci.* **2022**, *12*, 2815.
23. Caputo, R.; Catalano, S.; Monaco, C.; Romagnoli, G.; Tortorici, G.; Tortorici, L. Active faulting on the island of Crete (Greece). *Geophys. J. Int.* **2010**, *183*, 111–126. <https://doi.org/10.1111/j.1365-510246X.2010.04749.x>.
24. Karakonstantis, A.; Pavlou, K.; Kouli, M.; Michas, G.; Avgerinou, S.E.; Anyfadi, E.A.; Chatzopoulos, G.; Hloupis, G.; Makris, J.P.; Vallianatos, F. Preliminary results of the 2021–2022 central Crete seismic sequences: Seismological, Satellite and Geophysical observations. In Proceedings of the 3rd European Conference on Earthquake Engineering & Seismology, Bucharest, Romania, 4–9 September 2022.
25. Vallianatos, F.; Michas, G.; Hloupis, G.; Chatzopoulos, G. The Evolution of Preseismic Patterns Related to the Central Crete (Mw6.0) Strong Earthquake on 27 September 2021 Revealed by Multiresolution Wavelets and Natural Time Analysis. *Geosciences* **2022**, *12*, 33. <https://doi.org/10.3390/geosciences12010033>.
26. Hellenic Unified Seismic Network (H.U.S.N.). Available online: <http://www.gein.noa.gr/en/networks/husn> (accessed on 1 November 2021).
27. Tramutoli, V.; Di Bello, G.; Pergola, N.; Piscitelli, S. Robust satellite techniques for remote sensing of seismically active areas. *Ann. di Geofis.* **2001**, *44*, 295–312 <https://doi.org/10.4401/ag-3596>.
28. Tramutoli, V.; Cuomo, V.; Filizzola, C.; Pergola, N.; Pietrapertosa, C. Assessing the potential of thermal infrared satellite surveys for monitoring seismically active areas: The case of Kocaeli (Izmit) earthquake, August 17, 1999. *Remote Sens. Environ.* **2005**, *96*, 409–426 <https://doi.org/10.1016/j.rse.2005.04.006>.
29. Tramutoli, V. Robust Satellite Techniques (RST) for Natural and Environmental Hazards Monitoring and Mitigation: Theory and Applications. In Proceedings of the 2007 International Workshop on the Analysis of Multi-Temporal Remote Sensing Images, Leuven, Belgium, 18–20 July 2007, pp. 1–6. <https://doi.org/10.1109/MULTITEMP.2007.4293057>.
30. Curlander, J.; McDonough, R. *Synthetic Aperture Radar: Systems and Signal Processing*; John Wiley & Sons: Hoboken, NJ, USA, 1991; ISBN 978-0-471-85770-9.
31. Hooper, A.; Bekaert, D.; Spaans, K.; Arikan, M. Recent advances in SAR interferometry time series analysis for measuring crustal deformation. *Tectonophysics* **2012**, *514–517*, 1–13.
32. Massonnet, D.; Rabaute, T. Radar interferometry: Limits and potential. *IEEE Geosci. Remote Sens.* **1993**, *31*, 455–464. <https://doi.org/10.1109/36.214922>.
33. Bamler, R.; Hartl, P. Synthetic aperture radar interferometry. *Inverse. Prob.* **1998**, *14*, 1–54.
34. Elliott, J.; Walters, R.; Wright, T. The role of space-based observation in understanding and responding to active tectonics and earthquakes. *Nat. Commun.* **2016**, *7*, 13844.
35. Markogiannaki, O.; Karavias, A.; Bafi, D.; Angelou, D.; Parcharidis, I. A geospatial intelligence application to support post-disaster inspections based on local exposure information and on coseismic DInSAR results: The case of the Durres (Albania) earthquake on November 26, 2019. *Nat. Hazards* **2020**, *103*, 3085–3100.
36. McKenzie, D. Active tectonics of the Mediterranean region. *Geophys. J. Roy. Astr. Soc.* **1972**, *30*, 109–185.
37. McKenzie, D. Active tectonics of the Alpine–Himalayan belt: The Aegean Sea and surrounding regions. *Geophys. J. Roy. Astr. Soc.* **1978**, *55*, 217–254.
38. Le Pichon, X.; Angelier, J. The Hellenic arc and trench system: A key to the neotectonic evolution of the Eastern Mediterranean area. *Tectonophysics* **1979**, *60*, 1–42.
39. Kassaras, I.; Kapetanidis, V.; Ganas, A.; Tzanis, A.; Kosma, C.; Karakonstantis, A.; Valkaniotis, S.; Chailas, S.; Kouskouna, V.; Papadimitriou, P. The New Seismotectonic Atlas of Greece (v1.0) and Its Implementation. *Geosciences* **2020**, *10*, 447.

40. Ganas, A.; Oikonomou, I.; Tsimi, C. NOA faults: A digital database for active faults in Greece. *Bull. Geol. Soc. Greece* **2013**, *47*, 518–530. <https://doi.org/10.12681/bgsg.11079>.
41. Caputo, R.; Pavlides, S. The Greek Database of Seismogenic Sources (GreDaSS), version 2.0.0: A Compilation of Potential Seismogenic Sources (Mw > 5.5) in the Aegean Region. 2013. Available online: <https://gredass.unife.it>. <https://doi.org/10.15160/unife/gredass/0200>.
42. Kokinou, E.; Moisiou, M.; Tsanaki, I.; Tsakalaki, E.; Sarris, A. and Vallianatos, F. A seismotectonic study for the Heraklion basin in Crete (Southern Hellenic arc, Greece). *Int. J. Geol.* **2008**, *2*, 9–16.
43. van Hinsbergen, D.J.J.; Meulenkamp, J.E. Neogene supradetachment basin development on Crete (Greece) during exhumation of the South Aegean core complex. *Basin Res.* **2006**, *18*, 103–124.
44. Filizzola, C.; Pergola, N.; Pietrapertosa, C.; Tramutoli, V. Robust satellite techniques for seismically active areas monitoring: A sensitivity analysis on September 7, 1999 Athens's earthquake. *Phys. Chem. Earth* **2004**, *29*, 517–527. <https://doi.org/10.1016/j.pce.2003.11.019>.
45. Eleftheriou, A.; Filizzola, C.; Genzano, N.; Lacava, T.; Lisi, M.; Paciello, R.; Pergola, N.; Vallianatos, F.; Tramutoli, V. Long-term RST analysis of anomalous TIR sequences in relation with earthquakes occurred in Greece in the period 2004–2013. *Pure Appl. Geophys.* **2016**, *173*, 285–303. <https://doi.org/10.1007/s00024-015-1116-8>.
46. Pergola, N.; Aliano, C.; Coviello, I.; Filizzola, C.; Genzano, N.; Lacava, T.; Lisi, M.; Mazzeo, G.; Tramutoli, V. Using RST approach and EOS-MODIS radiances for monitoring seismically active regions: A study on the 6 April 2009 Abruzzo earthquake. *Nat. Hazards Earth Syst. Sci.* **2010**, *10*, 239–249.
47. Wan, Z. MODIS Land Surface Temperature Products User's Guide. 2013. Available online: <https://ices.eri.ucsb.edu/modis/LstUsrGuide/usrguide.html>.
48. Aliano, C.; Corrado, R.; Filizzola, C.; Genzano, N.; Pergola, N.; Tramutoli, V. Robust TIR satellite techniques for monitoring earthquake active regions: Limits, main achievements and perspectives. *Ann. Geophys.* **2008**, *51*, 303–317 <https://doi.org/10.4401/ag-3050>.
49. Aliano, C.; Corrado, R.; Filizzola, C.; Genzano, N.; Pergola, N.; Tramutoli, V. Robust satellite techniques (RST) for the thermal monitoring of earthquake prone areas: The case of Umbria-Marche October, 1997 seismic events. *Ann. Geophys.* **2008**, *51*, 451–459.
50. ESA Sentinel Online—Sentinel-1. Available online: <https://sentinel.esa.int/web/sentinel/missions/sentinel-1> (accessed on 20 April 2020).
51. Goldstein, R.M.; Werner, C.L. Radar interferogram filtering for geophysical applications. *Geophys. Res. Lett.* **1998**, *25*, 4035–4038.
52. Silverman, B.W. *Density Estimation for Statistics and Data Analysis*; Chapman and Hall: New York, NY, USA, 1986.
53. Ganas, A.; Hamiel, Y.; Serpetsidaki, A.; Briole, P.; Valkaniotis, S.; Fassoulas, C.; Piatibratova, O.; Kranis, H.; Tsironi, V.; Karamitros, I.; et al. The Arkalochori Mw = 5.9 Earthquake of 27 September 2021 Inside the Heraklion Basin: A Shallow, Blind Rupture Event Highlighting the Orthogonal Extension of Central Crete. *Geosciences* **2022**, *12*, 220. <https://doi.org/10.3390/geosciences12060220>.
54. Institute of Geology and Mineral Exploration—IGME. *Geological Map of Greece—Mochos Sheet (Scale 1:50.000)*; IGME: Athens, Greece, 1989.
55. Pulinet, S.; Ouzounov, D. Lithosphere–atmosphere–ionosphere coupling (LAIC) model—an unified concept for earthquake precursors validation. *J. Asian Earth Sci.* **2011**, *41*, 371–82. <https://doi.org/10.1016/j.jseas.2010.03.005>.
56. Thomas, D. Geochemical Precursors to Seismic Activity. *Pure Appl. Geophys.* **1988**, *126*, 241–266. <https://doi.org/10.1007/BF00878998>.
57. Martinelli, G. Previous, Current, and Future Trends in Research into Earthquake Precursors in Geofluids. *Geosciences* **2020**, *10*, 189. <https://doi.org/10.3390/geosciences10050189>.
58. Chiodini, G.; Cardellini, C.; Di Luccio, F.; Selva, J.; Frondini, F.; Caliro, S.; Rosiello, A.; Beddini, G.; Ventura, G. Correlation between tectonic CO<sub>2</sub> Earth degassing and seismicity is revealed by a 10-year record in the Apennines, Italy. *Sci. Adv.* **2020**, *6*, 35. <https://doi.org/10.1126/sciadv.abc2938>.
59. Tamburello, G.; Pondrelli, S.; Chiodini, G.; Rouwet, D. Global-scale control of extensional tectonics on CO<sub>2</sub> earth degassing. *Nat. Commun.* **2018**, *9*, 4608. <https://doi.org/10.1038/s41467-018-07087-z>.
60. Freund, F.T. Pre-earthquake signals: Underlying physical processes. *J. Southeast. Asian Earth Sci.* **2011**, *41*, 383–400. <https://doi.org/10.1016/j.jseas.2010.03.009>.
61. Freund, F.; Ouillon, G.; Scoville, J.; Sornette, D. Earthquake precursors in the light of peroxy defects theory: Critical review of systematic observations. *Eur. Phys. J. Spéc. Top.* **2021**, *230*, 7–46. <https://doi.org/10.1140/epjst/e2020-000243-x>.
62. Panagopoulos, G.; Vafidis, A.; Soupios, P. and Manoutsoglou, E. A study on the Gas-bearing Miocene Sediments of MESSARA Basin in Crete (Greece) by Using Seismic Reflection, Geochemical and Petrophysical Data. *Arab. J. Sci. Eng.* **2022**, <https://doi.org/10.1007/s13369-022-06727-3>.
63. Panagopoulos, G.; Pylotis, I.; Zelilidis, A.; Spyridonos, E.; Hamdan, H.; Vafidis, A.; Manoutsoglou, E. 3D modeling of biogenic gas-bearing Neogene deposits at Arkalochori region, Messara, Crete, Greece. *Proc. IAMG Saltzburg.* **2011**, 431–440.
64. Vallianatos, F.; Sakkas, V. Multiscale Post-Seismic Deformation Based on cGNSS Time Series Following the 2015 Lefkas (W. Greece) Mw6.5 Earthquake. *Appl. Sci.* **2021**, *11*, 4817. <https://doi.org/10.3390/app11114817>.



## Chapter 4

Preliminary results of the 2021-2022  
Central Crete Seismic Sequences:  
Seismic,  
Satellite and Geophysical Observations

**Abstract:** The 27 September 2021 damaging mainshock ( $M_w$ 6.0) with a seismic moment  $M_0$  of  $1.14 \times 10^{18}$  N·m is the first known strong earthquake that ruptured the Central Crete (Greece) close to Arkalochori village, during the last hundred years. The main shock was preceded by foreshock activity lasting for about four months. In this work, we present the results from the analysis of the earthquake sequence and the aftershock sequence as reported until October 31, 2021. The coseismic maximum ground subsidence of about 18 cm was estimated from InSAR images, taking into account that the observed deformation may have included that caused by the largest aftershock ( $M_w$ 5.1) of 28 September 2021. The deformation is in agreement with the spatial distribution of aftershocks and the Coulomb stress changes. The entire aftershock epicenters located in an almost SW-NE direction but are distributed in two main clusters, the southern and the northern ones. The analysis of the inter-event times distribution in the foreshock and aftershock period and for both clusters based on non-extensive statistical physics indicates a system in an anomalous equilibrium.

---

## 1. Introduction

The study area is situated in Central Crete, near the front of the Hellenic arc where the European and Nubia plates converge, giving rise to large earthquakes (Delibasis et al., 1981; Papadopoulos 2011; 2017; Ganas and Parsons, 2009). The 2021 seismic crisis in Arkalochorion and the neighboring villages was located in a fault system of what was considered as possibly-active with NW-SE and NE-SW direction of strike (e.g. Fassoulas, 2001; Kokinou et al., 2008; Caputo et al., 2010; Zygouri et al., 2016; Triantafyllou et al., 2022; Vassilakis et al., 2022 and references there in), which bounds the Heraklion basin.

In this area close to Arkalochorion village, a strong earthquake of magnitude  $M_w=6.0$  occurred on September 27, 2021, 06:17:22 UTC, with a focal depth of 9.6 km. The earthquake caused extensive damages in Arkalochorion, Rousochoria, Archontiko and Patsideros villages, causing severe damages in more than 5,000 old buildings on the island according to news reports.

## 2. Spatiotemporal patterns of the Earthquake sequence

The Arkalochorion earthquake sequence is divided into two main temporal groups, one that preceded the September 27<sup>th</sup>  $M_w=6.0$  mainshock consisting of 620 events with a significant rise in numbers during July and August 2021 (Vallianatos et al., 2022) and the aftershock sequence, divided into three spatial sub-groups. A major part of the sequence was recorded by local stations of the regional Hellenic Unified Seismological Network (HUSN), with the nearest stations being KNSS, PFKS of the Hellenic Seismological Network of Crete (HSNC), located about 20 km to the SW and NE of the epicenter, respectively. On October 1, 2021 the Geodynamics Institute (National Observatory of Athens-NOA) installed 4 temporary stations (CRE1-4) around the aftershock zone, improving the depth accuracy and providing a better preliminary hypocentral solution for this time period. A total of 2,599 events of the 2021 Arkalochorion sequence that occurred during the period between 13 January and 31 October 2021 (Figure 1) were detected and manually analysed using real-time waveform data from the Hellenic Unified Seismological network (HUSN, <https://eida.gein.noa.gr/>), as well as the stations of Hellenic Seismological Network of Crete (HSNC) and of Geodynamic Institute (NOA) that operate in the area. Accurate earthquake hypocenter parameters are required to obtain a detailed image of the structure properties and processes that trigger seismic activity. HYPODD is an algorithm that minimizes residuals between observed and calculated travel time differences for pairs of neighboring earthquakes at each station that recorded both events. In this way errors caused by unmodeled velocity structure are minimized without the use of station corrections. A minimum 1-D layered velocity model is used to predict

the travel time differences and partial derivatives. Inter-event distance and misfit weighting is applied after each iteration to catalogue data, to optimize their quality dynamically during relocation. Horizontal and vertical relative spatial errors can be minimized by approximately one order of magnitude under certain conditions (Waldhauser 2001).

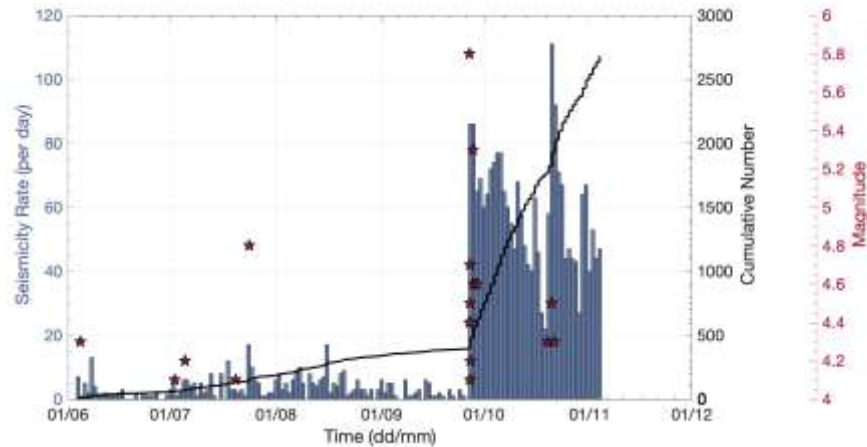


**Fig. 1** Seismicity rate in terms of events per day (blue vertical bars) and cumulative number of events (solid black line) during June 2021–October 2021 in the area of Arkalochorion. The occurrence of events with  $M_L \geq 4$  is marked by red stars ( $M_L$  magnitude in the red axis to the right).

In this study, two local 1-D velocity models (Delibassis et al., 1999; Becker et al., 2010) have been used through data processing, running the HypoInverse code (Klein, 2002). Residual values from these models were compared (Table 1) with no significant differences, while the epicentral differences were less than 0.5 km. Depths were more sensitive to the velocity model, differing by about 1 km on average. The Delibassis et al. (1999) velocity model (Model 1) provided much shallower events than the respective ones from the velocity model of Becker et al. (2010) (Model 2), particularly for the stronger events of the sequence ( $M=6.0$  and  $M=5.3$ ) that were located at depths shallower than 5 km (2.7 and 0.7 km respectively), which seemed unrealistic in terms of earthquake physics and the geology of the area. The final hypocentral locations were obtained using the local velocity model of Becker et al. (2010). Focal depths are mainly distributed in the range of 5 – 15 km for the aftershocks of the September 27<sup>th</sup>  $M_w=6.0$  event.

**Table 1.** Statistics of the 2021 Arkalochorion earthquake sequence

Model	Model used	
	Model 1	Model 2
Mean RMS (sec)	0.26	0.26
Mean ERH (km)	1.30	1.31
Mean ERZ (km)	4.41	4.52
Mean Depth (km)	9.43	13.94

The time evolution of seismic sequence was divided into 4 sub-groups (Figure 2):

1. 13 January – 27 September 2021 (period A), consisting of 620 events,
2. 27 September – 28 September 2021 (period B), first day of the aftershock sequence and just few hours before the greatest aftershock ( $M5.3$ ), composed by 90 events,

3. 28 September – 12 October 2021 (period C), just after the occurrence of the M=5.3 aftershock at 04:48 UTC, and it consists of 803 events,
4. 12 October – 31 October 2021 (period D), where the M=4.0 event took place after a significant decay in numbers of the aftershocks in Arkalochorion.

In the area of Central Crete, 2497 out of 2581 events of the initial catalogue were relocated with HYPODD, giving a first result that could be rated as satisfactory. The mean temporal errors (rms) were reduced from 0.17 sec to 0.12 sec while the spatial errors (erx, ery, erz) were decreased from 1.1, 1.2 and 1.9 km to 0.3, 0.3 and 0.4 km respectively. The hypoDD-estimated errors in the final locations were calculated using the LSQR method, which may not be representative of the real ones (Waldhauser, 2001).

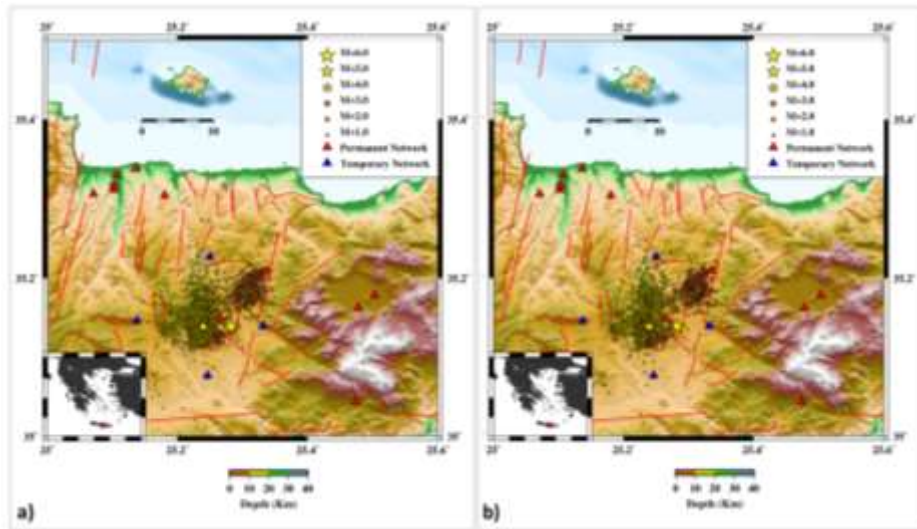


**Fig. 2**–Located (left) and relocated (right) epicentres of the 2021 Arkalochorion earthquake sequence.

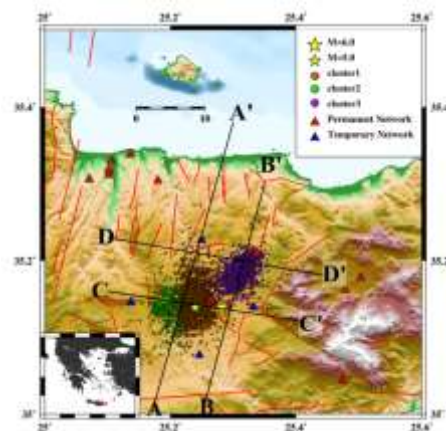


**Fig. 3**–Location of the performed cross-sections

The epicenter of the mainshock was located less than 3 km to the SE of Arkalochorion (lat: 35.1416° N, long: 25.2736° E) at a depth of 9.6 km, obtained by the double-difference algorithm procedure. The optimization of the final results leads to clustering of the earthquake sequence into four main clusters. A dense cluster of events has occurred west of the mainshock, in an approximately 15-km-long area associated with the foreshocks (cluster 1). The epicenters of cluster 2 were mainly distributed in the area between Amourgeles and Parthenio N-S oriented

normal faults, in the region to the west of Arkalochorion. Further to the NE, another significant cluster of events (cluster 3) was also observed, in the footwall of Agnos NE-SW striking normal fault, near Kastelli (Figure 3).

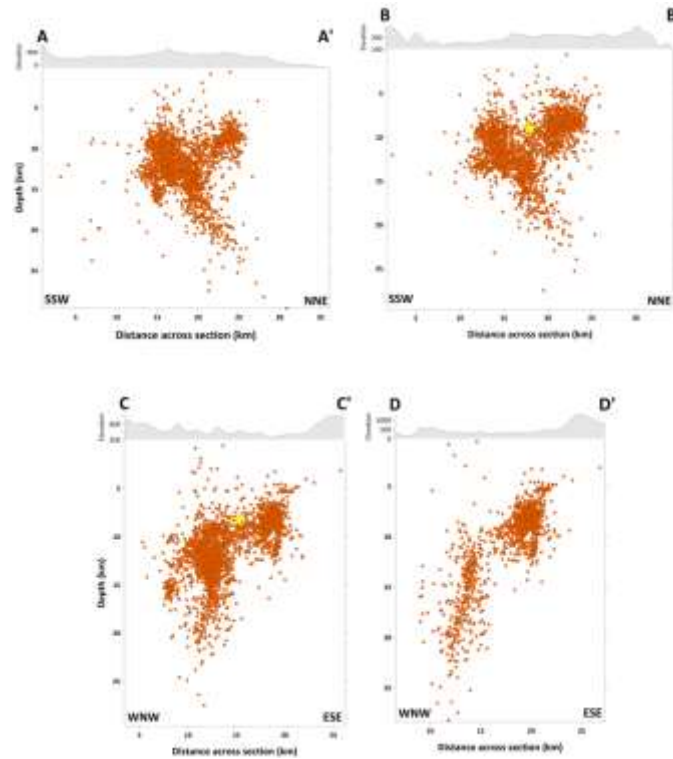


**Fig. 4**–Hypocenter distribution in the performed four sections

Most events are in a range of focal depths between 7 and 18 km. Furthermore, four (4) cross-sections were created in order to see the impact of the relocation procedure on the sequence hypocentral depths and the discrimination of the local activated structures (Figure 4). Cross-sections 1-2 have a NNE-SSW orientation, and 3-4 WNW-ESE direction, perpendicular to the NE trending faults. The geometry of the hypocenters as they appear in the performed cross-sections (Figure 4), reveal the activation of a fault, dipping  $\sim 60^\circ$  to the WNW, and a smaller antithetic structure, possibly connected to Galatas N-S striking normal fault. An almost sub-vertical structure makes an appearance in the cross-sections north of the epicenter of the mainshock (sections B-B', D-D'; Figures 4).

### 3. Coulomb stress changes

Numerous studies of strong earthquakes show a correlation between the positive lobe of Coulomb stress changes and the locations of most and major aftershocks (see King et al., 1994). Here, we examine the co-seismic static stress changes with respect to the aftershocks spatial distribution during the  $M_w=6.0$  main event. The  $\Delta CFS$  changes were determined via Coulomb3.3 software (Toda et al., 2011) in an elastic half-space and a uniform slip on the rupture planar surfaces. The Coulomb Failure Stress changes ( $\Delta CFS$ ) are given by the equation (1):

$$\Delta CFS = \Delta\tau - \mu_f \Delta\sigma \quad (1)$$

Where  $\Delta\tau$  and  $\Delta\sigma$  are the in-shear stress and normal stress respectively, while  $\mu_f$  is the effective friction coefficient (Cocco & Rice, 2002). For the shear modulus and Poisson's ratio, we used the values of 3.3 MPa and 0.25, respectively, and a mean value for the coefficient of friction equal to  $\mu_f= 0.4$  (Harris & Simpson, 1998). To calculate the

subsurface fault's width and length, we used the empirical relations of Wells and Coppersmith (1994) for each modelled earthquake. The parameters used for the estimation of  $\Delta CFS$  are: depth 9 km, strike 214°, dip 52°, rake 95° and length and width 2.3 km and 2.56 km, respectively. The results for the  $\Delta CFS$  are presented in Figure 5.

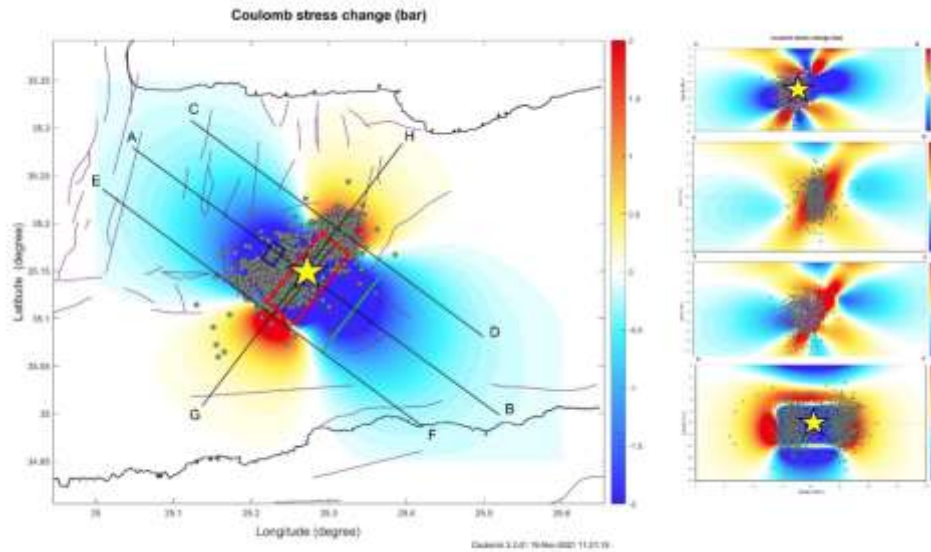
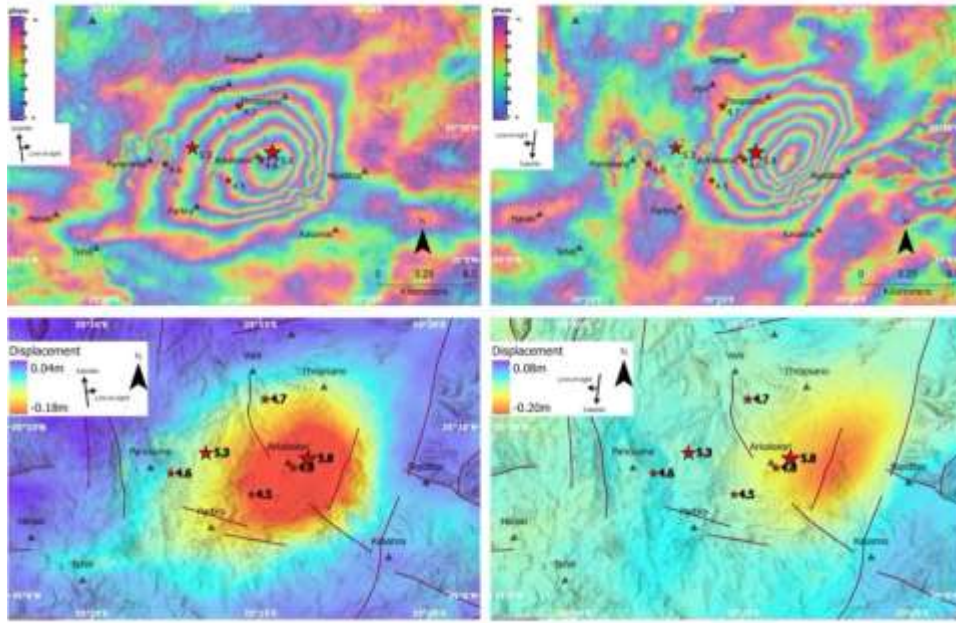


Fig. 5 - Coulomb stress changes distribution due to Mw=6.0 event (yellow star) at centroid depth of 8 km. (Right) Coulomb stress changes along the vertical cross-sections AB, CD, EF and the parallel cross-section GH (from up to down). The green circles are the relocated hypocenters of the aftershocks which occurred after the Mw=6.0 main shock.

#### 4. Ground Deformation from InSAR

The InSAR technique has proven to be an efficient tool for measuring and observing ground deformation related to geodynamic processes (see Elliott et al., 2016). To map the coseismic ground deformation due to the September 27, 2021 earthquake, we used one ascending and one descending SAR image pair (with acquisition dates of 23 September 2021 – 29 September 2021 and 25 September 2021– 01 October 2021, respectively) from ESA's Sentinel-1A and Sentinel-1B satellites (<https://scihub.copernicus.eu/>). In both cases the master image was the one before the earthquake occurrence, while the slave image the one that refers to the date after the event. Each master-slave pair was processed using the SNAP software and two individual interferograms were generated. Topographic phase was subtracted using the SRTM 1 arc-second Digital Terrain Model, a 30-m resolution Shuttle Radar Topography Mission Digital Elevation Model (USGS 1 ARC-second SRTM DEM), while the signal tonoise ratio was enhanced by applying the adaptive power spectrum filter of Goldstein and Werner (1998) with a coherence threshold of 0.4. The two wrapped interferograms were then used in the second stage to calculate the terrain displacement, an unwrapping process was performed, and the phase unit was transformed into distance units in the satellite line of sight (LoS) for every interferometric pair. As a last step and in order to map the vertical (up-down) and horizontal (east-west) deformation, displacement decomposition of ascending and descending LOS displacement products was performed. Subsidence up to 20 cm has been calculated from the displacement decomposition in the vertical (up-down) direction while no uplift displacement was detected. As shown in Figure 6, the horizontal (east-west) displacement maps an eastward movement up to 6 cm to the west of Arkalochorion town and a westward movement up to 8 cm to the east of Arkalochorion was detected.



**Fig. 6** - Up: Wrapped ascending (left) and descending (right) co-seismic interferograms over the Arkalochorion area. The interferograms are draped over shaded relief. **Down:** Co-seismic displacement maps generated using the ascending and the descending image pairs and draped over shaded relief. The active faults of the area are depicted with lines while red stars show the major event and aftershocks.

## 5. The interevent time distribution of the Arkalochorion sequence

To examine the temporal characteristics and scaling relations of the Arkalochorion sequence, we used the non-extensive statistical physics (NESP) concept, and the  $q$  entropic parameters were calculated. It has been demonstrated that the cumulative distribution of the spatiotemporal properties, such as the interevent times  $\tau$ , which is the time interval between two consecutive events, can be explained by non-extensive statistical physics (Michas et al., 2013; Papadakis et al., 2013). In a non-equilibrium system, the complexity states can be studied by the entropic functional (Tsallis 2009)  $S_q = k_B \frac{1 - \int_0^\infty P^q(X) dX}{q-1}$ , where  $k_B$  is Boltzmann's constant,  $q$  expresses the degree of non-additivity and  $p(X)$  represents the probability distribution of the parameter  $X$ . Using the Lagrange multipliers method under proper normalized constraints (Tsallis, 2009; Chelidze et al., 2018), the entropy  $S_q$  can be maximized to find the probability distribution and then the cumulative distribution function (CDF) of the interevent times  $P(>\tau) = N(>\tau)/N_o$ , with  $N(>\tau)$  the number of interevent times with value greater than  $\tau$  and  $N_o$  the total number of events (Vallianatos et al., 2016a; 2016b; 2018).

The cumulative distribution function is given as  $P(>\tau) = \exp_q(-\frac{\tau}{\tau_o})$ , where  $\tau_o$  is a generalized scaled interevent time and  $\exp_q(x)$  the  $q$ -exponential function defined as:  $\exp_q(x) = [1 + (1 - q)x]^{1/(1-q)}$ . Its inverse is the  $q$ -logarithmic function:  $\ln_q(x) = \frac{1}{1-q} (x^{1-q} - 1)$ . In the limit of  $q \rightarrow 1$ , the  $q$ -exponential and  $q$ -logarithmic functions lead to the ordinary exponential and logarithmic functions, respectively. In Fig 7, the interevent time distributions during the foreshock and aftershock periods and the two spatial clusters are presented along with the CDF based on the NESP approach. The analysis shows that the  $q$ -exponential function describes appropriately the observed CDF, with  $q$ -values that vary from  $q_\tau=1.38$  for the NNE cluster, to  $q_\tau=1.71$  for the foreshock sequence and  $q_\tau=1.84$  for the SSW cluster, indicating long-range correlations in the temporal evolution of the earthquake sequence.

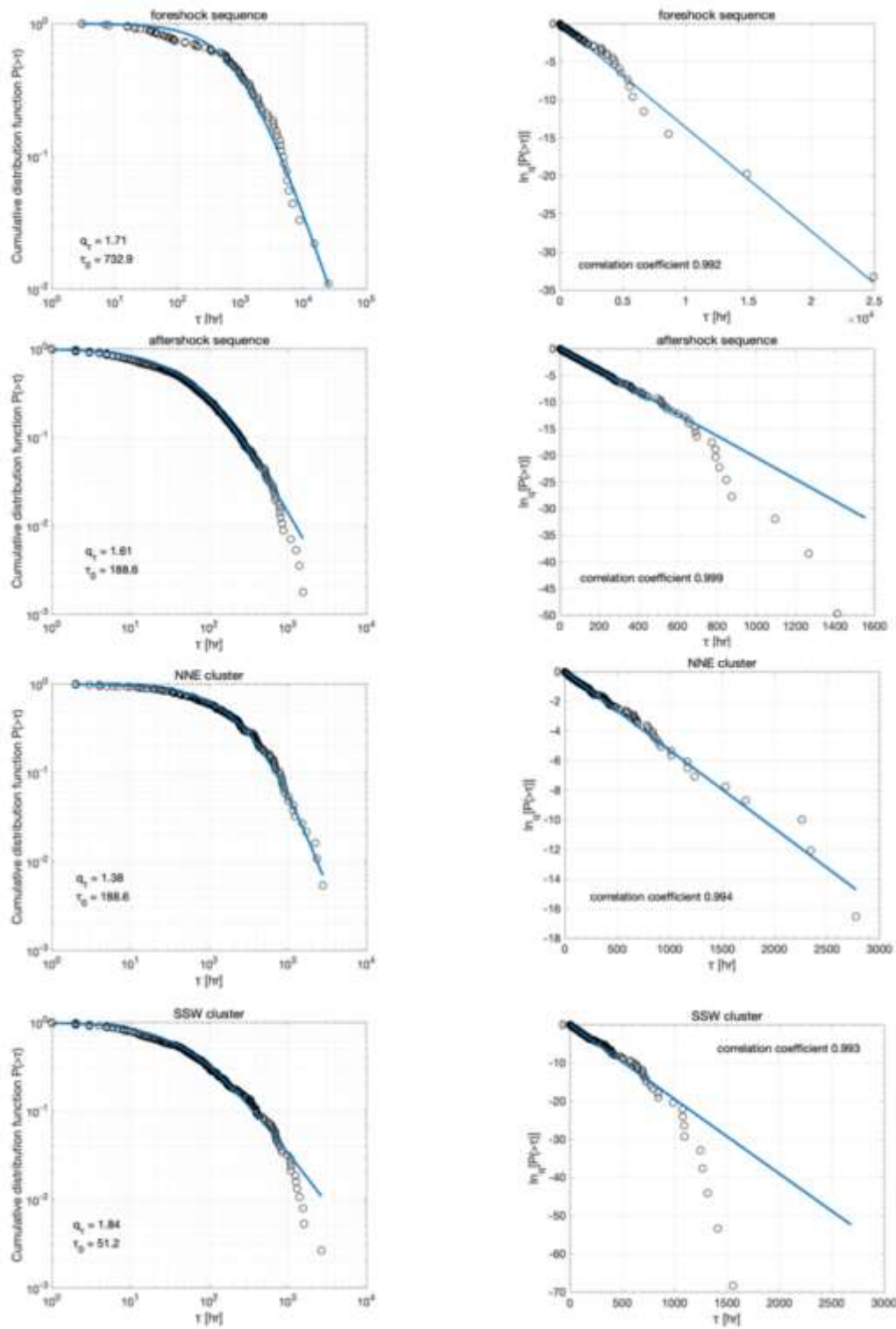


**Fig. 7** - The cumulative distribution function  $P(>\tau)$  of the inter-event times  $\tau$  (in minutes) (left panels) and the corresponding  $q$ -logarithmic function (right panels), represented by circles, for the foreshock sequence, the aftershock sequence, the NNE aftershocks cluster, and the SSW aftershocks cluster. Fitting with the  $q$ -exponential function is shown with the solid lines, for the parameter values and the corresponding correlation coefficients shown in the down left corners.

## 4. Concluding remarks

The strong ( $M_w$ 6.0) mainshock that occurred in Arkalochorion area of Crete on 27 September 2021 came after a nearly 4-month-long foreshock activity. The aftershock activity is spatially distributed in two clusters, the southern and northern ones. Analysis of InSAR images showed that the deformation area nearly coincides with the southern aftershock cluster while maximum subsidence of 20 cm has been estimated. The co-seismic Coulomb stress changes caused by the strong earthquake  $M_w=6.0$  at centroid depth of 9.0 km, as well as the aftershocks spatial distribution indicates stress decrease towards NW and SE and stress increase towards NE and SW of the ruptured faults. The aftershock epicenters are clearly distributed in two main spatial clusters covering the southern and northern sides of the entire cloud. The southern cluster, which is the most extensive one, nearly overlaps with the deformation area determined from InSAR images. The foreshocks and aftershocks interevent times in both clusters) follows a q-exponential distribution indicating long-range correlations in the temporal evolution of the earthquake sequence.

## Acknowledgments

We acknowledge support of this study by the project “Operation of the Hellenic Seismological Network of Crete”, funded by the Region of Crete.

## References

1. Becker D, Meier T, Bohnhoff M, Harjes HP (2010). Seismicity at the convergent plate boundary offshore Crete, Greece, observed by an amphibian network. *J. Seismol.* 14: 369–392.
2. Caputo R, Catalano S, Monaco C, Romagnoli G, Tortorici G, Tortorici L. (2010). Active faulting on the island of Crete (Greece), *Geophys. J. Int.*, 183:111–126.
3. Chelidze T, Vallianatos F, Telesca L (Eds) (2018). *Complexity of Seismic Time Series: Measurement and Application*. Elsevier: Amsterdam, 503-522 ISBN: 9780128131381,
4. Cocco M, Rice J. R. (2002). Pore pressure and poroelasticity effects in Coulomb stress analysis of earthquake interactions. *Journal of Geophysical Research: Solid Earth*, 107(B2), ESE-2.
5. Delibasis ND, Ziazia M, Voulgaris N, Papadopoulos T, Stavrakakis GN, Papanastassiou D, Drakatos G (1999). Microseismic activity and seismotectonics of Heraklion Area (central Crete Island, Greece). *Tectonophysics* 308: 237–248.
6. Elliott J, Walters R, Wright T (2016). The role of space-based observation in understanding and responding to active tectonics and earthquakes. *Nat Commun* 7:13844.
7. Fassoula, C (2001). The tectonic development of a Neogene basalt the leading edge of the active European margin: The Heraklion basin, Crete, Greece. *J. Geodyn.* 31: 49–70.
8. Ganas A, Parsons T (2009). Three-dimensional model of Hellenic Arc deformation and origin of the Cretan uplift. *Journal of Geophysical Research: Solid Earth* 114 B06404.
9. Goldstein R.M., Werner C.L. (1998). Radar interferogram filtering for geophysical applications, *Geophys. Res. Lett.*, 25, 4035–4038.
10. Geodynamic Institute, National Observatory of Athens Seismic Network, <https://doi.org/10.7914/SN/HL>
11. Harris RA, Simpson RW (1998). Suppression of large earthquakes by stress shadows: A comparison of Coulomb and rate-and-state failure. *Journal of Geophysical Research: Solid Earth* 103(B10): 24439-24451
12. Kokinou E, Moisisi M, Tsanaki I, Tsakalaki E, Tsiskaki E, Sarris A, Vallianatos F (2008). A seismotectonic study for the Heraklion basin in Crete (Southern Hellenic arc, Greece). *Int. J. Geol.*, 2, 9–16.
13. Kilb D, Gombert J, Bodin P (2002) Aftershock triggering by complete Coulomb stress changes. *JGR Solid Earth* <https://doi.org/10.1029/2001JB000202>
14. Klein, F.W. (2002). User’s Guide to HYPOINVERSE-2000, a Fortran program to solve for earthquake locations and magnitudes, Open File Report 02-171, US Geological Survey, 1–123, 2002.
15. Lee, W. H. K. and Lahr, J. C. (1972) HYPO71: A computer program for determining hypocenter, magnitude, and first motion pattern of local earthquakes, US Geological Survey Open-File Report, 1–104, 1972.
16. Michas G, Vallianatos F, Sammonds P (2013). Non-extensivity and long-range correlations in the earthquake activity at the West Corinth rift (Greece), *Nonlinear Process. Geophys.* 20: 713–724.
17. Papadakis G, Vallianatos F, Sammonds P (2013) Evidence of Nonextensive Statistical Physics behavior of the Hellenic Subduction Zone seismicity, *Tectonophysics.* 608: 1037–1048.
18. Papadopoulos G.A. (2011). *A Seismic History of Crete: Earthquakes and Tsunamis, 2000 B.C.–A.D. 2010*, 1st ed.; Ocelotos Publ.: Athens, Greece, p. 415. ISBN 978-960-9499-68-2.
19. Papadopoulos, G.A. (2017) Earthquake sources and seismotectonics in the area of Crete. In *Minoan Earthquakes-Breaking the Myth through Interdisciplinarity*, 1st ed.; Jusseret, S., Sintubin, M., Eds.; Leuven University Press: Leuven, Belgium, 165–190.
20. Toda S, Stein RS, Sevilgen V, Lin J (2011). Coulomb 3.3 Graphic-rich deformation and stress-change software for earthquake, tectonic, and volcano research and teaching—user guide. US Geological Survey open-file report 1060: 63
21. Triantafyllou I, Karavias A, Koukouvelas I, Papadopoulos GA, Parcharidis I (2022) The Crete Isl. (Greece) Mw6.0 Earthquake of 27 September 2021: Expecting the Unexpected. *GeoHazards*, 3: 106–124.

22. Tsallis C (2009) *Introduction to nonextensive Statistical Mechanics: Approaching a Complex World*. Springer: Berlin/Heidelberg, Germany,
23. Vallianatos F, Papadakis G, Michas G (2016a). Generalized statistical mechanics approaches to earthquakes and tectonics. *Proc R Soc A* 472-497
24. Vallianatos F, Michas G, Papadakis G. (2016b). A description of seismicity based on non-extensive statistical physics: A review. In *Earthquakes and Their Impact on Society*; D'Amico, S., Ed.; Springer Natural Hazards: Heidelberg, Germany, 1–42.
25. Vallianatos F, Michas G, Papadakis G (2018). Nonextensive statistical seismology: An overview. In *Complexity of Seismic Time Series*; Chelidze, T., Vallianatos, F., Telesca, L., Eds.; Elsevier: Amsterdam, The Netherlands, pp. 25–60
26. Vallianatos F, Michas G, Hloupis G, Chatzopoulos G (2022) The Evolution of Preseismic Patterns Related to the Central Crete (Mw6.0) Strong Earthquake on 27 September 2021 Revealed by Multiresolution Wavelets and Natural Time Analysis. *Geosciences*. 12(1):33.
27. Vassilakis E, Kaviris G, Kapetanidis V, Papageorgiou E, Foumelis M, Konsolaki A, Petrakis S, Evangelidis C.P, Alexopoulos J, Karastathis V, Voulgaris N, Tselentis G.-A (2022). The 27 September 2021 Earthquake in Central Crete (Greece)—Detailed Analysis of the Earthquake Sequence and Indications for Contemporary Arc-Parallel Extension to the Hellenic Arc. *Appl. Sci.*, 12, 2815. <https://doi.org/10.3390/app12062815>
28. Waldhauser, F. (2011). *HypoDD-A Program to Compute Double-Difference Hypocenter Locations*, open-file report, 01-113; U.S. Geological Survey: Menlo Park, CA, USA.
29. Wells DL, Coppersmith KJ (1994). New empirical relationships among magnitude, rupture length, rupture width, rupture area, and surface displacement. *Bulletin of the Seismological Society of America* 84(4): 974-1002
30. Zygouri V, Koukouvelas I, Ganas A (2016). Palaeoseismological analysis of the east Giouchtas fault, Heraklion basin, Crete (preliminary results). *Bull. Geol. Soc. Greece*, 50:563–571.



## Chapter 5

The 2021 Central Crete (Greece)

$M_w$  6.0 ( $M_L$  5.8)

earthquake: an example of coalescent  
fault segments reconstructed from  
InSAR and GNSS data

**Abstract:** The  $M_L$  5.8 earthquake that hit the island of Crete on 27 September 2021 is analysed with InSAR (Interferometry from Synthetic Aperture Radar) and GNSS (Global Navigation Satellite System) data. InSAR coseismic displacements maps show negative values along the LOS of  $\sim 18$  cm for the ascending orbit and  $\sim 20$  cm for the descending one. Similarly, the GNSS data of 3 permanent stations were used in PPK (Post Processing Kinematic) mode to i) estimate the coseismic shifts, highlighting the same range of values as the InSAR, ii) model the deformation of the ground associated with the main shock, and iii) validate InSAR results by combining GNSS and InSAR data. This allowed us to constrain the geometric characteristics of the seismogenic fault and the slip distribution on it. Our model, which stands on a joint inversion of the InSAR and GNSS data, highlights a major rupture surface striking  $214^\circ$ , dipping  $50^\circ$  NW and extending at depth from 2.5 km down to 12 km. The kinematics is almost dip-slip normal (rake  $-106^\circ$ ), while a maximum slip of  $\sim 1.0$  m occurred at a depth of ca. 6 km. The crucial though indirect role of inherited tectonic structures affecting the seismogenic crustal volume is also discussed suggesting their influence on the surrounding stress field and their capacity to dynamically merge distinct fault segments.

---

## 1. Introduction

The location of Crete Island falls within one of the most important seismically active areas in the world, within the Hellenic arc (Figure 1a). This major geodynamic feature formed as a consequence of the Nubia-Eurasia convergence (Caputo et al., 1970; Le Pichon et al., 1979; McKenzie, 1972). Nowadays, the central sector of the Hellenic Arc, south of Crete, is represented by the so-called East Mediterranean Ridge (Finetti et al., 1976; Huguen et al., 2006). As a result of the rapid S-W movement of the southern Aegean with respect to Eurasia, the Mediterranean oceanic crust subducts northwards with a velocity of 35 mm/a (which greatly exceeds the convergence rate between Africa and Eurasia, approximately 5-10 mm/a) below Crete and the Peloponnese (Reilinger et al., 2010).

The tectonics of Crete Island is currently dominated by crustal extension likely as a result of the slab retreat (Bocchini et al., 2018), the Aegean mantle wedge intrusion (Halpaap et al., 2019) and the subsequent strong uplift (Robertson et al., 2019). Stretching directions are, however, not regionally uniform (Angelier, 1979) as clearly documented by the variable trend of the major active normal faults affecting the island of Crete (Caputo et al., 2006) and its surroundings (Caputo and Pavlides, 2013).

On September 27, 2021, a moderate  $M_L$  5.8 earthquake affected Central Crete (Greece) not far from the city of Heraklion (Figure 1). The structural damage of the villages close to the epicentral area, located near Arkalochori, was considerable, and there were several injured and one person died; furthermore, the shaking effects of the mainshock have been widely felt across the island. Within the first 24 hours after the mainshock, an  $M_L$  5.2 and several  $M_L$  4+ aftershocks occurred (Table 1).

**Table 1:** Mainshock and aftershock ( $M > 4.5$ ) focal mechanism of the 2021 Central Crete seismic sequence (National Observatory of Athens - NOA data) immediately following the earthquake.

Magnitude ( $M_L$ ) & focal mechanisms (NOA)	Date-Time	Location	Latitude (°N)	Longitude (°E)	Depth (km)
5.8 (main) 	2021/09/2 7 06:17:21	23.3 km SE of Heraklion	35.1512	25.2736	10
4.5 	2021/09/2 7 07:30:45	23.7 km SSE of Heraklion	35.1334	25.2457	14
4.7 	2021/09/2 7 11:02:25	19.5 km SE of Heraklion	35.1805	25.2525	13
5.2 	2021/09/2 8 04:48:09	20.8 km SSE of Heraklion	35.1540	25.2232	11
4.6 	2021/09/2 8 15:13:15	23.4 km SSE of Heraklion	35.1466	25.2663	14
4.6 	2021/09/2 9 11:54:49	21.3 km SSE of Heraklion	25.2058	25.1561	16

The crustal volume that was reactivated by the 2021 seismic sequence is at present stretched along a ca. ESE-WNW direction (Vassilakis et al., 2022; Ganas et al., 2017; 2022) and the observed kinematics of the events is mainly dip-slip normal.

The distribution of the epicentres partially overlaps the southwestern sector of the Kastelli seismogenic source included in GreDaSS (GRCS743) (Caputo and Pavlides, 2013) for which has been estimated a maximum magnitude of 6.4. The fault trace of this tectonic structure has been mapped for about 22 km showing a curved shape geometry with ENE-WSW strike in the NE sector and NNE-SSW orientation towards its SW termination. Based on morphotectonic analysis and empirical relationships (Caputo et al., 2010a), the estimated mean recurrence interval is about 812 years over the last 13 ka with maximum vertical displacements of 65-70 cm. Among the several faults affecting the eastern sector of the Heraklion Basin with variable settings, the Kastelli Fault has been considered the most active tectonic structure (Fasoulas, 2001) and this is likely confirmed by microseismic activity recorded in the area (Delibasis et al., 1999).

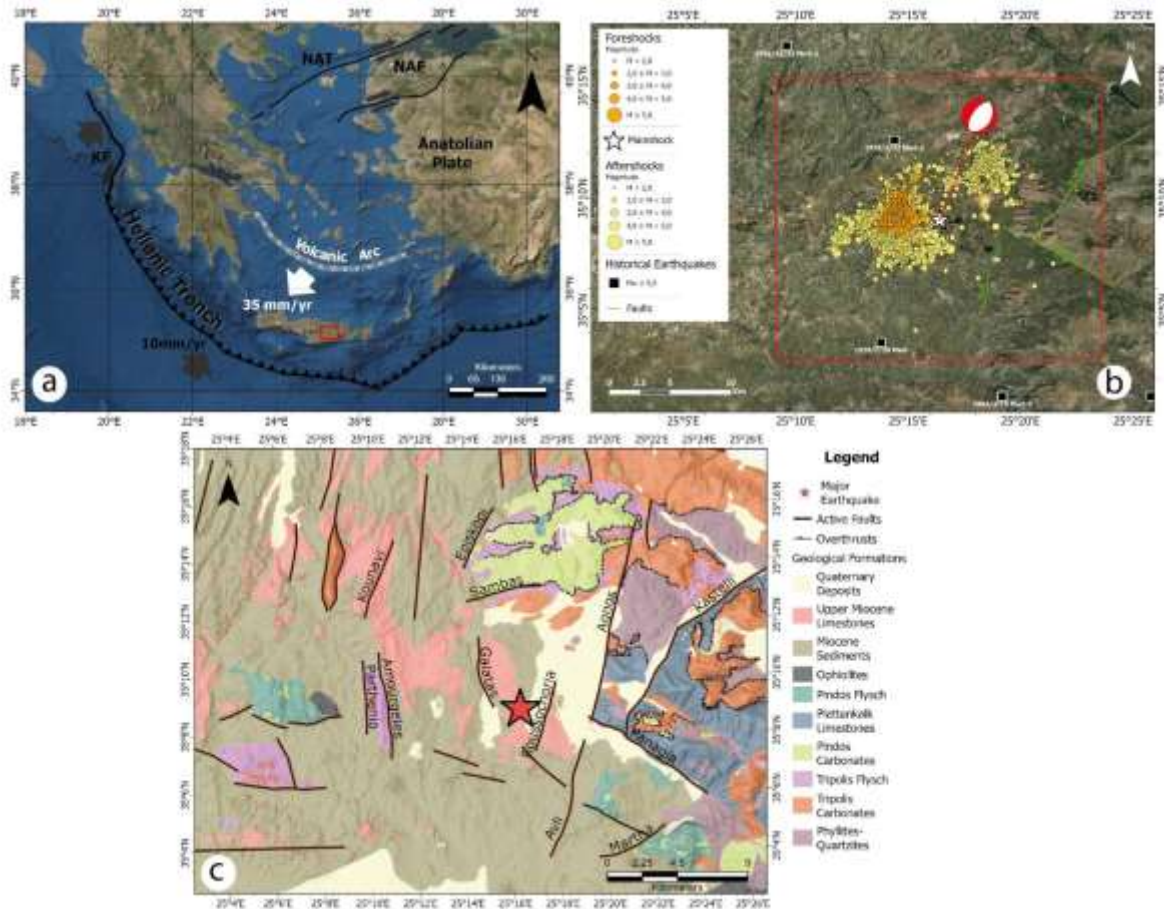


**Figure 1.** (a) Indicative map of the main structural characteristics of the Hellenic Arc and Trench system. KF: Kefalonia Transform Fault, NAF: North Anatolian Fault, NAT: North Anatolian Trench. The white thick arrow shows the direction of relative motion between the Aegean and Nubian plates accommodated by the Hellenic subduction (Kokkalas et al., 2001). The red box indicates the study area. (b) Map of the investigated area showing the epicenter (white star) and the focal mechanisms of the mainshock, the M>5 historical earthquakes from 1900 up to today (<https://www.gein.noa.gr/en/services-products/earthquake-catalogs/>), the foreshocks and the aftershocks (from 1 June to 18 October 2021 relocated by Vassilakis et al., 2022) and the composite seismogenic sources included in GreDaSS (Caputo and Pavlides, 2013); (c) Simplified geological map of the broader area (IGME, 1989) draped on a shaded relief, with the traces of the major active faults (Ganas et al., 2013) affecting the area.

Several reporting agencies provided moment tensor solutions for the mainshock (visit of 1 October 2021 to the portal <https://www.seismicportal.eu/mtws/>), suggesting that the activated normal fault had a mean NW dip-direction with a dip angle of about  $54^\circ$ , in agreement with the geological observations (Caputo et al., 2006; 2010a; Vallianatos et al., 2022b; Vassilakis et al., 2022).

Nearly four months prior to the occurrence of the mainshock, several foreshocks had been recorded in the broad area (Vallianatos et al., 2022a), and several aftershocks occurred in the days and months that followed. From June 1st to July 24th, about 155 foreshocks were recorded with magnitudes up to  $M_L$  4.3, with four exceeding  $M_L$  4.0. At 02:07:37 UTC on July 24th, a moderate pre-shock with magnitude  $M_L$  4.8 and hundreds of foreshocks with magnitudes up to 3.8 occurred until the main event.

In the following days, several major aftershocks occurred, about eight of magnitude greater than or equal to  $M_L$  4.2, of which the largest occurred on September 28 at 4:48:09 UTC ( $M_L$  5.3). Consequently, thousands of people suffered damages as a result of the continuous seismic activity. The most serious damage occurred near the village Arkalochori.

In the present research, the main seismic event with  $M_L$  5.8 was analysed using ground displacement data derived from InSAR (Interferometry from Synthetic Aperture Radar) (Massonnet and Feigl, 1998) and GNSS (Global Navigation Satellite System) (Alac et al., 2016) techniques in order to constrain the fault kinematic and calculate the slip distribution of the rupture surface following the mainshock.

The causative fault parameters of the earthquake were determined by a nonlinear inversion of InSAR and GNSS displacement data, and the slip distribution of the source was determined by using a linear inversion algorithm.

Beyond the contribution to our seismotectonic knowledge, a second major goal of the present work is to investigate the compatibility of the causative fault with previously known local structures and/or the identification of new potential structures.

## 2. Materials and Methods

The data analysis of the 2021 Central Crete sequence is based on the following three steps:

- a two-pass SAR phase interferometric analysis to get the surface displacement field;
- determination of punctual 3D coseismic offset through the differential analysis of GNSS data;
- reconstruction of the source model through joint inversion of InSAR and GNSS data.

### 2.1 InSAR Analysis

The InSAR analysis is based on SAR images of Sentinel-1 satellites, ESA (European Space Agency) constellation, in IW (Interferometric Wide) mode and V-V polarisation. Four images, in pairs of two and with a temporal distance of 12 days, along the ascending and descending orbits (table 2), were used to retrieve the coseismic displacement field. Both pairs include 3 days of aftershocks, expected to give a negligible contribution compared to the mainshock.

For each pair, images have been co-registered and multi-looked 4 and 1 in range and azimuth direction, respectively, to obtain a final ground resolution of about 30 m, thus increasing the SNR (Signal-to-Noise Ratio); then orbital corrections were applied using ESA PO (Precise Orbits) and the SRTM-1 digital elevation model was used to remove the topographic phase contribution.

The application of the adaptive filtering algorithm to the raw interferograms allowed us to significantly increase the quality of interferometric fringes, by reducing the phase noise (Goldstein et al., 1998). Through the MCF (Minimum Cost Flow) algorithm the unwrapping interferogram was obtained (Costantini et al., 1998). The unwrapped maps were then geocoded with the same SRTM-1 DEM with a pixel resolution of 30 m.

**Table 2.** Sentinel-1 images used for InSAR processing of M<sub>L</sub> 5.8 Central Crete Earthquake.

event	interferogram number	pre-event date	post-event date	orbit	incidence angle	track
M <sub>L</sub> 5.8 - 23.3 km SE of Heraklion	1	18/09/2021	30/09/2021	ascending	35,55742	29
2021-09-27 06:17:21 (UTC)	2	18/09/2021	30/09/2021	descending	38,352143	109

## 2.2 GNSS Analysis

In the current study, the GNSS data were used both to estimate the co-seismic shifts, and to model the ground deformation associated with the mainshock by combining GNSS and InSAR data for analysis, in addition to validation of the InSAR results (Floyd et al., 2020; Kuzin, 2021; Jaduszliwer et al., 2021; Oktar et al., 2021, Redhwan et al., 2021; Sakkas, 2021; Tiryakioglu et al., 2017).

We processed the data of three permanent GNSS stations on the island of Crete, belonging to the commercial network of METRICA SA (HexagonSmartNet), in PPK (Post Processing Kinematic) mode using the RTKLib software (Takasu et al., 2007) (Figure 2):

- ARKL located in the epicentral area (used as a Rover);
- HERA and MOI1 (located at Heraklion and Mires, respectively), which are both outside the area that suffered instability following the earthquake (used as Bases).

The HERA and MOI1 stations, used as reference bases in this configuration, have a distance from the Rover station (ARKL) approximately 24 and 36 km, respectively.

The characteristics of the equipment of the three GNSS stations are:

- **HERA:** Receiver LEICA GRX1200+GNSS, Antenna LEIAR10 NONE;
- **ARKL:** Receiver LEICA GR10, Antenna LEIAR10 NONE;
- **MOI1:** Receiver LEICA GR30, Antenna LEIAR10 NONE.

By working in PPK, it is possible to reach accuracies in the positioning at the centimetre level, if not too long baselines are used and the ambiguities of phase integers of the carrier are correctly resolved (Rizos et al., 1997). However, it has been shown that accuracies of a few centimetres can be reached even with greater distances (> 25 km) as long as the correct parameters are properly set (Sugar et al., 2021).

As described below, the processing of GNSS data with the PPK method allowed an in-depth analysis of the kinematics of the ARKL station with respect to two different bases, and highlighted the usefulness of this method in evaluating the earthquake effects on the ground.

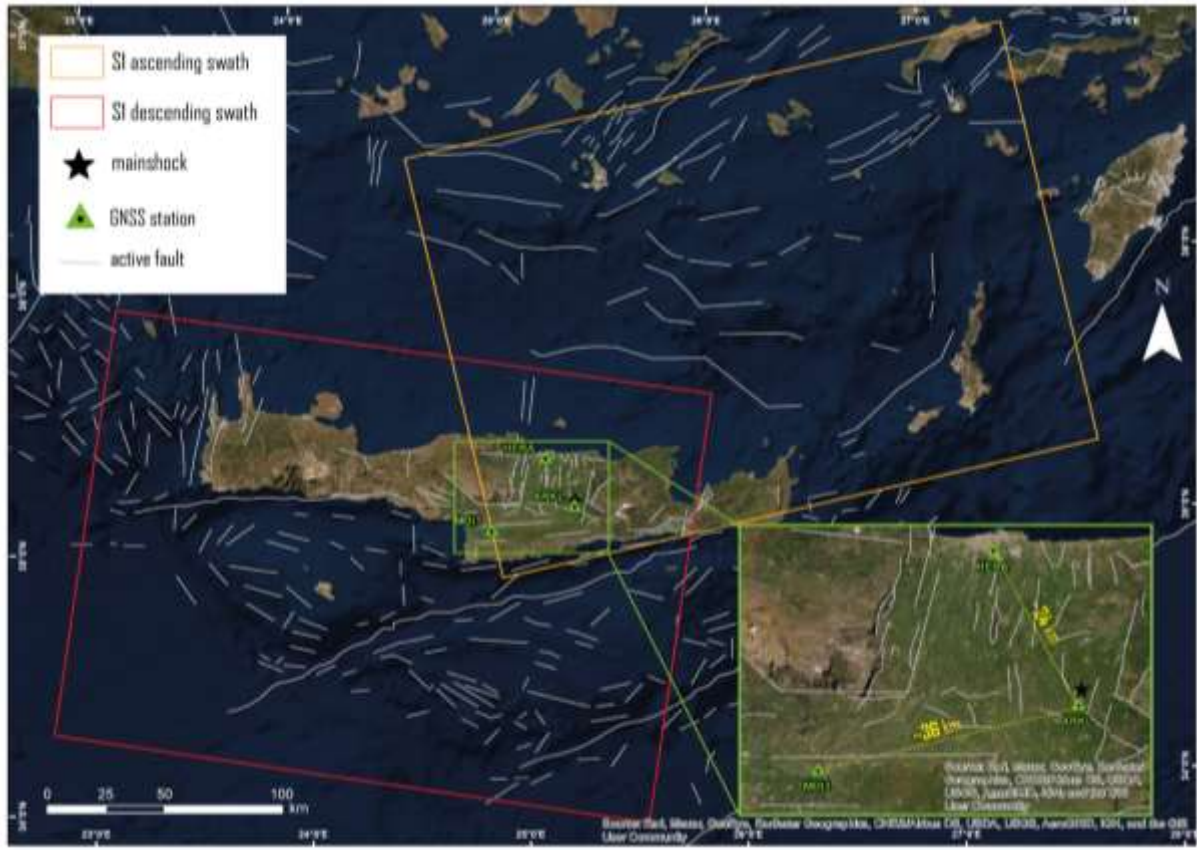


**Figure 2.** The location of the three permanent GNSS Crete Stations and IW Swath of Sentinel 1 images.

### 2.3 Source Modelling Analysis

Data modeling was conducted over a set of points regularly sampled from the ascending and descending raster displacement maps with two different spatial resolutions: 500 m in the fault near-field and 2000 m in the far field (see the point distribution in Figure 9).

InSAR LOS co-seismic points were then jointly modelled with 3D GNSS points using a dual step validated approach: at first it was carried out a non-linear inversion to trace the geometry and position of the fault, using a uniform dislocation value; then we applied a linear inversion to calculate the slip distribution on the inverted fault plane, subdivided into square elements and opportunely extended to include the whole distribution, from the peak value to zero. In both inversions, the underlying geophysical model used to predict the surface displacement is the elastic dislocation induced by a finite source in a homogeneous half-space (Okada et al., 1985), with the Williams and Wadge (1998) approach to account for the local topography. The linear inversion is conducted with the additional Non-Negative Least-Square (NNLS) constraint, preventing unrealistic back-slip values, and the inclusion of a regularisation contribution, opportunely weighted with a try-and-error damping factor (Menke, 1989; Funning et al. 2005; Wright et al., 2003; Golshadi, Z. et al., 2022). Details about both non-linear and linear inversion algorithm implementations can be found in Atzori et al. (2008; 2009).

An iterative procedure of the Levenberg-Marquardt optimization algorithm was used for non-linear inversion (Marquardt et al., 1963). Based on the parameter ranges given, the optimization uses the weighted squares of the residuals to minimize the objective function F:

$$F = \frac{1}{N} \sum_{i=1}^N [(d_i - f(m)) / \sigma_i]^2 \quad (1)$$

Where  $d_i$  is the observation value of the  $i$ -th data point;  $\sigma_i$  represents the standard deviation relating to each datum;  $m$  represents the model parameters vector and  $f$  is the non-linear forward Okada's model (Okada et al., 1985) in the inversion that consists of  $N$  points. As part of this approach, the model parameter vector  $m$  is defined in order to minimize  $F$ . The cost function is a weighted mean of the residuals between observed and predicted data sets. Using multiple restarts, the minimization algorithm can reasonably guarantee catching the global minimum. As part of the

linear inversion procedure, we maintained the fixed geometric settings derived from our preferred non-linear inversion to get the slip distribution along the fault. During this procedure, the fault spread out until the slip vanished to zero and it was subdivided into small patches. Each patch's slip value was obtained from joint inversion of the ascending and descending InSAR and GNSS datasets (Atzori et al., 2008). We used a trial-and-error approach for system damping to avoid backslip, in which the empirical parameter is balancing the slip distribution roughness and the data fit (Funning et al. 2005; Wright et al., 2003).

### 3. Results

#### 3.1 InSAR Results

The dates relating to the used SAR acquisitions have a temporal baseline of 12 days (Zebker and Pepin, 2021), therefore including six events ( $M > 4.5$ ) of the seismic sequence (in particular, the mainshock of 2021-09-27 at 06:17:21 (UTC) and five aftershocks that took place in the following hours and days) (Tables 1 and 2).

Thanks to this short time interval, as shown in (Figure 3), the produced interferograms have good coherence ( $> 0.6$ ) gaps and prove to be similar to each other. In the production of differential interferograms, the coherence factor is strongly influenced by the temporal baseline and the spatial decorrelation between the reference image and the repeated images. Considering the 12-days time interval and the good quality of Sentinel images, the high level of coherence ( $> 0.6$ ) was maintained across the whole investigated area (Hanssen et al., 2001).

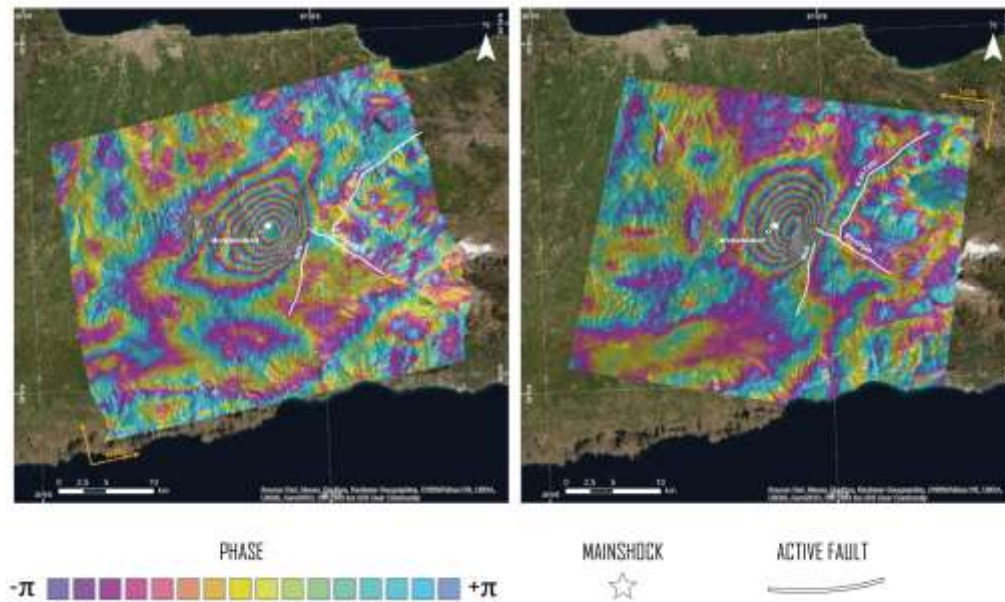


**Figure 3.** Ascending (left) and descending (right) wrapped interferograms of the 2021 M 5.8 Heraklion earthquake.

The displacement maps along both orbits show a very similar deformation pattern, indicating that the actual ground movement is predominantly vertical, as also visible from the conversion from ascending and descending to vertical and horizontal components (Figure 7) (Dai et al., 2015; Pepe et al., 2017). More intense displacements occurred at the epicentral area of the mainshock where there is a lowering of the ground up to 20 cm (Figure 4).

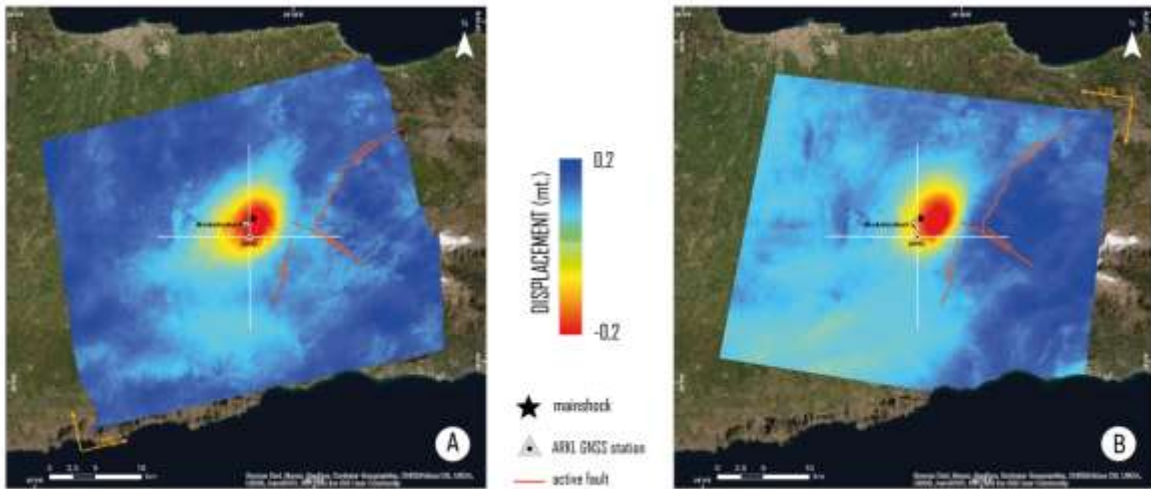


**Figure 4.** Ascending (left) and descending (right) displacements. The mainshock is highlighted with a black star.

These maps show a peak of displacement (red colour) moving away along LOS direction in the vicinity of the city of Arkalochori, explaining the extensive structural damages in the neighbouring villages.

Four maps were produced relative to the two transects (Figure 4), two for each orbital direction. The transects were traced in the N-S (North-South) and E-W (East-West) directions, and their crossing point coincides with the position of the ARKL GNSS station.

The elevation profiles of the two orbital directions, ascending and descending, were obtained from the two transects. Profiles on North-South and East-West directions were produced to examine the displacement field along these directions. In each profile, the results obtained with the two softwares (SARscape and SNAP, represented by red and blue curves, respectively, in Figure 5) were compared (Tolomei et al., 2021).

In particular, negative displacements along LOS (away from the sensor) of ~18 cm for the ascending orbit and ~20 cm for the descending one are highlighted.

Moreover, it has to be emphasized the good agreement of the epicentral area of the  $M_L 5.8$  event with the maximum displacement area depicted in all profiles.

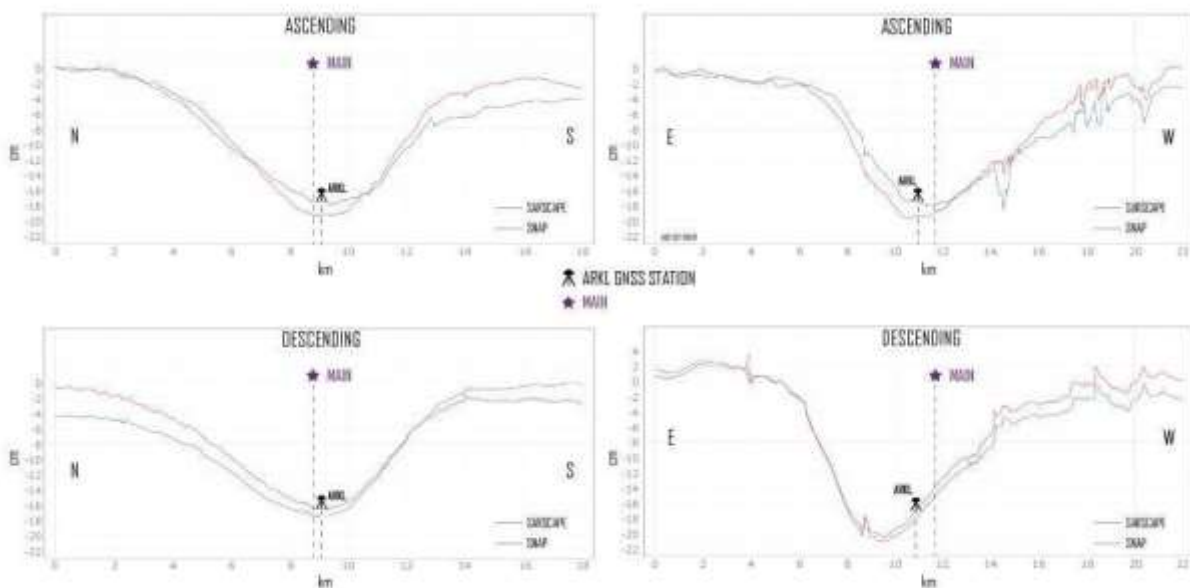


**Figure 5.** Cross sections along the S-N and E-W transects shown in Figure 4.

### 3.2 GNSS Results

The GNSS data were analysed using a differential kinematic post-processing (PPK) approach with the RTKPOST ver.2.4.3 b34 GNSS Post-Processing Software.

Two baselines were then calculated:

- **ARKL-HERA**; with ARKL acting as rover and HERA being the base;
- **ARKL\_MOI1**; with ARKL also being the rover and MOI1 set as base.

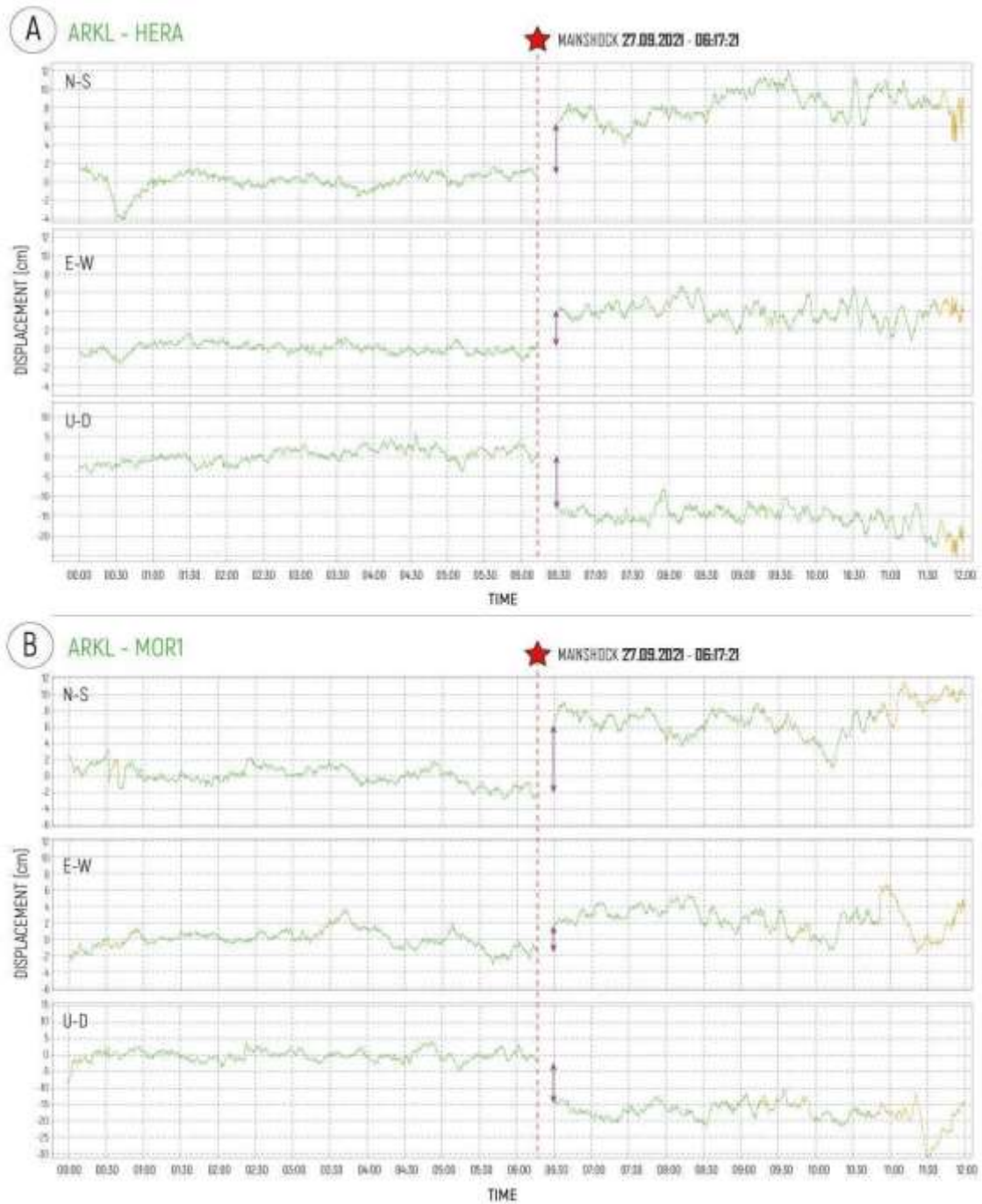


**Figure 6.** Time series during the day of the ML5.8 event showing the co-seismic GNSS displacements in the three components of the ARKL station with respect to the HERA base (A) and with respect to the MOI1 base (B).

Since the data from the ARKL station show an interruption during the seismic event (from 06:17:30 to 06:30:30), for each of the two baselines, about 6 hours pre- and post-event were processed: that is to say, from 00:00 to 06:17 and from 06:30 to 12:00 of 27/09/2021, as it can be seen in figure 6.

The GNSS data (of GPS and GLONASS constellations only) were processed using IGS precise orbits (Beutler et al., 1999) in Kinematic mode with an automatically combined of forward and backward directions.

This procedure maximises the accuracy of the solutions and improves the quality control (Erol et al., 2020). Based on this processing strategy the following results were obtained: ARKL-HERA baseline phase ambiguities fix at 99.3%, while ARKL-MOI1 92.8% fix. From the linearly fitted positions of the pre- vs post-solution, we estimated the three components (E-W, N-S and U-D) of the displacement vectors using the Vincenty formula (Vincenty, 1975; 2013).

The GNSS data act not only as GCPs (Ground Control Points) during the processing of the phase SAR data, but also validate the InSAR products (Cheloni et al., 2017). The displacements deriving from the interferograms were thus compared with the co-seismic offsets obtained from the geodetic data (vertical and E-W components), as represented in Figure 7.

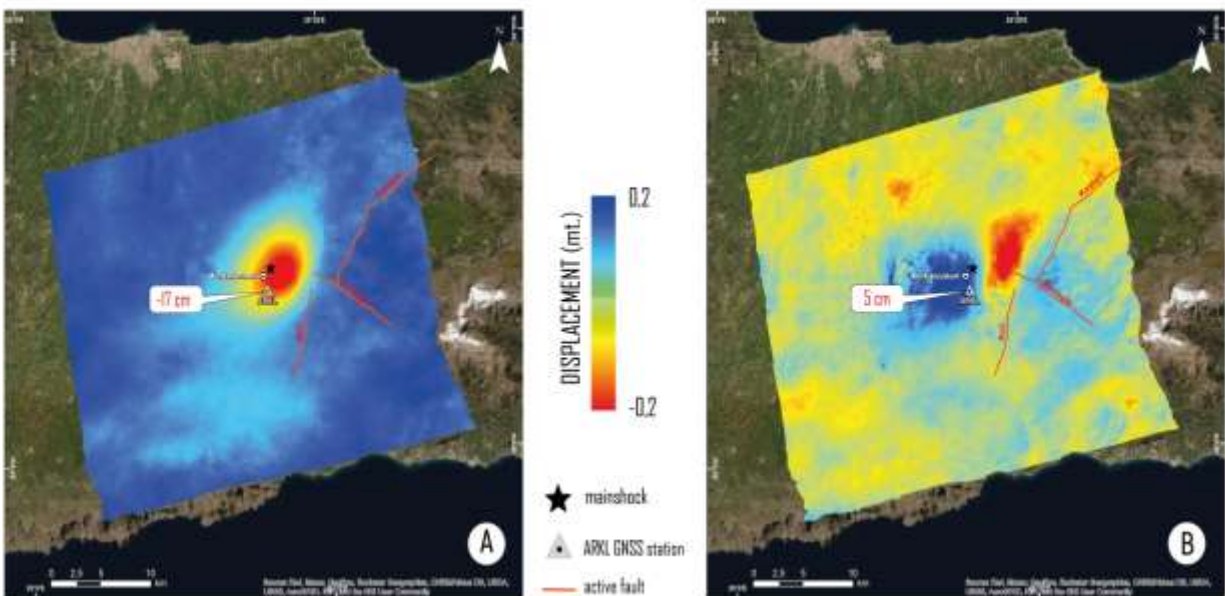


**Figure 7.** Vertical (A) and E-W (B) InSAR deformation components with relative GNSS ARKL Station co-seismic offset values.

The figure shows the agreement between the InSAR and GNSS data along the U-D and E-W directions: the largest subsidence value is highlighted in the epicentral area and is equal to about 20 cm, a more significant displacement of 11 cm towards the east of the footwall block and about 7 cm towards the west of the hanging-wall block confirming an important E-W component of crustal stretching.

The co-seismic offsets obtained from GNSS data were projected into LOS (ascending and descending) direction and are reported in table 3.

**Table 3.** Co-seismic Offset of GNSS PPK processing.

Stations	Time	Latitude	Longitude	Height
<b>ARKL-HERA</b>	<i>Pre Mainschok</i>	35.1339	25.2689	472.48980
	<i>Post Mainschok</i>	35.1339	25.26894	472.33980
	$\Delta$ (cm)	8.25	3.90	-15
	$\Delta$ (cm) projected on LOS (Asc): -17.81			
	$\Delta$ (cm) projected on LOS (Desc): -12.80			
stations	time	latitude	longitude	height
<b>ARKL-MOI1</b>	<i>Pre Mainschok</i>	35.13390	25.26890	472.59870
	<i>Post Mainschok</i>	35.133970	25.26890	472.41760
	$\Delta$ (cm)	7.30	4.48	-18.11
	$\Delta$ (cm) projected on LOS (Asc): -20.82			
	$\Delta$ (cm) projected on LOS (Desc): -12.06			

### 3.3 Source Modelling Results

We jointly modelled the dataset of points sampled from InSAR data and displacements obtained from GNSS, assuming that the dislocation occurred over a single surface simplified as a planar geometry, for which all the parameters were left free in the non-linear inversion. The importance of different datasets in modeling was handled by weighting them according to the automatic approach described in Atzori et al. (2019).

The results of the modelling show a best-fit source with an almost purely dip-slip normal kinematics (rake  $-106^\circ$ ) characterised by a mean slip of about 0.9 m. The reconstructed fault plane dips N-W (strike  $214^\circ$ ) with an angle of  $50^\circ$ . The length and width of the uniform slip source are 5.5 and 5.8 km, respectively (the results of analysis from non-linear inversion are added in the auxiliary materials).

This uniform slip model was then extended to  $15 \times 13$  km and subdivided into elements of  $1 \times 1$  km to get the slip distribution. The results show a single slip peak distribution that reaches the highest value ( $\sim 1.0$  m) at a depth of  $\sim 6$  km, with the most whole dislocation included between about 3 and 12 km of depth (Figure 8).

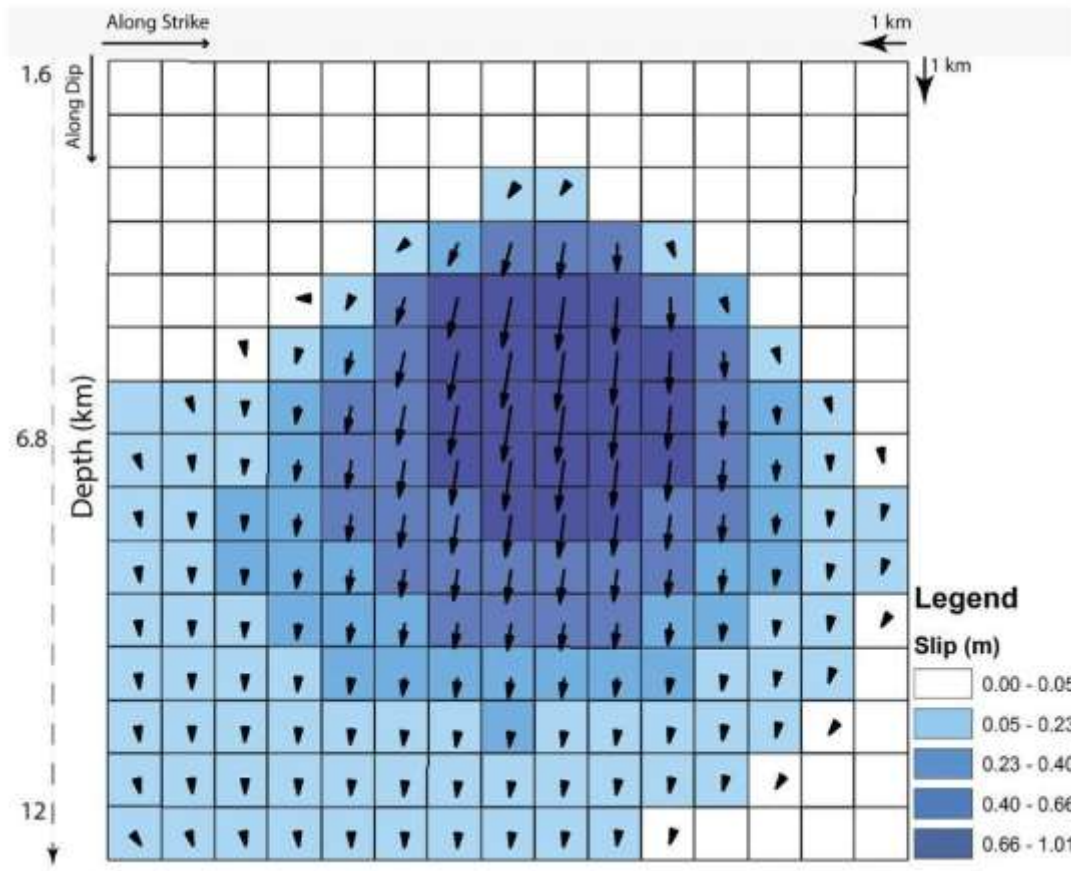


**Figure 8.** M<sub>L</sub> 5.8 main event slip distribution. The top of the modelled area is placed at a depth of 1.6 km.

The comparison between observed and predicted surface displacement based on the Okada modelling, together with the residuals, basically confirm the high reliability of the obtained solution (Figure 9 and Table 4). The observed, modelled and residuals signals, derived from joint linear least-square inversions for both observations, are shown in Figure 9.

The results of GNSS data inversion are also shown in Table 4. During the processing, we tried to smooth and reduce the residual patterns for all datasets.

**Table 4.** Observed and modelled co-seismic offset (cm) of GNSS processing projected on LOS direction.

Stations (rover-base)	Ascending observed	Ascending modeled	Descending observed	Descending modeled
ARKL- HERA	-17.81	-17.56	-12.80	-11.68
ARKL-MOI1	-20.82	-20.03	-12.06	-10.36

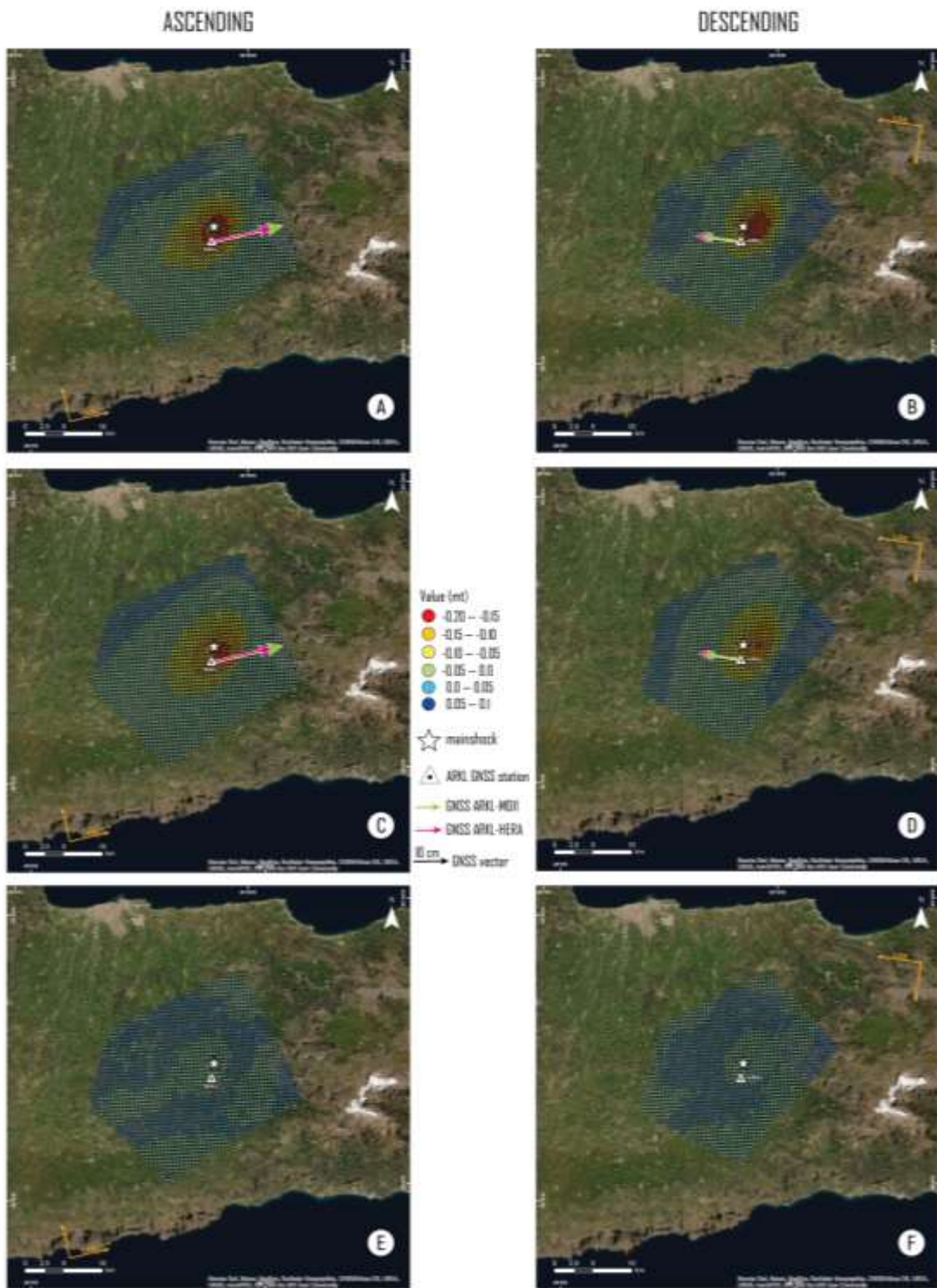


**Figure 9.** Observed (A and B), modelled (C and D) and residual (E and F) maps for displacement obtained from both pairs. The colored arrows represent the displacement vectors of the GNSS, observed and modeled, along the Line Of Sight (LOS) of the satellite. The white star shows the location of mainshock. The white triangle indicates the position of the ARKL GNSS station.

#### 4. Discussion and Conclusions

In this study, a moderate earthquake with the magnitude of  $M_L$  5.8 that struck the island of Crete on 27 September 2021 was analyzed. The event occurred in a tectonically active area characterized by multidirectional crustal extension associated to several causes, like the rapid roll-back of the Hellenic subduction slab, the Aegean mantle wedging and the consequent uplift, the post-orogenic collapse and the arc-parallel stretching.

InSAR images and GNSS data were used to determine the characteristics of the mainshock causative fault and to better understand what happened during the earthquake. The seismic event caused severe damages in the epicentral area and was followed by several aftershocks.

Based on the ascending and descending orbital geometries, the obtained interferograms show the same number of deformation fringes, which indicates that this seismic sequence produced ground movement mainly in the vertical direction (U-D) and only slightly in the horizontal direction (E-W).

The unwrapping phase interferograms confirm coseismic shifts in the mainshock epicentral area. With the aid of two transects traced in the N-S and E-W directions it was possible to emphasise the occurrence of negative displacements along LOS (away from the sensor) of  $\sim 18$  cm for the ascending orbit and  $\sim 20$  cm for the descending one. These results are in good agreement with Triantafyllou et al. (2022), Vassilakis et al. (2022) and Ganas et al. (2022) though some minor differences in the numerical values exist.

The data of three permanent GNSS stations were processed in PPK (Post Processing Kinematic) mode. The station called ARKL positioned in the epicentral area was used as Rover; instead, the HERA and MOI1 stations, a few tens of km from the epicenter, were used as Bases. The results show negative coseismic displacements of about 15-18 cm on the vertical, of about 4-5 cm in the east direction and about 7-8 cm towards the north. Projecting the results to LOS directions, our InSAR results showed good agreement also with the GNSS-based results.

Compared to previously published solutions (Triantafyllou et al., 2022), which highlighted a geodetic seismic moment calculated from the Okada's formalism of  $1.14 \times 10^{18}$  Nm ( $M_w$ 6.0), and a maximum slip of 1.03 m at depths from 3.5 km to 5 km, our model, which is based on a joint inversion of InSAR and GNSS data, seems to provide a better data fit.

In the present research, we also calculated the slip distribution of the source using an algorithm for joint linear inversion of the datasets. The results indicate a major fault striking  $214^\circ$ , dipping  $50^\circ$  towards NW and with an almost dip-slip kinematics (rake:  $-106$ ). The modelled surface rupture extends at depth up to ca. 12 km and it is partially located in correspondence of the south-southwestern sector of the Kastelli active fault (Caputo et al., 2010b), which was clearly considered as a potential seismogenic source in GreDaSS (Caputo and Pavlides, 2013). Moreover, the obtained results indicate a maximum slip of  $\sim 1.0$  m, occurred at a fault depth of 6 km, comparable to the displacement values suggested by Caputo et al. (2006) for the same fault (Figures 8 and 10).

As concerns the modelled source proposed by Ganas et al. (2022), although their slip distribution shows a single peak similar to ours, some differences relative to the new results should be emphasised: i) our reconstructed rupture surface is slightly broader, being the maximum dimensions ca.  $15 \times 13$  km ( $W \times L$ ); ii) conversely, the maximum slip value is smaller (1.01 m instead of 1.2 m), though occurring at a comparable depth of 5-6 km; iii) the dip-angle obtained in the present research is slightly smaller ( $50^\circ$  instead of  $55^\circ$ ); iv) our best-fit strike is  $214^\circ$  instead of  $195^\circ$ ; v) the minimum and maximum depths are both deeper (3 and ca. 12 km instead of 1.2 and 10 km). After all, these differences possibly explain the better fit we obtain between the modelled rupture surface (Figure 10) and the hypocentral distribution of the events belonging to the aftershock sequence (e.g. compare with Fig. 9 of Ganas et al., 2022).

Our results are in agreement with the moment tensor solutions for the main event obtained by several reporting agencies ([https://www.emsc-csem.org/Earthquake/index\\_tensors.php](https://www.emsc-csem.org/Earthquake/index_tensors.php)) suggesting the activation of a normal fault with a mean NW dip-direction and approximately  $54^\circ$  dip-angle.

Similarly, the total seismic moment release of  $1.17 \times 10^{18}$  Nm that we estimated, corresponding to a magnitude close to 6, falls within the range of the values reported by the USGS and GCMT, while also the focal mechanism for the modelled source is in agreement with the USGS and GCMT solutions. It should be noted that the aftershocks distribution of the 2021 sequence is clustered in two distinct subvolumes (Figure 10a) suggesting the occurrence of two segments at depth behaving somehow independently. In between, there is a sort of 'silent' volume that is exactly aligned with the westward extension of the Panagia Fault (Figure 10), which is also referred to as Nipitidos Fault by Vassilakis et al. (2022).

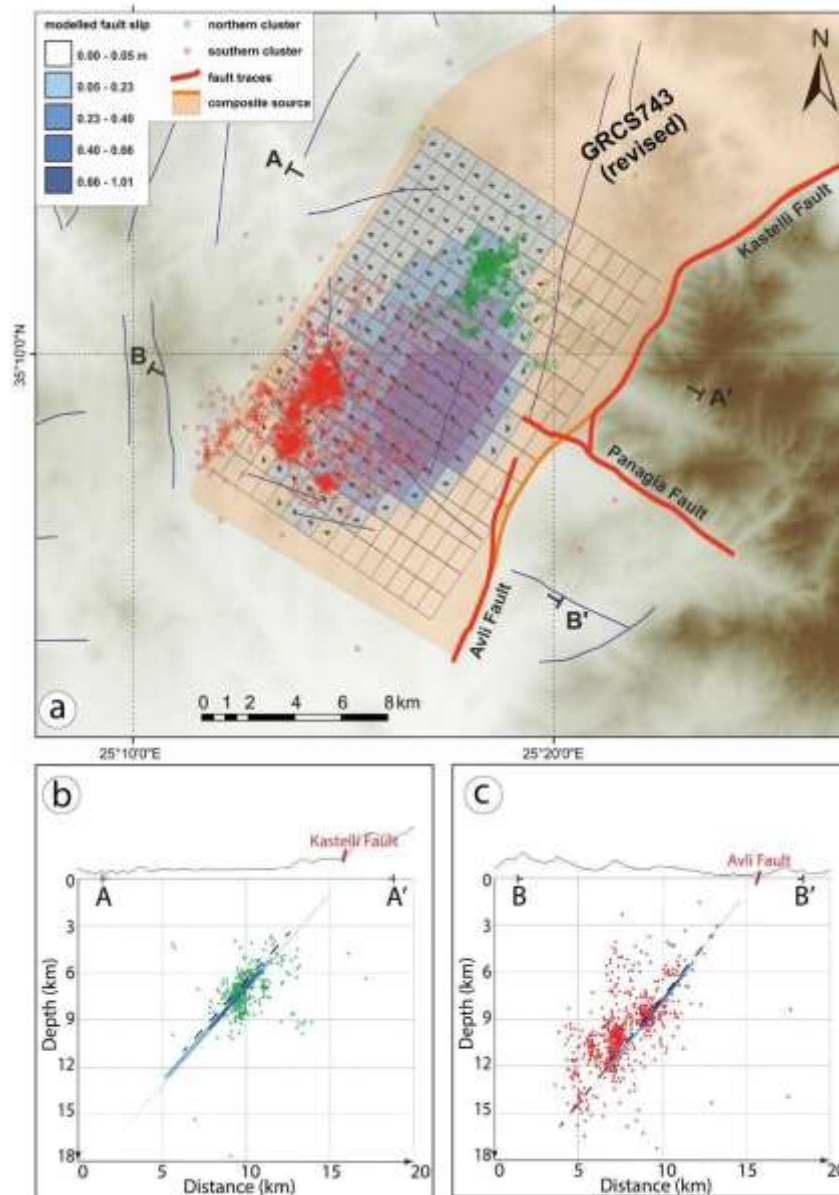


**Figure 10.** a) Map view of the investigated area showing the seismicity from Vassilakis et al.(2022) and the slip modelled fault; b) and c) profiles orthogonal to the modelled slip surface showing the aftershock sequence plotted within a distance of ~ 3 and 4 km for the A-A' and B-B' profiles, respectively. Red and green dots indicate the two seismic clusters. For slip distribution on the modelled surface, see Figure 8. The orange shaded area in (a) indicates the proposed revised geometry for the composite seismogenic source GRCS743 (Caputo and Pavlides, 2013).

It is also noteworthy that the latter tectonic structure does not affect at all the Quaternary deposits of the Messara Basin (Figure 1b). This (lack of) evidence, in turn, strongly supports the hypothesis that the Panagia Fault has not been recently reactivated, at the least along its western segment buried under the Quaternary deposits of the Messara Basin. Accordingly, from a seismotectonic point of view this tectonic structure should be considered as an inherited crustal weakness zone crossing some of the NNE-SSW trending active faults mapped in the area (like the Kastelli and Avli faults).

Although inactive, the Panagia Fault had an important, though indirect, role during the 2021 Central Crete event. This role was indeed played either at depth, by partitioning the behaviour of the seismogenic volume (as depicted by the two aftershocks clusters), but probably also within the shallowest crustal volume where the slip surface of the cumulative neotectonic fault (i.e. composite seismogenic source) likely branches at few km depth, say at circa 3-4 km, in correspondence of the intersection with (and a consequence of) the Panagia Fault (Figure 11).

Indeed, in case of a stronger event, the upwards coseismic rupture would have reasonably reached the topographic surface, i.e. linear morphogenic earthquake (Caputo, 2005), as largely predicted by empirical relationships (Pavlidis and Caputo, 2004), therefore cumulating further throw along the Kastelli and the Avli fault scarps, north and south of the Panagia Fault, respectively. This process could have occurred several times during the latest Quaternary, post-LGM (Caputo et al., 2006).

Relative to the composite seismogenic source labelled GRCS743 included in GreDaSS (Caputo and Pavlidis, 2013), it is worth to emphasise that the cross-cutting relationships with the Panagia Fault and the overstep geometry with the Avli Fault were likely assumed as hard segment boundaries.

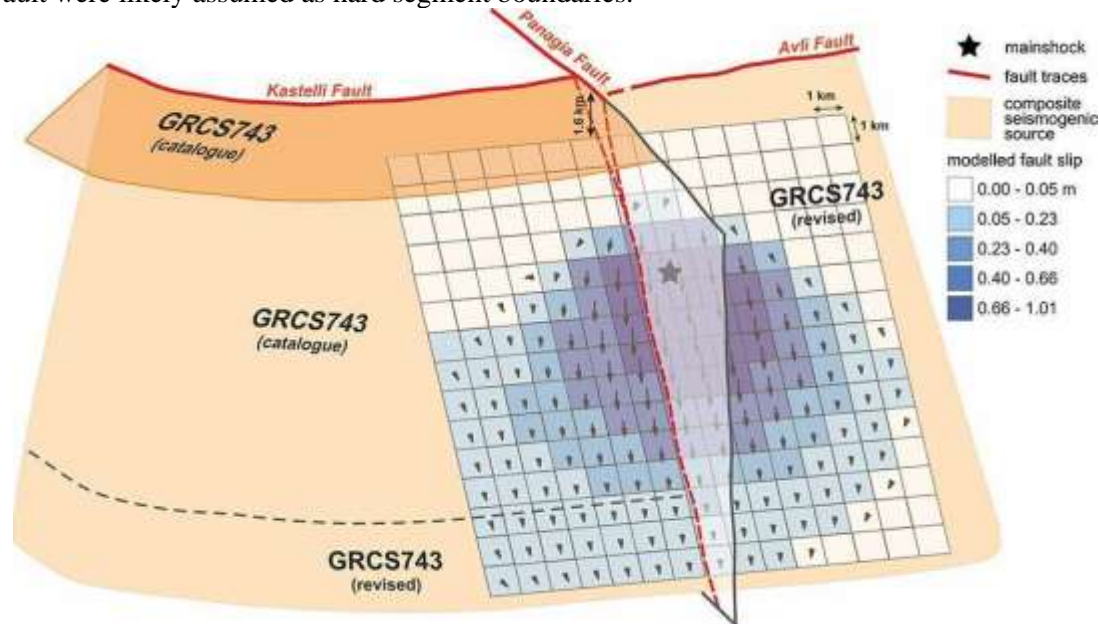


**Figure 11.** Perspective view of the modelled slip surface and its relations with the major faults affecting the investigated volume. The coseismic rupture reactivated the southern sector of the Kastelli seismogenic source, GRCS743 in GreDaSS (Caputo and Pavlidis, 2013), and propagated southwards into the Avli Fault and slightly downwards relative to what predicted in the database. The figure also shows the important, though indirect, role of the Panagia Fault during the 2021 seismic sequence. See text discussion.

From a seismotectonic point of view, the results and interpretations presented and discussed in this paper provide some major lessons.

Firstly, it is the important role that inherited faults (like the Panagia Fault) could possibly play in seismogenesis by altering the stress field close to active faults (like the Kastelli and Avli faults). Secondly, an overstep of a couple of km observed at the surface between fault traces, does not necessarily imply two distinct seismogenic sources as far as fault segments could merge at a few km depth thus forming a continuous surface. Finally, the seismic hazard prediction implicitly provided in GreDaSS specifically for Crete Island (Caputo and Pavlidis, 2013) was partially successful in predicting the reactivation of the Kastelli composite seismogenic source (GRCS743) and partially wrong by omitting the Avli segment and missing its contribution.

Altogether, the above learned lessons will also contribute to improve the database in Crete, but also in other similar geological and tectonic settings within the Aegean Region.

## References

1. Alac, R., Trinder, J., Rizos, C., 2016. Analysing post-seismic deformation of Izmit earthquake with InSAR, GNSS and Coulomb stress modelling. ISPRS - International Archives of the Photogrammetry, Remote Sensing and Spatial Information Sciences. XLI-B1. 417-421. 10.5194/isprs-archives-XLI-B1-417-2016.
2. Angelier, J., 1979. Néotectonique de l'Arc Égéen. Soc. Géol. Nord, Spéc. Publ., 3, 418 pp.
3. Atzori, S., Manunta, M., Fornaro, G., Ganas, A., Salvi, S., 2008. Postseismic displacement of the 1999 Athens earthquake retrieved by the Differential Interferometry by Synthetic Aperture Radar time series. J. Geophys. Res. 113. 10.1029/2007JB005504.

4. Atzori, S., Hunstad, I., Chini, M., Salvi, S., Tolomei, C., Bignami, C., & Stramondo, S., Trasatti, E., Antonioli, A., Boschi, E., 2009. Finite fault inversion of DInSAR coseismic displacement of the 2009 L'Aquila earthquake (central Italy). *Geophysical Research Letters*. 36. L15305. 10.1029/2009GL039293.
5. Atzori, S., Antonioli, A., Tolomei, C., De Novellis, V., De Luca, C., Monterroso, C., 2019. InSAR full-resolution analysis of the 2017–2018 M>6 earthquakes in Mexico. *Remote Sensing of Environment*. Volume 234. 111461. ISSN 0034-4257. <https://doi.org/10.1016/j.rse.2019.111461>.
6. Beutler, G., Rothacher, M., & Schaer, S., Springer, T., Kouba, J., Neilan, R., 1999. The International GPS Service (IGS): An interdisciplinary service in support of earth sciences. *Advances in Space Research - ADV SPACE RES*. 23. 631-653. 10.1016/S0273-1177(99)00160-X.
7. Bocchini, G. M., Brüstle, A., Becker, D., Meier, T., Keken, P.E., Ruscic, M., Papadopoulos, G., Rische, M., Friederich, W., 2018. Tearing, segmentation, and backstepping of subduction in the Aegean: New insights from seismicity. *Tectonophysics*. 734. 10.1016/j.tecto.2018.04.002.
8. Caputo, M., Panza, G., Postpischl, D., 1970. Deep Structure of the Mediterranean Basin. *Journal of Geophysical Research*. 75. 4919-4923. 10.1029/JB075i026p04919.
9. Caputo, R., 2005. Ground effects of large morphogenic earthquakes. *Journal of Geodynamics*. 40. 113-118. 10.1016/j.jog.2005.07.001.
10. Caputo, R., Monaco, C., Tortorici, L., 2006. Multiseismic cycle deformation rates from Holocene normal fault scarps on Crete (Greece). *Terra Nova*. 18. 181 - 190. 10.1111/j.1365-3121.2006.00678.x.
11. Caputo, R., Catalano, S., Monaco, C., Romagnoli, G., Tortorici, G., Tortorici, L., 2010a. Active faulting on the island of Crete (Greece). *Geophysical Journal International*. 183. 111-126. 10.1111/j.1365-246X.2010.04749.x.
12. Caputo, R., Catalano, S., Monaco, C., Romagnoli, G., Tortorici, G., Tortorici, L., 2010b. Middle-Late Quaternary geodynamics of Crete, Southern Aegean, and seismotectonic implications. *Bulletin of the Geological Society of Greece*. 43. 379-. 10.12681/bgsg.11191.
13. Caputo, R., Pavlides, S., 2013. The Greek Database of Seismogenic Sources (GreDaSS), version 2.0.0: A compilation of potential seismogenic sources (Mw>5.5) in the Aegean Region. <http://gredass.unife.it>, doi: 10.15160/unife/gredass/0200.
14. Cheloni, D., De Novellis, V., Albano, M., Antonioli, A., Anzidei, M., Atzori, S., Avallone, A., Bignami, C., Bonano, M., Calcaterra, S., Castaldo, R., Casu, F., Cecere, G., & Luca, C., Devoti, R., Bucci, D., Esposito, A., Galvani, A., Gambino, P., Doglioni, C., 2017. Geodetic model of the 2016 Central Italy earthquake sequence inferred from InSAR and GPS data. *Geophysical Research Letters*. 10.1002/2017GL073580.
15. Costantini, M., 1998. A novel phase unwrapping method based on network programming. *Geoscience and Remote Sensing, IEEE Transactions on*. 36. 813 - 821. 10.1109/36.673674.
16. Dai, K., Liu, G., Li, Z., Li, T., Yu, B., Wang, X., Singleton, A., 2015. Extracting vertical displacement rates in Shanghai (China) with multi-platform SAR images. *Remote Sensing*. 7. 9542-9562. 10.3390/rs70809542.
17. Delibasis, N., Ziazia, M., Voulgaris, N., Papadopoulos, T., Stavrakakis, G., Papanastassiou, D., Drakatos, G., 1999. Microseismic activity and seismotectonics of Heraklion area (central Crete Island, Greece). *Tectonophysics*. 308, 237–248.
18. Erol, S., Alkan, R., Ozulu, I. M., İlçi, V., 2020. Performance analysis of real-time and post-mission kinematic precise point positioning in marine environments. *Geodesy and Geodynamics*. 11. 401-410. 10.1016/j.geog.2020.09.002.
19. Fasoulas, Ch., 2001. The tectonic development of a Neogene basin at the leading edge of the active European margin: the Heraklion basin, Crete, Greece. *Journal of Geodynamics*. 31, 42-70.
20. Finetti I., 1976. Mediterranean Ridge: a young submerged chain associated with the Hellenic Arc, *Boll. Geofis. Teor. Appl.*, XIX (69), 31-65.
21. Floyd, M., Funning, G., Fialko, Y., Terry, R., Herring, T., 2020. Survey and continuous GNSS in the vicinity of the July 2019 Ridgecrest earthquakes. *Seismological Research Letters*. 91. 10.1785/0220190324.
22. Funning, G., Parsons, B., Wright, T., Jackson, J., Fielding, E., 2005. Surface displacements and source parameters of the 2003 Bam (Iran) earthquake from Envisat advanced synthetic aperture radar imagery. *Journal of Geophysical Research*. 110. B09406. 10.1029/2004JB003338.
23. Ganas, A., Oikonomou, A., Tsimi, C., 2013. NOAFAULTS: A digital database for active faults in Greece, *Bulletin of the Geological Society of Greece*. 47 (Proceedings of the 13Th International Congress). 47. 518-530.
24. Ganas, A., Fassoulas, C., Moschou, A., Bozionelos, G., Papathanassiou, G., Tsimi., Ch.; Valkaniotis, S., 2017. Geological and seismological evidence for NW-SE crustal extension at the southern margin of Heraklion Basin, Crete. *Bulletin of the Geological Society of Greece*, 51, 52–75. 10.12681/bgsg.15004.
25. Ganas, A., Hamiel, Y., Serpetsidaki, A., Briole, P., Valkaniotis, S. Fassoulas, C., Piatibratova, O., Kranis, H., Tsironi, V., Karamitros, I., Elias, P., Vassilakis, E., 2022. The Arkalochori Mw = 5.9 earthquake of 27 September 2021 inside the Heraklion Basin: A Shallow, blind rupture event highlighting the orthogonal extension of Central Crete. *Geosciences*, 12, 220, 10.3390/geosciences12060220.
26. Golshadi, Z., Famiglietti, N.A., Atzori, S., Vicari, A., 2022. Surface Displacement and Source Parameters of the 2021 Bandar-e Ge-naveh, Iran, Earthquake Determined from InSAR Observations. *Appl. Sci*. 12. 4223. 10.3390/app12094223.
27. Goldstein, R., Werner, C., 1998. Radar interferogram filtering for geophysical applications. *Geophysical Research Letters*, 25, 4035-4038. *Geophysical Research Letters*. 25. 10.1029/1998GL900033.
28. Halpaap, F., Rondenay, S., Perrin, A., Goes, S., Ottemoller, L., Austrheim, H., Shaw, R., Eeken, T., 2019. Earthquakes track subduction fluids from slab source to mantle wedge sink. *Science Advances*. 5. eaav7369. 10.1126/sciadv.aav7369.
29. Hanssen, R., 2001. Radar interferometry data interpretation and error Analysis. 10.1007/0-306-47633-9.
30. Huguen, C., Chamot-Rooke, N., Loubrieu, B., Mascle, J., 2006. Morphology of a pre-collisional, salt-bearing, accretionary complex: The Mediterranean Ridge (Eastern Mediterranean). *Marine Geophysical Researches*. 27. 61-75. 10.1007/s11001-005-5026-5.
31. IGME - Institute of Geology and Mineral Exploration, 1989. Geological map of Greece—Mochos sheet (scale 1:50.000). IGME, 1989, Athens.

32. Jadaszliwer, B., Camparo, J., 2021. Past, present and future of atomic clocks for GNSS. *GPS Solutions*. 25. 10.1007/s10291-020-01059-x.
33. Kokkalas, S., Doutsos, T., 2001. Strain-dependent stress field and plate motions in the South-East Aegean region. *Journal of Geodynamics*. 32. 311-332. 10.1016/S0264-3707(01)00035-7.
34. Kuzin, S., 2021. The key role of GNSS for monitoring geodetic parameters of the Earth, *INASAN Science Reports*. 10-15. 10.51194/INASAN.2021.6.1.003.
35. Le Pichon, X., Angelier, J., 1979. The Hellenic Arc and Trench System: a key to the neotectonic evolution of the Eastern Mediterranean Area. *Tectonophysics*. 60. 1-42. 10.1016/0040-1951(79)90131-8.
36. Marquardt, D.W., 1963. An algorithm for least-squares estimation of nonlinear parameter. *Journal of the Society for Industrial and Applied Mathematics*. 11. 431-441.
37. Massonnet, D., Feigl, K., 1998. Radar interferometry and its application to changes in the Earth's surface. *Rev. Geophys.* 36, 441-500. *Reviews of Geophysics*. 36. 10.1029/97RG03139.
38. McKenzie, D., 1972. Active Tectonics of the Mediterranean Region. *The Geophysical Journal of the Royal Astronomical Society*. 30.109-185. DOI: 10.1111/j.1365-246X.1972.tb02351.x.
39. Menke, W., 1989. *Geophysical Data Analysis: Discrete Inverse Theory*. 1st Edition, Academic Press, San Diego, 289.
40. Okada Y., 1985. Surface deformation due to shear and tensile faults in a half-space. *Bull. Seismol. Soc. Am.*, vol. 75, no. 4, pp. 1135-1154, Aug.
41. Oktar, O., Erdoğan, H., Poyraz, F., Tiryakioglu, I., 2021. Investigation of deformations with the GNSS and PSInSAR methods. *Arabian Journal of Geosciences*. 14. 10.1007/s12517-021-08765-x.
42. Pavlides, S., Caputo, R., 2004. Magnitude versus faults' surface parameters: Quantitative relationships from the Aegean Region. *Tectonophysics*. 380. 159-188. 10.1016/j.tecto.2003.09.019.
43. Pepe, A., Calò, F., 2017. A review of Interferometric Synthetic Aperture RADAR (InSAR) Multi-Track approaches for the retrieval of Earth's surface displacements. *Applied Sciences*. 7. 1264. 10.3390/app7121264.
44. Redhwan, A., Erdoğan, H., Gezgin, C., Oktar, O., 2021. Monitoring of continuous GNSS stations at Central Anatolia Region. *Turkish Journal of Geosciences*. 10.48053/turkgeo.996719.
45. Reilinger, R., McClusky, S., Paradisis, D., Ergintav, S., Vernant, P., 2010. Geodetic constraints on the tectonic evolution of the Aegean region and strain accumulation along the Hellenic subduction zone. *Tectonophysics*. 488. 22-30. 10.1016/j.tecto.2009.05.027.
46. Rizos, C., 1997. Principles and practice of GPS surveying. Edition 17 of Monograph (University of New South Wales. School of Geomatic Engineering).
47. Robertson, J., Meschis, M., Roberts, G., Ganas, A., Gheorghiu, D., 2019. Temporally constant Quaternary uplift rates and their relationship with extensional upper-plate faults in south Crete (Greece), constrained with <sup>36</sup>Cl exposure dating. 10.31223/osf.io/sgmf6.
48. Sakkas, V., 2021. Ground deformation modelling of the 2020 Mw6.9 Samos earthquake (Greece) based on InSAR and GNSS data. *Remote Sensing*. 13. 10.3390/rs13091665.
49. Sugar, D., Bacic, Z., 2021. Kinematic effects of M5.5 Zagreb earthquake assessed by GNSS method supported by Galileo satellite system. 385-396. 10.5592/CO/ICroCEE.2021.74.
50. Takasu, T., Yasuda, A., 2009. Development of the low-cost RTK-GPS receiver with an open source program package RTKLIB. *International Symposium on GPS/GNSS*.
51. Tiryakioglu, I., Aktug, B., Yigit, C., Yavaşoğlu, H., Sozibilir, H., Özkaymak, C., Poyraz, F., Taneli, E., Bulut, F., Dogru, A., Ozener, H., 2017. Slip distribution and source parameters of the 20 July 2017 Bodrum-Kos earthquake (Mw6.6) from GPS observations. *Geodynamica Acta*. 30. 1-14. 10.1080/09853111.2017.1408264.
52. Tiryakioglu, I., Aktug, B., Yigit, C., Yavaşoğlu, H., Sozibilir, H., Özkaymak, C., Poyraz, F., Taneli, E., Bulut, F., Dogru, A., Ozener, H., 2017. Slip distribution and source parameters of the 20 July 2017 Bodrum-Kos earthquake (Mw6.6) from GPS observations. *Geodynamica Acta*. 30. 1-14. 10.1080/09853111.2017.1408264.
53. Tolomei, C., Caputo, R., Polcari, M., Famiglietti, N. A., Maggini, M., Stramondo, S., 2021. The use of Interferometric Synthetic Aperture Radar for isolating the contribution of major shocks: the case of the March 2021 Thessaly, Greece, seismic sequence. *Geosciences*. 11. 10.3390/geosciences11050191.
54. Triantafyllou, I., Karavias, A., Koukouvelas, I., Papadopoulos, G.A., Parcharidis, I. The Crete Isl. (Greece) Mw6.0 Earthquake of 27 September 2021: expecting the unexpected. *GeoHazards* 2022. 3. 106-124. <https://doi.org/10.3390/geohazards3010006>.
55. Vallianatos, F., Michas, G., Hloupis, G., Chatzopoulos, G., 2022a. The evolution of preseismic patterns related to the Central Crete (Mw6.0) strong earthquake on 27 September 2021 revealed by Multiresolution Wavelets and Natural Time Analysis. *Geosciences*. 12. 33. 10.3390/geosciences12010033.
56. Vallianatos F, Karakostas A, Michas G, Pavlou K, Kouli M, Sakkas V. 2022b. On the patterns and scaling properties of the 2021-2022 Arkalochori earthquake sequence (Central Crete, Greece) Based on Seismological, Geophysical and Satellite Observations. *Applied Sciences*. 12(15).7716. <https://doi.org/10.3390/app12157716>.
57. Vassilakis, E., Kaviris, G., Kapetanidis, V., Papageorgiou, E., Foulmelis, M., Konsolaki, A., Petrakis, S., Evangelidis, C., Alexopoulos, J., Karastathis, V., Voulgaris, N., Tselentis, A., 2022 The 27 September 2021 Earthquake in Central Crete (Greece)—Detailed analysis of the earthquake sequence and indications for contemporary arc-parallel extension to the Hellenic Arc. *Applied Sciences*. 12. 2815. 10.3390/app12062815.
58. Vincenty, T., 1975. Direct and inverse solutions of geodesics on the ellipsoid with application of nested equations. *Survey Review*. 23. 88-93. 10.1179/sre.1975.23.176.88.
59. Vincenty, T., 2013. Formula for distance between two Latitude/Longitude points, Online: <http://www.movabletype.co.uk/scripts/lat-long-vincenty.html>.
60. Williams, C., Wadge, G., 1998. The effects of topography on magma chamber deformation models: Application to Mt. Etna and radar interferometry. *Geophysical Research Letters - GEOPHYS RES LETT*. 25. 1549-1552. 10.1029/98GL01136.

61. Wright, T., Lu, Z., Wicks, C., 2003. Source model for the Mw 6.7, 23 October 2002, Nenana Mountain earthquake (Alaska) from InSAR. *Geophysical Research Letters*. 30. 10.1029/2003GL018014.
62. Zebker, H., Pepin, K., 2021. Maximum temporal baseline for InSAR time series. 2652-2654. 10.1109/IGARSS47720.2021.9554071.



Ινστιτούτο Φυσικής Εσωτερικού της Γης  
& Γεωκαταστροφών

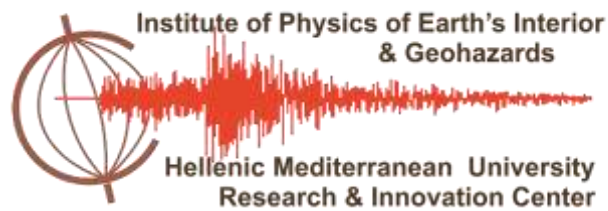
Ελληνικό Μεσογειακό Πανεπιστήμιο  
Πανεπιστημιακό Κέντρο Έρευνας & Καινοτομίας



United Nations  
Educational, Scientific and  
Cultural Organization

uniTwin

- UNESCO Chair on
- "Solid Earth Physics and
- Geohazards Risk Reduction"



Institute of Physics of Earth's Interior  
& Geohazards

Hellenic Mediterranean University  
Research & Innovation Center

**Chania, September 2022**